III-NITRIDE SELF-ASSEMBLED QUANTUM DOT LIGHT EMITTING DIODES AND LASERS

by

Animesh Banerjee

A dissertation submitted in partial fulfillment
of the requirements for the degree of
Doctor of Philosophy
(Electrical Engineering)
in The University of Michigan
2014

Doctoral Committee:

Professor Pallab K. Bhattacharya, Chair
Associate Professor Pei-Cheng Ku
Professor Joanna Mirecki-Millunchick
Professor Jamie D. Phillips

© Animesh Banerjee 2014
All Rights Reserved

To my parents who have always stood by me, and have showered their blessings, unconditional love and unwavering support

ACKNOWLEDGMENT

I would like to express my sincere gratitude to my advisor Prof. Pallab Bhattacharya for his continuous support and motivation, his immense knowledge, enthusiasm and patience powering me along the way during my PhD years. He is a great motivator and educator. He was always available to discuss my research and any technical problem that I encountered. His sheer persistence and determination in solving any problem is something I really admire and aspire to pursue for the rest of my life. It has been truly an honor to work with Prof. Bhattacharya. I am also grateful to my committee memebers, Prof. Pei-Cheng Ku, Prof. Jamie Phillips, and Prof. Joanna Mirecki-Millunchick, for their time, insightful comments, and valuable suggestions. I would like to specially thank Prof. Millunchick for her valuable discussions and inputs during our collaborative endeavor.

I am thankful to Dr. Meng Zhang and Dr. Wei Guo, my mentors in this group for getting me aquainted with epitaxial growth, fabrication and characterization. I would like to thank Dr. Junseok Heo for guiding me in my first research project here. I thank Dr. Ayan Das for being my roommate and a dear friend who I could always rely upon. I am thankful to Dr. Sishir Bhowmick, Thomas Frost, Shafat Jahangir, Jimmy Chen, Saniya Deshpande, and Bo Xiao for the countless hours of technical discussion, their advice and cooperation. Special thanks to my mentee Thomas Frost who made the last two years of my research thoroughly enjoyable through his technical inputs, constant support and cheerful demeanor. He is a dear friend of mine and I wish him all the success in the years to follow. I would also like to thank my past group members, Dr. Debashish Basu, Dr.

Guan Huang, Dr. Chi-Sen Lee, and Dr. Hyun Kum from whom I have learned much. I would also like to thank my newer group members and colleagues Md Zunaid Baten, Ethank Stark, Alan Teran, and Arnab Shashi Hazari - they are extremely talented, yet friendly and supportive. I wish them good luck on their future work.

Life in Ann Arbor was one of the busiest periods of my life, yet the moments of candor, camaraderie and the everlasting friendships I built during this course have helped me always stay fresh and has spurred me on. I thank Anchal Agarwal, Daya S. Khudia, Ankit Sethia, Abhayendra Singh, Ritesh Parikh, Gaurav Chadha and Dr. Soumya Kundu. Special thanks to Anchal Agarwal for her love and support during the best and worst years of my PhD life.

The excellent support of the Lurie nanofabrication facility staff is greatly appreciated. In particular, I give my special thanks to Dennis Schweiger and Dennis Grimard whose expertise and generous help have ensured that I have learned much more about my experimental tools and have allowed me to continue my work unimpeded. I would also like to thank Greg Allion, David Sebastian, Antony Sebastian, Russ Clifford, Matthew Oonk, Sandrine Martin and Pilar Herrera-Fierro for their mentorship and help in device fabrication.

I would like to extend my gratitude to Lisa Vogel, Melanie Caughey, Laura Jarels, Deb Swartz, and Beth Stalnaker for administrative support throughout my graduate career. I wish to acknowledge the National Science Foundation (NSF) and KAUST for funding my research. Last but not the least, I thank my parents, D. K. Bandyopadhyay and Rita Banerjee whose unconditional love and support was instrumental in overcoming some of the toughest challenges I have faced during this course.

TABLE OF CONTENTS

DEDICATION ii

ACKNOWLEDGMENT iii

LIST OF FIGURES viii

LIST OF TABLES xv

LIST OF APPENDICES xvi

ABSTRACT xvii

CHAPTER

I. INTODUCTION 1

1.1 Solid State Lighting: Background and Motivation 1
1.2 History of III-Nitride Research and DOE Roadmap 6
1.3 Challenges Facing III-Nitride Research 9
1.3.1 Availability of substrate for gallium nitride growth 9
1.3.2 Efficiency droop in blue and green emitting diodes 10
1.3.3 Large lasing threshold and longer wavelength lasing in (In)GaN lasers 11
1.3.4 Issues with p-doping 13
1.3.5 Large polarization field and associated problems 14
1.4 Our Approach: Use of Quantum Dots 17
1.5 Dissertation Overview 18

II. GROWTH AND CHARACTERIZATION OF SELF-ASSEMBLED INGAN/GAN QUANTUM DOTS BY PLASMA-ASSISTED MOLECULAR BEAM EPITAXY 21

2.1 Introduction 21
2.2 Growth and Characterization of n-doped GaN Buffer 24
2.3 Growth Optimization of Self-Assembled InGaN/GaN Quantum Dots 29
2.3.1 Optimization of number of InGaN monolayers (MLs) 30
2.3.2 Optimization of N_2 growth interruption time for each dot layer 31
2.3.3 Optimization of GaN barrier layer thickness 33
2.4 Optical Characterization of Optimized Blue and Green InGaN/GaN Quantum Dots 34
2.4.1 Temperature dependent and time resolved photoluminescence measurements 35
2.4.2 Thermal activation energy for InGaN/GaN radiative recombination 39

2.4.3 Temperature dependent photoluminescence shift: absence of S-shaped behavior 41
2.5 Structural Characterization of InGaN/GaN Quantum Dots 42
2.5.1 Atomic force microscopy (AFM) and scaling theory 42
2.5.2 Transmission electron microscopy of InGaN/GaN quantum dots 44
2.6 Summary 46

III. INGAN/GAN QUANTUM DOT LIGHT EMITTING DIODES 47

3.1 Introduction 47
3.2 Growth of InGaN/GaN Quantum Dot Light Emitting Diode Heterostructure 48
3.3 Fabrication and Characterization of Quantum Dot LEDs 52
3.3.1 Fabrication of a typical LED 52
3.3.2 Fabrication of High Speed LEDs 54
3.4 Output Characteristics of Quantum Dot LEDs 55
3.4.1 Current-voltage characteristics 55
3.3.2 Electroluminescence of quantum dot LED 56
3.4.3 Efficiency characteristics of quantum dot LEDs 59
3.5 Differential Carrier Lifetime Measurements of Quantum Dot and Quantum Well LEDs 61
3.5.1 Introduction 61
3.5.2 Heterostructure design and measurement 62
3.5.3 Results and discussion 64
3.6 Summary 69

IV. SELF-ASSEMBLED INGAN/GAN QUANTUM DOTS AS DISLOCATION FILTERS 70

4.1 Introduction 70
4.2 Design, Growth and Characterization of InGaN/GaN Quantum Dot Dislocation Filter 71
4.2.1 Growth of InGaN/GaN quantum dot dislocation filter 72
4.2.2 Etch pit dislocation measurement 73
4.2.3 Theoretical calculation 75
4.2.4 Deep level traps in n^+-p GaN junctions on quantum dot dislocation filter 79
4.3 Optical Properties of Green-Emitting Quantum Dot active Region on Dislocation Filter 80
4.4 Output Characteristics of Green-emitting QD LEDs on QD Dislocation Filter 83
4.5 Summary 86

V. INGAN/GAN QUANTUM DOT LASERS 88

5.1 Introduction 88
5.2 Design and Growth of InGaN/GaN Quantum Dot Laser Heterostructures 90

5.2.1 Growth of AlGaN cladding layer..92
5.2.2 Growth of InGaN waveguide layer on top of AlGaN cladding layer..95
5.2.3 The laser heterostructure..96
5.3 Fabrication of Ridge Waveguide Quantum Dot Lasers..............................99
5.3.1 Processing of Ridge Geometry Waveguide Heterostructure 99
5.3.2 Cleaved facet mirrors for longitudinal confinement..........................101
5.4 Characteristics of Blue-Emitting InGaN/GaN Quantum Dot Lasers.......102
5.4.1 Output-current and spectral characteristics.......................................102
5.4.2 Measurement of differential gain..106
5.4.3 Polarization output and near field characteristics..............................107
5.5 Characteristics of Red-Emitting (λ=630 nm) InGaN/GaN Quantum Dot Lasers...109
5.6 Summary 111

VI. OPTICAL AND SPIN PROPERTIES OF CARRIERS IN INGAN DOTS IN GAN NANOWIRES GROWN ON SILICON..113

6.1 Introduction..113
6.2 Growth and Characterization of InGaN Dots in GaN Nanowires 114
6.2.1 Growth of InGaN/GaN dot-in-nanowire heterostructure...................114
6.2.2 Photoluminescence of GaN nanowires 116
6.2.3 Time-resolved photoluminescence of GaN nanowires and InGaN dots in GaN nanowires..117
6.3 Properties of Spin Polarized Carriers in InGaN Dots in GaN Nanowires...120
6.3.1 Introduction...120
6.3.2 Optical injection and detection of spin polarized carriers 122
6.3.3 Spin polarization lifetimes of electrons in InGaN dots in GaN nanowires 125
6.3.4 Discussion and theoretical analysis 129
6.4 Summary 133

VII. CONCLUSION AND SUGGESTIONS FOR FUTURE WORK 134

7.1 Summary of the Present Work...134
7.2 Suggestions for the Future Work 137
7.2.1 Red-emitting quantum dot LEDs with dislocation filter 137
7.2.2 Red-green-blue (RGB) white light sources.......................................139
7.2.3 High power quantum dot lasers 141

APPENDICES 143

BIBLIOGRAPHY 153

LIST OF FIGURES

Figure

1.1: Measured external quantum efficiencies for state-of-the-art LEDs emitting in the visible spectrum [1] 2

1.2: Energy efficiency of a solid state nitride LED compared to incandescent and compact fluorescent lamps [2] 3

1.3: Applications of nitride-based visible LEDs. 4

1.4: Applications of nitride-based visible lasers 5

1.5: Packaged nitride LED revenue 6

1.6: DOE goal for solid state LEDs as compared to high intensity discharge (HID) and linear fluorescent lamps (LFL). 8

1.7: Efficiency droop observed in state-of-the-art c-plane quantum well LEDs 10

1.8: Threshold current density for CW lasing at longer wavelengths by several groups [Modified from 27]. 12

1.9: Polar wurtzite crystal structure of GaN. 12

1.10: (a) Simulated band diagram of a typical InGaN/GaN multi quantum well (QW) LED with (solid line) and without (dashed line) polarization field; (b) Electron hole wavefunction separation in c-plane InGaN/GaN QW due to polarization field [33] 15

2.1: Schematics of three different growth modes: (a) Frank-van der Merwe (FM), (b) Volmer Weber (VM) and (c) Stranski-Krastonow growth modes.. 23

2.2: Veeco Gen 930 Plasma-assisted molecular beam epitaxy (MBE) system in our lab. 25

2.3: Schematics of typical heterostructures for optimizing (a) underlying GaN buffer layer and (b) InGaN/GaN QD growth conditions for optical and structural characterization.. 26

2.4: Atomic force microscopy (AFM) images of 300 nm of n-doped GaN layer grown on GaN/sapphire template with different Ga fluxes (a), (b) and (c)... 26

2.5: Photoluminescence spectra of n-GaN band edge emission corresponding to Ga fluxes for which the AFMs are shown in Figs. 2.4 (a), (b) and (c).. 27

2.6: A 10 μm x 10 μm micrograph of a GaN layer growth with metal droplet formation at Φ_{Ga} = 5 nm/min...28

2.7: In-situ RHEED characterization during QD formation showing the RHEED pattern changing from streaky (layer-by-layer growth) to spotty (QD or island formation) pattern at (a) t = 0s, (b) t = 15s and (c) t = 20s.. 29

2.8: Influence of the number of monolayers (MLs) of InGaN deposited to form QDs on its (a) PL intensity and peak energy, and (b) lifetimes.. 31

2.9: Influence of N2 interruption times after each layer of InGaN QD formation on its (a) PL intensity and peak energy, and (b) lifetimes..................................32

2.10: Influence of GaN barrier layer thickness after each layer of InGaN QD formation on its (a) PL intensity and peak energy, and (b) lifetimes..................34

2.11: Photoluminescence spectra of (a) blue-emitting and (b) green-emitting eight layers of InGaN/GaN QDs grown on free-standing GaN bulk substrates under different temperatures..36

2.12: Room temperature carrier decay times obtained from time-resolved PL measurements and fit with stretched exponential model for blue emitting InGaN/GaN QDs...38

2.13: Total, radiative and non-radiative carrier lifetimes obtained from TRPL and time dependent PL measurements for (a) blue and (b) green emitting InGaN/GaN quantum dots...38

2.14: Thermal activation of blue emitting QD photoluminescence grown on GaN/sapphire templates. Sample A: radiative efficiency 44%; Sample B: Radiative efficiency 18%. 40

2.15: PL peak energy shift with temperature for (a) blue and (b) green emitting InGaN/GaN QDs fit with Varshni equation...41

2.16: Atomic force microscopy (AFM) measurements of a (a) blue and (b) green emitting InGaN/GaN QDs...43

2.17: QD height distribution of (a) blue and (b) green emitting InGaN/GaN QDs obtained from AFM measurements and fit with scaling theory showing good epitaxial growth of dots. 44

2.18: (a) Transmission electron microscope (TEM) image of seven layers of red--emitting InGaN/GaN QDs, (b) bright field TEM indicating how dislocations can propagate through the dots, and (c) high resolution TEM of a single QD. 45

3.1: Schematic of InGaN/GaN quantum dot LED heterostructure grown on GaN-templated c-plane sapphire substrates.. 49

3.2: (a) X-ray diffraction (XRD) showing composition of AlGaN, (b) room temperature photoluminescence showing AlGaN and GaN band-edge emissions, and (c) a 5μm x 5μm atomic force microscopy (AFM) image of 150 nm $Al_{0.15}Ga_{0.85}N$ layer on GaN/sapphire template for electron blocking layer. 51

3.3: (a) Schematic of a fabricated QD LED heterostructure and (b) photo micrograph of fabricated LEDs from top. 53

3.4: (a) Schematic and (b) micrograph of a fabricated high-speed QD LED heterostructure for measurement using G-S-G probe. 54

3.5: (a) Current-voltage characteristics for different EBL layers in QD blue LEDs. Micrographs of (b) blue and (c) green QD LEDs under 100 A/cm2 injection. 57

3.6: Electroluminescence of (a) blue and (b) green QD LEDs. The injection dependent peak emission shift is shown in the inset for the respective LEDs. 58

3.7: Efficiency characteristics indicating low efficiency droop and peaking of efficiencies at low current densities for (a) blue- and (b) green-emitting QD LEDs. 59

3.8: (a) Measured current-voltage and light-current characteristics at T = 300K for quantum dot LED. Inset shows electroluminescence spectrum at 300 K, (b) measured internal quantum efficiency of quantum dot LED. The solid curve indicates a fit to the data using the A-B-C model.. 63

3.9: Measured differential lifetime τ and calculated radiative and non-radiative lifetimes, τr and τnr, respectively, as a function of injection current density in (a) quantum dot LED, and (b) quantum well LED. 65

3.10: Calculation flow for measuring differential carrier lifetime and analysis of radiative lifetimes, and A, B, C parameters.. 66

4.1: Heterostructure schematics for etch pit dislocation measurements with: (a) no QD dislocation filter, (b) InxGa1-xN/GaN QD dislocation filters having 3 and 5 QD layers, and (c) dislocation filter having 3 GaN/AlN QD layers grown on relaxed AlN.. 72

4.2: Atomic force microscopy (AFM) images of the GaN surfaces after etch pit dislocation (EPD) treatment on (a) control sample without dislocation filter, (b) sample with 3 layers of $In_{0.2}Ga_{0.8}N$/ GaN QD dislocation filter, and (c) sample with 3 layers of GaN/AlN QD dislocation filter.. 73

4.3: (a) Dark field transmission electron microscopy image showing annihilation and propagation of dislocation through QD dislocation filter and (b) calculated bending ratio of threading dislocation as a function of dot base width. 74

4.4: (a) Arrhenius plot of the emission time constant versus reciprocal temperature for (a) electron traps and (b) hole traps measured in n+-p GaN diodes grown without a dislocation filter.. 78

4.5: (a) Photoluminescence spectrum of the $In_{0.35}Ga_{0.65}N$/GaN QDs grown on QD dislocation filters and (b) temperature dependence of the peak emission energy showing a good fit with the Varshni equation. 80

4.6: (a) Excitation dependence of quantum efficiency in In0.35Ga0.65N/GaN QD samples grown without (sample A) and with (sample B) dislocation filter. The solid lines are joins of the data points and (b) luminescence decay transients measured for samples A and B. The solid lines are obtained from the rate equations... 82

4.7: A typical green-emitting InGaN/GaN QD LED heterostructure with QD dislocation filter and an AFM image of the green-emitting dots shown alongside. 83

4.8: A typical green-emitting InGaN/GaN QD LED heterostructure with QD dislocation filter and an AFM image of the green-emitting dots shown alongside. 84

4.9: Measured current-voltage characteristics(a), light-current characteristics(b), and external quantum efficiency as a function of injection current density(c) for green-emitting QD light emitting diodes with and without QD dislocation filters. 85

5.1: (a) Schematic of InGaN/GaN quantum dot laser heterostructure grown on a n-GaN bulk substrate with corresponding Mg flux used for each layer mentioned, (b) schematic of gain + feedback mechanism for laser operation, and (c) simulated transverse optical mode profiles for two different combinations of InGaN waveguide/AlGaN cladding layers. The dashed lines indicate the waveguide region. 90

5.2: (a) Schematic of heterostructure for AlGaN cladding layer calibration. A 5µm x 5µm AFM image showing the surface morphology of 700 nm $Al_{0.098}Ga_{0.902}N$ layer and (b) XRD data of $Al_{0.098}Ga_{0.902}N$ grown on GaN. 93

5.3: (a) A 5µm x 5µm AFM image showing the surface morphology of 700 nm $Al_{0.07}Ga_{0.93}N$ layer and (b) PL of $Al_{0.07}Ga_{0.93}N$ grown on GaN. 94

5.4: (a) Schematic of a typical heterostructure for InGaN waveguide layer calibration. A 5µm x 5µm AFM image showing the surface morphology of different In composition (b) $In_{0.05}Ga_{0.95}N$ and (c) $In_{0.02}Ga_{0.98}N$ waveguide layers. 95

5.5: (a) Schematic of a typical half laser heterostructure for calibration of the AlGaN cladding, InGaN waveguide and topmost QD layers. (b) A 1µm x 1µm AFM image of the blue $In_{0.22}Ga_{0.78}N$/GaN QDs, (c) room temperature PL of the blue $In_{0.22}Ga_{0.78}N$/GaN QDs, and (d) XRD of the half laser heterostructure showing very good fit with dynamical diffraction theory.. 96

5.6: (a) Schematic of a fabricated laser heterostructure showing all the layers and (b) an SEM image of the laser heterostructure showing the fabricated laser heterostructure along with the cleaved mirror facet.. 99

5.7: (a) Schematic of a fabricated laser heterostructure showing all the layers and (b) an SEM image of the laser heterostructure showing the fabricated laser heterostructure along with the cleaved mirror facet. 101

5.8: Light output versus current (L-I) characteristics of blue-emitting QD lasers under (a) 5% pulsed and (b) continuous wave (CW) mode operation.. 103

5.9: (a) Electroluminescence spectra of the laser with the spontaneous recombination from PL shown alongside and (b) peak emission wavelength shift with increasing injection for the laser.. 103

5.10: (a) Schematic of the laser heterostructure using GaN cladding and a higher In composition InGaN waveguide, (b) light output versus current (L-I) characteristics for a conventional laser heterostructure (Fig. 5.1(a)) and a GaN-clad laser heterostructure (Fig. 5.10(a)), and (c) lasing peak emission for the GaN-clad laser heterostructure.. 104

5.11: (a) Cavity length dependence of inverse differential quantum efficiency and (b) variation of threshold current density with inverse cavity length..........107

5.12: Laser output polarization as a function of injection current density... 108

5.13: (a) Contour plot of the near field image of the laser mode. Laser mode profile in the transverse (b) and longitudinal (c) directions, as compared with the mode profiles simulated by transfer matrix method............................109

5.14: (a) Schematic of red $In_{0.4}Ga_{0.6}N$/GaN QD laser, (b) spectral output from a single facet of the laser under continuous wave bias below and above threshold, and (c) light-current characteristics of the laser from a single facet. 110

6.1: (a) High density GaN nanowires grown on (001) Si and (b) HR-TEM image showing a GaN nanowire with multiple InGaN/GaN dot-in-nanowire heterostructures. The high resolution cross-TEM image shown in the inset depicts a single dot-in-nanowire [135]..115

6.2: (a) Room temperature PL of GaN nanowire ensemble showing absence of yellow band and (b) PL spectra of a GaN nanowire sample measured at 25K showing three sharp bulk related excitons and a broad surface-related defect bound exciton. 117

6.3: PL decay transients obtained from TRPL on as-grown and passivated GaN nanowires for (a) bulk excitons which remain unchanged and (b) surface excitons which change with passivation. 118

6.4: (a) Carrier decay time for InGaN dot in GaN nanowire measured at λ=420 nm and at different temperatures and (b) value of τ_1 and τ_2 obtained from rate equation analysis of measured data from (a)..120

6.5: (a) Schematic of InGaN dots in GaN nanowire heterostructure used for spin measurements and (b) anisotropic band diagram of GaN showing very low separaction of HH and LH bands [147]..123

6.6: Schematics of the measurement set-up for optical injection and detection of spin properties.. 124

6.7: (a) Polarization dependent photoluminescence spectra of sample 1 at T = 300 K under resonant excitation (λ = 395 nm) and (b) spin polarized transient photoluminescence at T=240 K for sample 2 measured at λ=420 nm. Inset shows the temporal variation of the degree of polarization. 127

6.8: Spin lifetimes as a function of temperature (a) in sample 3 at λ=420, 450 and 480 nm, (b) in samples 1, 2 and 4 measured at their peak wavelength

(λ=407, 420 and 453 nm, respectively). The dashed lines are the theoretical spin lifetimes calculated as described in subsequent section. 128

6.9: Calculated spin lifetimes limited by Elliot-Yafet scattering in InxGa1-xN quantum dots as a function of In composition at 100 and 300 K. 130

7.1: (a) Schematic of a proposed heterostructure for growing red QD LED on dislocation filter and (b) PL spectrum of the red-emitting QD grown on dislocation filter with InGaN barrier. 138

7.2: Schematic of a proposed heterostructure for growing white QD LED on GaN/sapphire template. 139

7.3: (a) Schematic of the heterostructure for white dots-in-nanowire LED on silicon, (b) electroluminescence spectra and (c) micrograph of an active white nanowire LED [127]. 140

7.4: A major application of high power laser is in heads-up display used in automobiles. 141

7.5: Proposed overhead schematic of a flared broad area laser for high output power. 142

LIST OF TABLES

Table

1.1: Different substrates used for nitride LED and laser epitaxy. 9

3.1: Description of the samples used to optimize the EBL layer for lowest turn-on voltage and series resistance.. 56

4.1: Description of the samples used for etch pit dislocation density measurements...75

4.2: Characteristics of deep levels in GaN obtained from transient capacitance measurements...81

6.1: Description of the samples used for measurement of spin lifetimes... 126

6.2: Fitting parameter for sample 3 at different wavelengths... 132

6.3: Fitting parameters for sample 1, 2 and 4..132

LIST OF APPENDICES

APPENDIX

A: Substrate Preparation Prior to MBE Growth. 144

B: Quantum Dot Ridge Waveguide Laser Processing...145

ABSTRACT

Nitride-based light emitting diodes (LEDs) and lasers are in high demand due to their numerous applications in solid state lighting, optical data storage, full color mobile projectors, heads-up displays, and other medical and military applications. Current state-of-the-art quantum well (QW) based devices suffer from large polarization field, In clustering effects, and large threading dislocation density resulting in strong band bending and associated carrier leakage, large efficiency droop at high injections in LEDs and large threshold current densities in lasers. The objective of this doctoral research was to develop the optimum growth conditions of self-assembled InGaN/GaN quantum dots (QDs) through optical and structural characterization, and to utilize them in the demonstration and characterization of high performance visible InGaN/GaN LEDs and lasers.

Self-assembled InGaN/GaN QDs were grown in a plasma-assisted molecular beam epitaxy (MBE) system via strain relaxation and therefore have reduced density of dislocations, smaller polarization field, and large electron-hole wavefunction overlap, resulting in higher radiative efficiencies and shorter radiative lifetimes. The growth conditions for the QDs were optimized through extensive structural and optical characterization to achieve high dot density (~3-8 x 10^{10} cm^{-2}), reduced radiative lifetimes (~0.6 ns and ~1.5 ns for blue and green QDs), high radiative efficiencies (~60% and ~40% for blue and green QDs, respectively), and no S-shaped peak emission shift with temperature typically associated with In clustering effects. The QD LED

heterostructure design, growth and processing were optimized to demonstrate devices with low leakage current, low turn-on voltage (3.5 V), low series resistance (< 10 Ω) and low efficiency droop (< 20%). Small signal modulation measurements were carried out in QW and QD based high speed LEDs to derive differential carrier lifetimes at various injection levels, which helps in the understanding of the recombination dynamics of carriers in the active region. A study of the use of InGaN/GaN QDs as dislocation filters was also investigated with the objective of growing active regions with lower defect densities.

Growth conditions for the laser cladding (AlGaN) and waveguide (InGaN) layers grown by PA-MBE were optimized to obtain epitaxial layers of high crystalline quality which were used to demonstrate some of the first nitride QD lasers. Ridge waveguide blue-emitting (λ=418 nm) QD lasers demonstrated significantly lower threshold current densities ~930 A/cm^2 and a small peak emission shift of 4.8 nm with injection. From cavity length dependent light-current measurements a high differential gain of 2x10^{-16} cm^2 was derived. Longer wavelength (λ=478 nm) QD lasers were also characterized. The first nitride-based red lasers were demonstrated incorporating $In_{0.4}Ga_{0.6}N$/GaN QDs as the active region and InAlN layers as cladding layers. The red lasers were characterized by a threshold current density of ~2.5 kA/cm^2 and a peak emission shift of only 11.6 nm.

Additionally, InGaN-dot-in-GaN nanowire heterostructures were grown by MBE on silicon substrates and optically characterized. The nanowires have a high aspect ratio and filter the dislocations through their sidewalls, resulting in high radiative efficiencies. The dynamics of spin polarized carriers in this relatively defect free nitride environment was studied for the first time by optical injection and detection of spin polarized carriers in InGaN dots in GaN nanowires.

Chapter I

Introduction

1.1 Solid State Lighting: Background and Motivation

Edison's incandescent light bulb is one of the most important inventions in human history. It revolutionized indoor lighting, and fundamentally changed the way people live their lives by enabling vision easily across any space at any time. Vision, one of the most basic senses of the human body for the beauty it registers and its role in coordinating daily tasks, is sensitive to the range of the electromagnetic spectrum spanning from 390-700nm. The light produced by Edison's light bulb contained both the desirable visible light as well as wasteful infrared components. An incandescent lamp produces light by heating a filament (infrared emission) to a high temperature by passing electric current through it until it glows, resulting in very poor efficiencies. Fluorescent lamps reduce the energy lost as invisible IR light by concentrating light production in the visible spectrum. However, the parasitic energy losses during light production from mercury discharge are significant and additionally, the mercury remnant after-use is a toxic waste. The use of solid state semiconductors in the form of light emitting diodes (LEDs) further reduces parasitic energy losses during light production by converting electricity directly into light in the visible wavelengths through the radiative recombination of electron hole pairs. Nitride based LEDs emit in the visible spectrum as

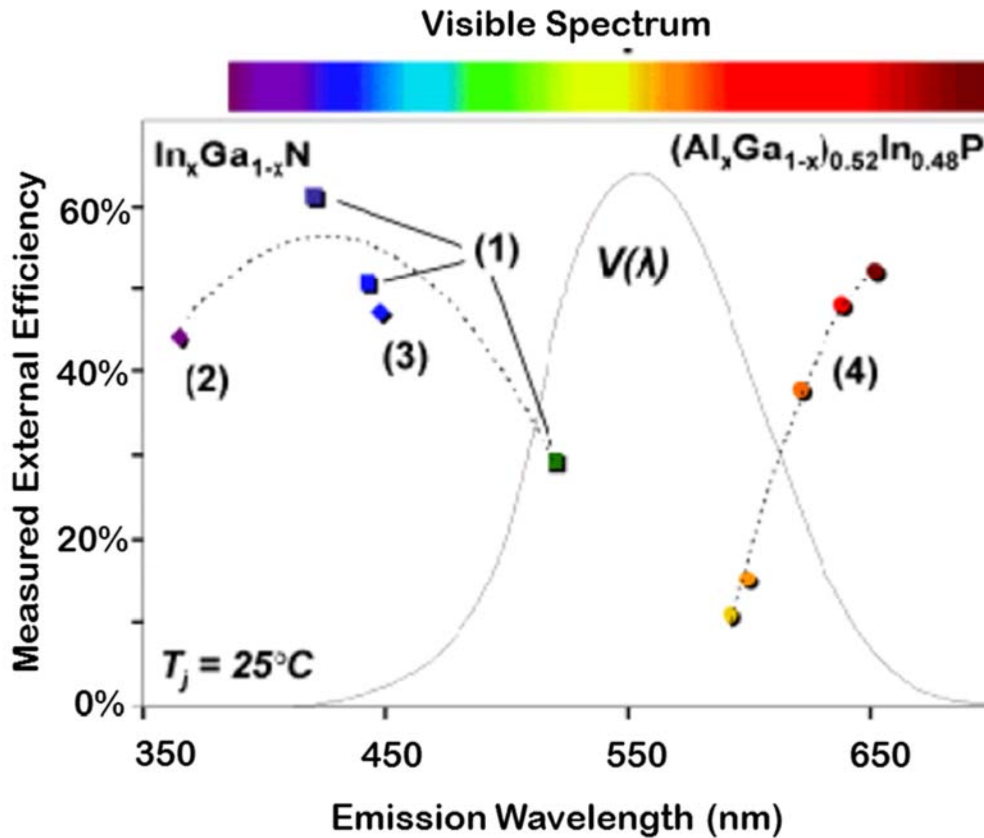

Fig. 1.1. Measured external quantum efficiencies for state-of-the-art LEDs emitting in the visible spectrum [1].

they are direct and wide band-gap semiconductors. Fig. 1.1 shows some of the recent measured efficiencies of nitride and phosphide LEDs at various wavelengths. While (Al,Ga)InP-based LEDs can emit in the red wavelengths, it is impossible to cover the visible spectrum with this material as seen from Fig. 1.1. The (In)GaN LEDs, on the other hand, can emit across the whole visible spectrum by varying In composition in the InGaN active region. The traditional problem of the "green gap" (Fig. 1.1) arises because the radiative efficiencies of green emitting InGaN active region reduces drastically with higher In incorporation and there is an absence of any other material system to provide high efficiency blue or green wavelength emission. The challenges

involved in getting longer wavelength emission from the nitrides and the approach used in this thesis is discussed later. Solid state lighting is the most energy efficient technique and has revolutionized lighting over the last decade. Its research and development has been relentlessly pursued and it has been replacing the conventional lighting in all spheres of human life at a steady pace. The efficacy of a light source is measured in lumens/watt (lm/W). Lumens is the measure of the amount of light output taking into account the sensitivity of human eye to various wavelengths and the efficacy is this amount of light output per injected electrical power. Fig. 1.2 describes how the usage of an LED can be extremely energy efficient compared to conventional light sources.

Fig. 1.2. Energy efficiency of a solid state nitride LED compared to incandescent and compact fluorescent lamps [2].

An LED is a semiconductor light source where the injected electrons and holes recombine within the device to give out light or photons. The first practical visible-spectrum (red) LED was developed in 1962 by Nick Holonyak Jr. [3]. Different material systems have been utilized for generating different light emission in the visible regime. The first visible LEDs were realized by using Gallium Arsenide Phosphide (GaAsP) on GaAs substrates in the 1960s. The further development includes green-emitting gallium

phosphide (GaP) LEDs and yellow-emitting silicon carbide (SiC) LEDs, although they are very inefficient. High efficiency LEDs appeared when gallium aluminum arsenide phosphide (GaAlAsP) and aluminum indium gallium phosphide (AlInGaP) were used for making red and yellow LEDs in 1990s. Blue-emitting LEDs were a must to produce white light for visible applications. The first high-brightness blue LED was demonstrated

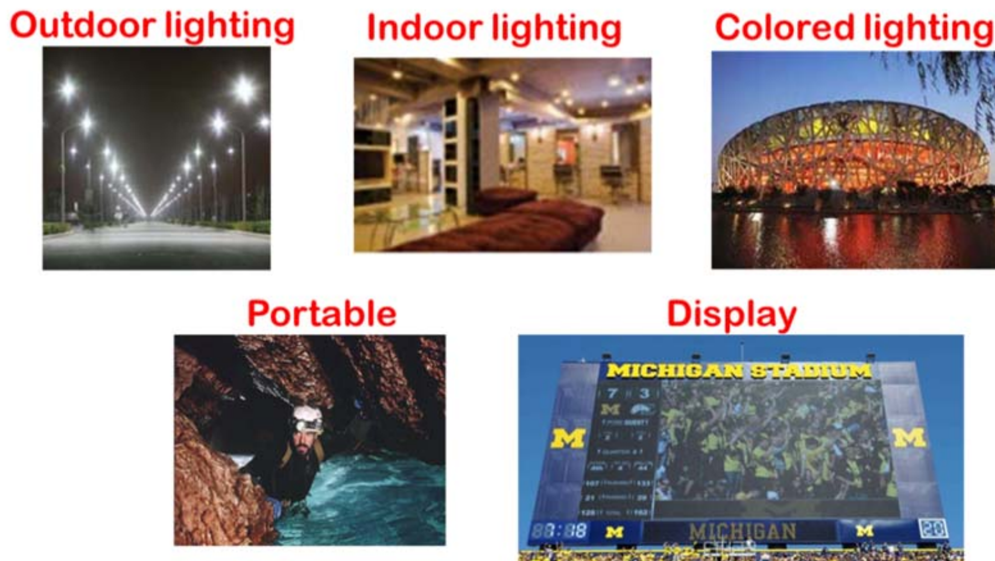

Fig. 1.3. Applications of nitride-based visible LEDs.

by Shuji Nakamura of Nichia Corporation in 1995 and was based on indium gallium nitride (InGaN) [4]. This was an extremely promising development because of its potential in providing high efficiency blue emission and also the possibility of providing longer visible wavelength emission including green and red by incorporating a higher In composition in the InGaN active region since (In)GaN is a direct, wide bandgap semiconductor. Its development was built on critical developments in GaN nucleation on sapphire substrates [5, 6] and the demonstration of p-type doping of GaN [7, 8]. Since then, blue LEDs have been combined with yellow phosphors to produce white light [9] used for solid state lighting. LEDs also find use in colored decorative lighting, portable

light sources and displays as shown in Fig. 1.3.

One of the other important applications of nitrides in visible light sources is in visible lasers. The first blue-emitting InGaN lasers were demonstrated by Nakamura *et. al.* [10] in 1996. It became increasingly difficult to obtain lasing at longer wavelengths. The problems associated with higher In incorporation for obtaining longer wavelengths will be discussed later in subsequent chapters. It was only as recent as March 2009 that the first InGaN/GaN quantum well (QW) based green-emitting laser was demonstrated [11]. Although the initial progress was slow, the recent demonstration of blue and green lasers have seen their applications increase in wide areas including optical data storage, pico-projectors, astronomy, military dazzlers, medical prostatectomy and heads-up displays used in automobiles, as shown in Fig. 1.4.

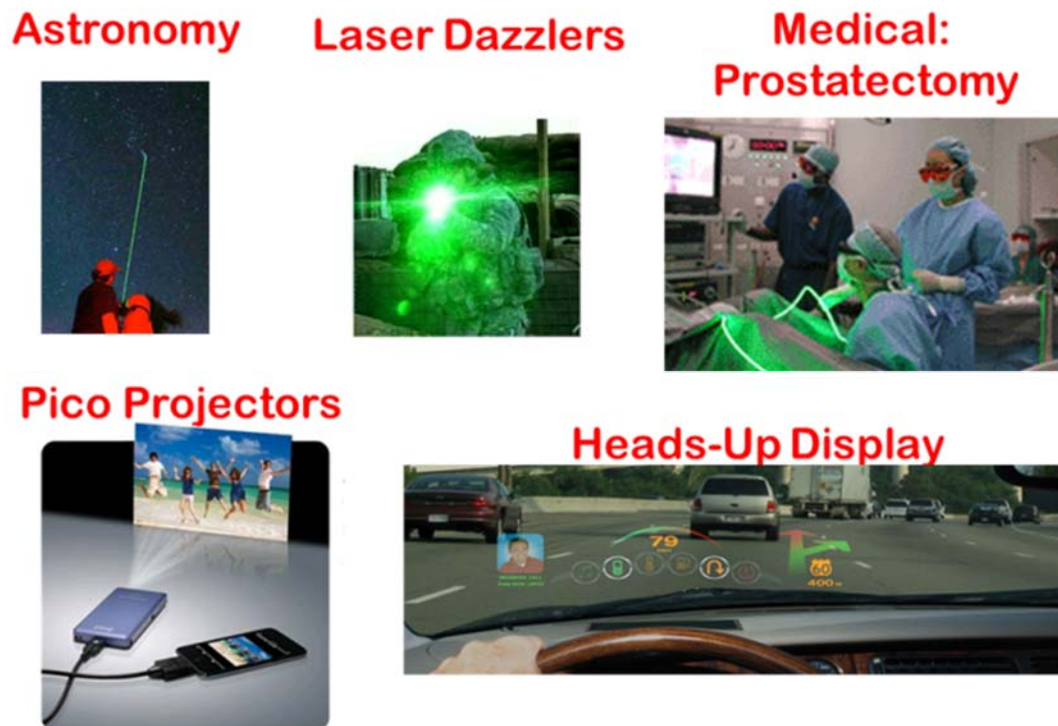

Fig. 1.4. Applications of nitride-based visible lasers.

1.2 History of III-Nitride Research and DOE Roadmap

Since the demonstration of the first InGaN blue LEDs, there has been enormous improvement in the efficacy and production of white light sources. White light sources can be achieved in two ways: 1) by mixing different proportions of blue, green and red emitting active regions in LEDs to tune the white light emission; and 2) coating a high brightness blue LED with a yellow phosphor to produce white light [8]. The persistent problem of the "green-gap" has promoted the adoption and steady pursuit of the second approach using phosphors to generate white light. Fig. 1.5 shows the exponential rise in nitride LED revenue, powered by the ever-increasing demands for solid state lighting. The nitride LED industry is at a threshold where it is facing serious challenges in its drive to replace all the existing conventional lighting sources and ushering in a lighting revolution not seen since the advent of Edison's incandescent lamps.

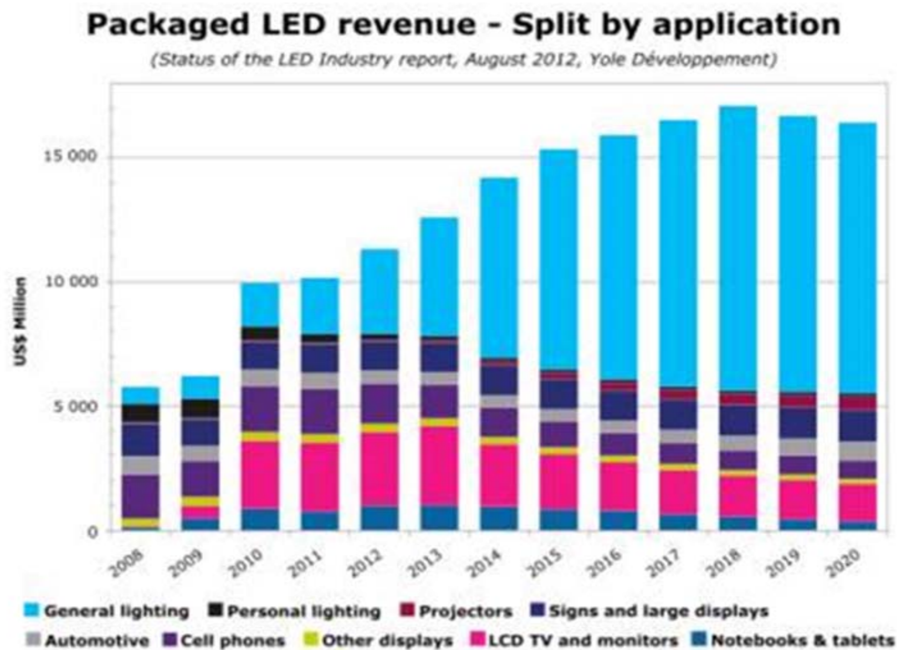

Fig. 1.5. Packaged nitride LED revenue.

The research in the nitride material system dates back to as early as 1969. The initial research in the 1970s and 1980s focused on studying the optical properties of the material but the inability to grow a thick single crystal GaN epitaxial layer with a flat surface free of cracks remained a major roadblock in making practical devices out of them. During this period, the lack of good epitaxial growth techniques coupled with issues of p-type doping in GaN due to high residual background doping impeded practical applications of the material system. It was not until the late 1980s that high crystalline quality GaN growth techniques were developed on readily available mismatched substrates including sapphire and SiC through the use of low temperature AlN buffer layers in chemical vapor deposition (CVD) chambers. The first demonstration of p-type doping in GaN using high incorporation of Mg subsequently led to the first demonstration of high brightness InGaN/GaN blue LEDs in 1989 by Amano *et. al.* and Nakamura *et. al.* [12], then working at Nichia Corp., in 1993 reported InGaN blue LEDs with recorded external quantum efficiency (EQE) of 0.18% and an external output power of 42 μW at 20 mA forward current. Continuous and relentless research resulted in the introduction of the AlGaN electron blocking layer (EBL) in 1993 followed by the utilization of InGaN QW active region instead of double heterostructure which resulted in demonstration of high output power (1.5 mW) blue LEDs [13]. This ensured high power and efficiencies despite the use of mismatched substrates such as sapphire having large propagating dislocation densities of 10^{8} – 10^{10} cm^{-2}. Steady improvement in the LED heterostructure design, epitaxy, processing and optimization of the chip design using a "flip chip" design [14] has led to an enormous increase in the output power to > 150 mW/mm^{2} and EQEs as high as 45% in blue LEDs in recent times

[15]. While companies like Phillips and Nichia have championed the use of GaN/sapphire for their LED technology, Cree has progressed with GaN/SiC technology and Soraa has recently started developing GaN/GaN substrates for their commercial LEDs. Longer wavelength emission is much more challenging as will be discussed in subsequent chapters, although recent commercial green LEDs have been demonstrated with output power as high as 37 mW/mm^2 [15]. As shown in Fig. 1.6, the Department of Energy (DOE) roadmap predicts a white LED source output goal of >

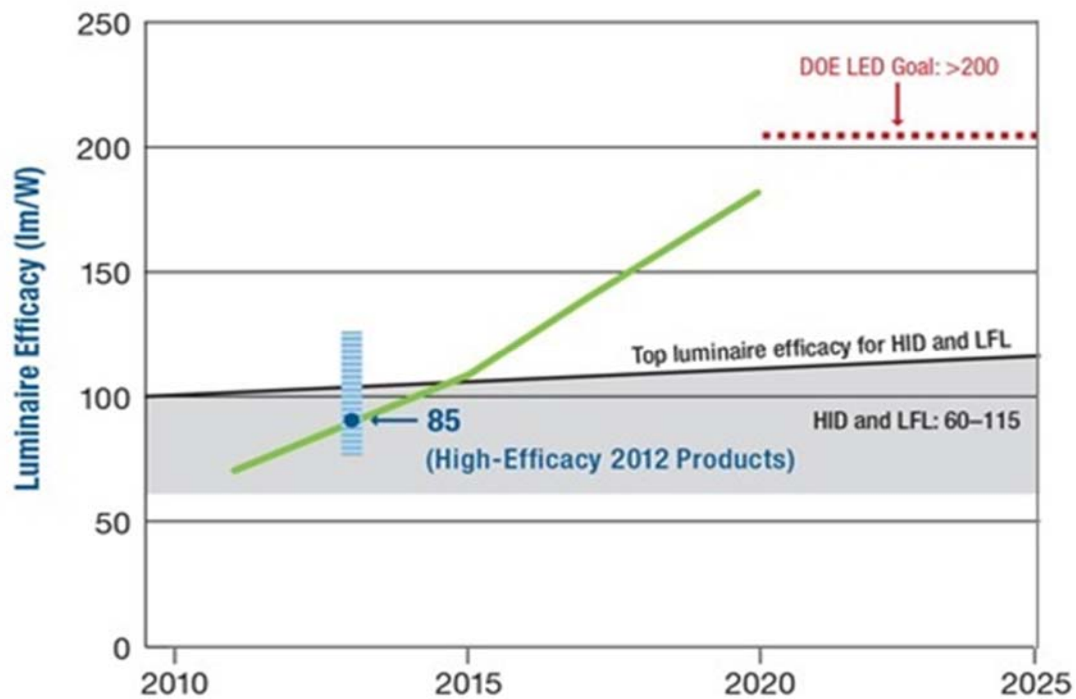

Fig. 1.6. DOE goal for solid state LEDs as compared to high intensity discharge (HID) and linear fluorescent lamps (LFL).

200 lumens/watt within the next decade. The 70-120 lumens/watt of light output produced by current white LED sources is already higher than that produced by high intensity discharge (HID) and linear fluorescent lamps (LFL), and the DOE further recognizes the potential of this technology in saving both costs and carbon emissions.

The DOE has been investing enormous amount of money to realize the full potential of the LED technology. Similar large scale research efforts have seen the successful commercialization and improvement of blue lasers since 1995 and green emitting InGaN lasers since 2009.

1.3 Challenges Facing III-Nitride Research

1.3.1 Availability of substrate for gallium nitride growth

The GaN industry needs to further improve the efficacy of the devices and get a high yield on a large size wafer to reduce costs, reach the DOE goal and make this alternative solid state lighting affordable for mass applications. The best substrate for growth of LEDs or lasers should be GaN. However, traditional crystal growth techniques used in Si and GaAs are not applicable for bulk GaN crystal growth. From its phase diagram, GaN only melts above 2500 °C at a pressure higher than 4.5 GPa while at low pressures, it decomposes into Ga and N_2 before melting.

Substrate	Lattice mismatch to GaN (%)	Thermal conductivity ($Wm^{-1}K^{-1}$)
GaN	0	130
6H SiC	3.4	490
Sapphire	13	7.5
Silicon	17	3.59

Table 1.1. Different substrates used for nitride LED and laser epitaxy.

As a result, large GaN crystals are typically grown on foreign substrates including sapphire, SiC or Si. However, the large lattice mismatch that the foreign substrates have from GaN, as shown in Table 1, results in the creation of a large dislocation density (10^8

– 10^{10} cm^{-2}). Such a high defect density degrades the GaN LED and laser performances significantly through the creation of non-radiative recombination centers in the lines and parallel paths for electron hole transport resulting in heating of the devices and large leakage. Red-emitting GaAs based devices would not even have any significant radiative recombination with such high defect densities, but the unique properties of nitrides still make them very favorable for making solid state lighting sources on substrates with such high dislocation densities. This makes the design, growth and demonstration of high performing LEDs and lasers on these substrates very challenging.

1.3.2 Efficiency droop in blue and green light emitting diodes

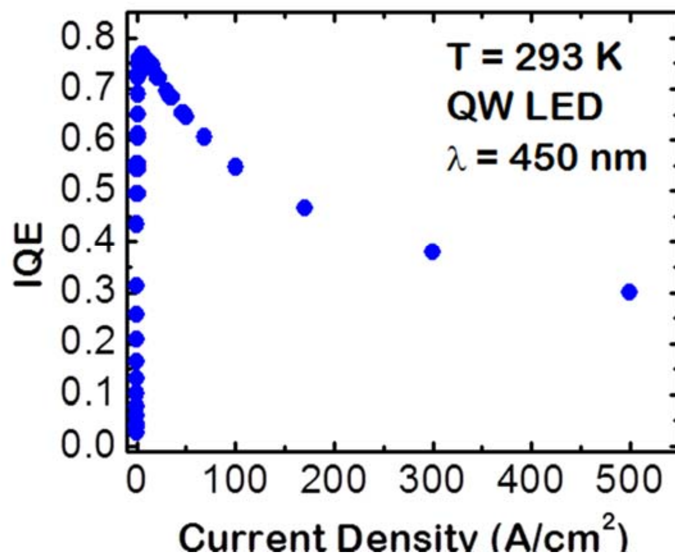

Fig. 1.7. Efficiency droop observed in state-of-the-art c-plane quantum well LEDs.

One of the biggest problems plaguing the solid state lighting industry is the huge drop in efficiency of LEDs at elevated current injections which are required for high brightness applications, a phenomenon termed as “efficiency droop”. Fig. 1.7 shows the

efficiency droop observed in state-of-the-art c-plane quantum well LEDs at high current densities. The QW LEDs were processed and characterized along with quantum dot (QD) LEDs whose results will be discussed later. The problem is particularly severe for green-emitting QW LEDs where the peak efficiencies are much lower than those seen in blue-emitting devices and the resulting efficiency at high injections after droop reaches very low values limiting practical applications. There has been a widespread research into the origin of the "droop" phenomena and into proposing solutions to alleviate it. It has been attributed to several mechanisms including the non-radiative Auger recombination [16], electron leakage from the QW active region [17], device self-heating [18] and exciton dissociation [19]. It was in 2008 that Krames *et. al.* [20] working at Phillips Lumileds first proposed Auger recombination as the main reason behind the observed efficiency droop. The results were substantiated by several other groups in the following years including lifetime measurements by Drager *et. al.* [21] and large signal modulation turn-on delay measurements on laser diodes by Bhattacharya *et. al.* [22]. Others [23, 24] put the blame of efficiency droop on leakage of electrons beyond the electron blocking layer. Efficiency droop was shown to be independent of ambient temperature ruling out device self-heating as a possible reason [25] while exciton dissociation resulting in droop behavior has not been demonstrated through experimental techniques. Several proposed mechanisms for "efficiency droop" essentially originate from the large polarization field in wurtzite structured III-nitride based semiconductors.

1.3.3 Large lasing threshold and longer wavelength lasing in (In)GaN lasers

The first InGaN-based laser diodes (LDs) were demonstrated by Nichia Corp. on c-plane GaN in 1995, emitting at 400 nm. Since then there has been relentless research and

development to increase the lasing wavelength to longer wavelengths including green by groups in Corning, Nichia Corp., Osram, Rohm, Samsung, Sharp, Sony, Soraa, Sumitomo, and at the University of California Santa Barbara (UCSB). It was only as recent as 2009 that first green-emitting LDs (λ=500 nm) were demonstrated [26].

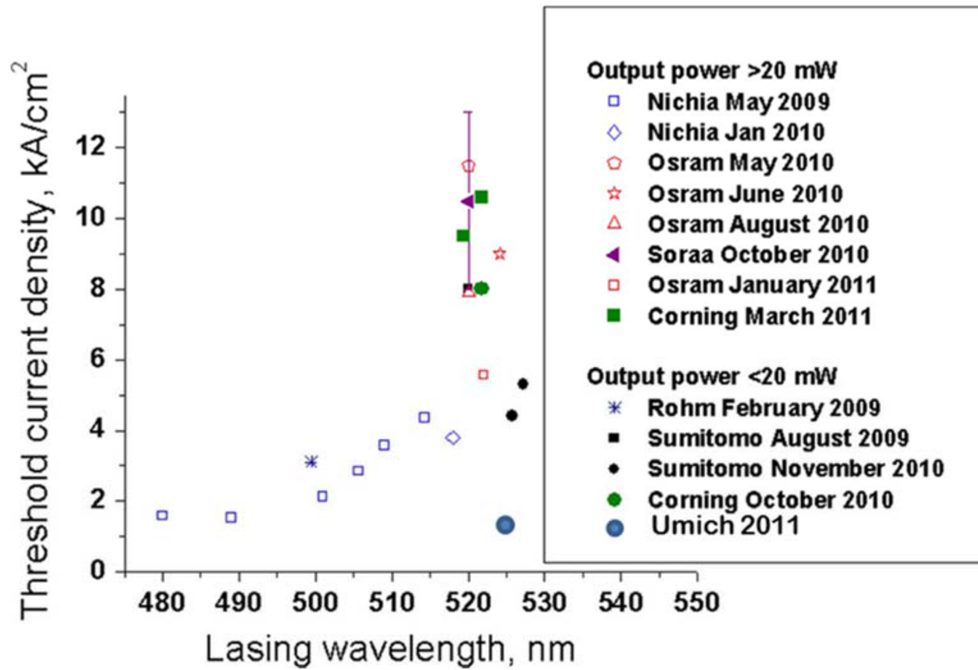

Fig. 1.8. Threshold current density for CW lasing at longer wavelengths by several groups [Modified from 27].

However, one of the biggest challenges the community is facing is to keep the threshold current density low especially for longer wavelength lasing, as shown in Fig. 1.8. There are several reasons responsible for increasingly high threshold current density with increasing wavelengths.

Lasing at longer wavelengths can only be attained by incorporating increasingly higher In composition in the QWs. This is challenging, because of the lower growth temperature required. Additionally, larger strain, polarization field and clustering results from increased In incorporation in the QWs. Secondly, the rough surface morphology due

to growth kinetics [28] and In alloy composition fluctuation in the InGaN QW active region [29] causes progressively broader spontaneous emission spectrum with increasing wavelengths due to the higher In incorporation. This broadening reduces the peak optical gain required to overcome the losses in the laser cavity. The third, and perhaps the biggest challenge, is to reduce the large piezoelectric polarization field in the active region especially at longer wavelengths which cause electron leakage and poor optical gain due to the quantum confined Stark effect (QCSE) [30].

1.3.4 Issues with p-doping

As was outlined in section 1.2, the progress in the field of nitrides was extremely slow during the 1970s and 80s mainly due to the inability in growing p-doping of GaN. This was mainly because of high n-type background doping of GaN during its crystal growth in MOCVD related to oxygen impurity incorporation and N-vacancies. Much of the initial progress in GaN crystal growth was done using CVD, and the interstitial incorporation of hydrogen in the crystal during MOCVD growth of GaN prevented activation of the most suitable acceptor dopant Mg by forming a Mg-H complex. A post-thermal annealing technique to achieve CVD grown p-GaN was discovered by Nakamura *et. al.* [31] in 1992 which paved the way for the demonstration of the first GaN LEDs and lasers. High levels of p-doping was still not easily attainable using CVD mostly because of the high activation energy and consequently, poor doping efficiencies of Mg. Molecular beam epitaxy (MBE) growth of highly p-doped GaN (2×10^{18} cm^{-3}) was demonstrated by Bhattacharya *et. al.* [32] at a low substrate temperature under N_2-rich conditions preventing the formation of nitrogen vacancies and in the absence of hydrogen under high vacuum yielding very high p-doping levels in GaN.

1.3.5 Large polarization field and associated problems

GaN is a polar crystal and has a wurtzite shape with alternating planes of Ga and N atoms, as shown in Fig. 1.9. Because of the high electronegativity of the N atoms, the wurtzite structure is more polar (or asymmetric) compared with other conventional semiconductors like GaAs. This creates a very large spontaneous polarization field in the nitrides. The polarization charges accumulate at the heterointerfaces especially at the AlGaN/GaN interface and can lead to a spontaneous polarization field as high as 2 MV/cm [33]. Many designs of high electron mobility transistors are based on such charge accumulation.

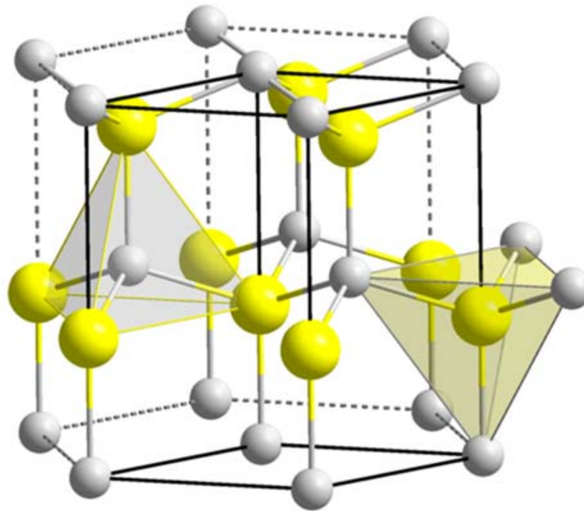

Fig. 1.9. Polar wurtzite crystal structure of GaN.

The other type of polarization, the piezoelectric polarization, plays a more significant role in InGaN/GaN LEDs and lasers as the spontaneous polatization is low for InGaN/GaN heterostructures. This field is caused by the displacement of the anion sub-

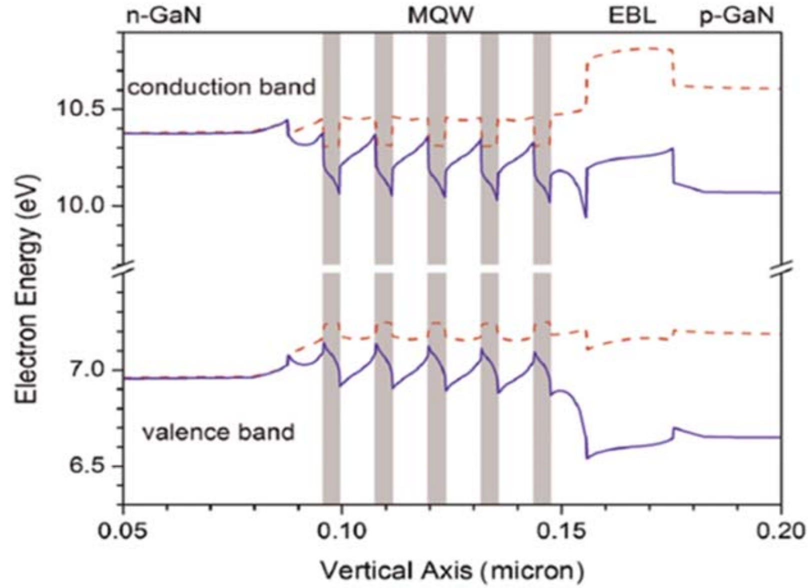

(a)

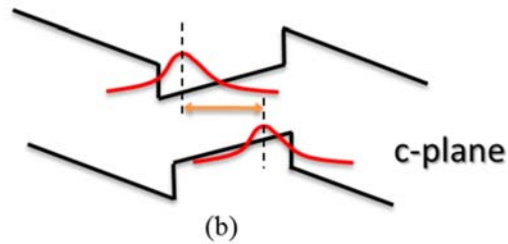

(b)

Fig. 1.10(a) Simulated band diagram of a typical InGaN/GaN multi quantum well (QW) LED with (solid line) and without (dashed line) polarization field; (b) Electron hole wavefunction separation in c-plane InGaN/GaN QW due to polarization field [33].

lattice and the cation sub-lattice due to the large strain developed at the heterointerface because of the coherent strain resulting from the growth of lattice mismatched layers. The biggest problems from the large polarization fields are the associated band bending as shown in Fig. 1.10 (a) for a conventional InGaN/GaN QW LED with AlGaN electron blocking layer (EBL). The large field in the InGaN QW region (shaded) causes the bands to bend in a way such that potential barrier to electron leakage on the p-side is reduced causing very high leakage thereby assisting in Auger recombination and contributing to

droop. Secondly, the AlGaN EBL is pulled down reducing its electron blocking effect. Additionally, a large triangular potential barrier is formed on the valence band which causes non-uniform injection of holes across the multiple well layers with the first few QWs from the p-side getting filled first before subsequent QWs receive any hole carriers. The most harmful effect of this polarization field in InGaN QWs is possibly the separation of electron-hole wavefunctions resulting in poor radiative efficiencies, as shown in Fig. 1.10 (b). The situation aggravates with higher In composition indicated by very poor peak radiative efficiencies of green-emitting InGaN/GaN QWs. This large polarization field in the InGaN/GaN QWs is screened at high carrier densities resulting in flat bands causing blue-shift of the emission peak. This effect is called quantum confined Stark effect (QCSE) and is responsible for huge shift in peak emission wavelengths (~20 – 30 nm) for QW LEDs and lasers.

There have been efforts to reduce the polarization field by using lattice-matched InGaN/InAlGaN quantum wells [34], by replacing the strained InGaN/GaN wells with a double heterostructure design [35], by growing the device heterostructures on non-polar and semi-polar substrates, or by applying external tensile stress on the substrates [36]. InGaN QW LEDs and lasers emitting in the blue and green wavelengths grown on non-polar or semi-polar GaN substrates have been demonstrated. The results are promising as they show reduced droops in LEDs and lasing at longer wavelengths. However, these devices suffer from low peak efficiencies in LEDs and high lasing threshold in the lasers [37-39]. Bhattacharya *et. al.* has pioneered the use of quantum dots as the gain material to reduce the polarization field as discussed subsequently.

1.4 Our Approach: Use of Quantum Dots

The challenges faced by the nitride research community are enormous and many of them can be solved by reducing the polarization field present in the active region. Several alternative techniques to reduce polarization field have been widely researched as has been outlined in section 1.3.5. Our approach in this dissertation research centers on using self-assembled InGaN/GaN quantum dots (QDs) as the active region. The self-assembled InGaN/GaN QDs form when sufficiently strained InGaN layers undergo 2D-3D strain relaxation via the Stranski-Krastonow growth mode. The strain relaxation in the active region results in reduced piezoelectric polarization field in the QDs resulting in strong electron-hole wavefunction overlap. This leads to a large radiative recombination rate, and high radiative efficiencies. All other problems associated with large polarization field in the wells can be drastically reduced by using such dots in the active region. Furthermore, the spatial localization of carriers also prevents them from reaching the existing defect centers which can act as centers of non-radiative recombination. The longer wavelength dots are more easily attainable because of the lower inherent strain in the active region during growth. These superior optical properties of QDs can be realized by controlling their growth and structural properties as will be discussed in details in chapter II. Bhattacharya et. al. have led the research efforts in realization of QD-based nitride LEDs and lasers although there have been several other groups who did early research on the properties of QDs and QD-based LEDs [40-42].

The use of quantum dots assumes more significance in terms of solving some of the most pressing issues facing the development of nitride lasers. The InGaN QWs on c-plane and semi- or non-polar GaN suffer from large threshold density which needs to be

lowered as it is critical in determining the power conversion efficiency. The use of dots in the active region provides both higher gain and differential gain due to their altered density of states which is expected to reduce threshold current density and produce large output power at relatively low current densities. Bhattacharya et. al. [43] and others [44] have demonstrated In(Ga)As/Ga(Al)As QD lasers with wide tunability of output wavelength, ultra-low threshold current, large modulation bandwidth and near-zero chirp and linewidth enhancement factors [43]. The superior properties of the nitride QDs would be even more important because of their role in mitigating the large polarization field inherent in InGaN/GaN QW devices as discussed above.

The purpose of the present research was to realize the advantages of QDs in the visible LEDs and lasers through detailed and careful control of the QD properties by growth using MBE. An extensive study of the growth and properties of the QDs and QD-based devices were performed and discussed in details. The QDs can prevent the propagation of dislocations through them and can act as filters. The properties of such QD filters were extensively studied through material and device characterizations. Additionally, fundamental properties of InGaN/GaN dots in GaN nanowire on Si having similar dimensions as self-assembled dots were explored.

1.5 Dissertation Overview

This dissertation focuses on the development of optimum growth conditions through close control and in-situ monitoring of self-assembled InGaN/GaN QDs grown by MBE. The optimized QDs were then used as the active region for realizing LEDs and

lasers with superior optical properties compared with state-of-the-art QW devices. Some of the most challenging issues facing the nitride industry including droop, low efficiencies especially in longer wavelengths, high threshold density in lasers and large peak emission shift were addressed using QD-based devices. The role of QDs in dislocation reduction inherent in GaN on sapphire substrates used for state-of-the-art LED growth was demonstrated. Additionally, InGaN/GaN dots in GaN nanowires were grown and characterized having similar dimensions as self-assembled InGaN/GaN QDs. The properties of spin polarized carriers were measured in the dots-in-nanowires to determine their potential use in realizing spin-based devices.

Chapter II discusses growth optimization of the self-assembled InGaN/GaN QDs with high radiative efficiencies, low polarization field indicated by low QCSE, and small radiative recombination lifetimes in Veeco Gen II and Gen 930 plasma assisted MBE systems. The QDs were characterized by detailed transmission electron microscopy (TEM), atomic force microscopy (AFM), temperature dependent photoluminescence (PL) and time resolved PL measurements to determine their optical and structural characteristics.

The use of QDs as the active region in LEDs is reported in chapter III. The QD LEDs are optimized through improvements in the device design, QD LED heterostructure growth and improvement in device processing techniques to realize high performing blue- and green-emitting LEDs. Current-voltage (I-V) and light-output (L-I) measurements were performed on such devices. Additionally, differential carrier lifetime measurements were performed on high-speed QD LEDs and equivalent state-of-the-art

QW LEDs to compare the recombination dynamics of carriers in the active region under varying injection levels.

The role of QDs in reducing propagating dislocations originating from lattice mismatched GaN nucleation has been explored through material and device characterization in chapter IV. Bhattacharya *et. al.* were the first to report the properties of QDs in reducing the dislocation densities in the arsenide material system [45]. Significant improvements in the I-V and L-I characteristics were obtained for green-emitting LEDs on GaN/sapphire templates using InGaN QDs as dislocation filter.

Chapter V discusses the issues faced in realizing some of the first nitride QD-based lasers emitting in the blue and longer wavelengths. The challenges involved in growing high crystalline quality strained InGaN waveguide, AlGaN cladding, and well-controlled InGaN QD layers are studied through extensive material characterization. Detailed optical output characteristics of the nitride QD lasers have been measured and are reported in this chapter.

GaN nanowires can be grown relatively defect-free due to their large aspect ratio even on largely lattice mismatched Si substrates. The InGaN disk-like insertions in such nanowires are of similar dimensions to the self-assembled QDs. In chapter VI, the optical properties of the nanowires and InGaN dots in GaN nanowires were characterized including the measurement of spin properties of carriers for the first time in quantum confined nitride heterostructures under relatively defect free environment.

Chapter VII summarizes the work done in this dissertation and suggests some exciting future work using nitride QDs.

Chapter II

Growth and Characterization of Self-assembled InGaN/GaN Quantum Dots by Plasma-Assisted Molecular Beam Epitaxy

2.1 Introduction

The active region plays a significant role in determining the performance of optical devices including light emitting diodes (LEDs) and lasers. State-of-the-art nitride commercial LEDs and lasers have used InGaN/GaN quantum wells (QW) as the active region which provide stronger confinement and a higher radiative recombination rate of carriers compared to a double heterostrucure active region [46]. However, the large polarization field inherent in the nitrides coupled with the high dislocation density limit the performance of these QW devices, as discussed in chapter I. Alternatively, InGaN/GaN quantum dots (QDs) have been predicted and experimentally demonstrated to have stronger overlap of electron and hole wavefunctions compared to QWs resulting in increased radiative recombination and other superior optical properties [47-49]. This is because quantum dots form by strain relaxation of the InGaN layer, and therefore have a reduced in-built polarization field as compared to quantum wells. Additionally, spatial confinement and localization of carriers in QDs prevent their escape to dislocation centers present in the InGaN layers that can act as centers of non-radiative recombination. InGaN/GaN QDs have been demonstrated using Stranski-Krastonow (S-

K) growth, the employment of low temperature passivation [50], use of anti-surfactants [51] and post-growth fabrication including annealing etc. [52]. The growth of self-assembled InGaN/GaN QDs in plasma-assisted MBE [49, 53], NH_3 MBE [54, 55] and MOCVD [56] are by far the most promising method in terms of realizing the improved optical and structural properties of QDs. The commercial nitride LEDs and lasers are mostly grown in metal organic chemical vapor deposition (MOCVD) reactors and the use of molecular beam epitaxy (MBE) has generally lagged behind. In this work, high performance QD based LEDs and lasers have been realized by precisely controlling and studying the epitaxial growth of constituent layers in high vacuum MBE. This chapter focuses on the detailed and systematic growth study of the QD active region and their detailed optical and structural characterization ultimately essential for demonstrating improvements in LED and laser performances.

The Stranski-Krastanow island growth mode for self-assembled InGaN/GaN QD formation is achieved when a large lattice mismatch exists between the growing InGaN layer and the underlying GaN substrate via the formation of a 2-D island layer called the wetting layer. Other growth modes include Frank-van der Merwe (FM) [57] and Volmer-Weber [58] depending on the lattice mismatch and the interaction strength of the impinging adatoms with each other and the surface. The Volmer–Weber (VW) growth mode results in a 3-D growth of adatom clusters and islands as a result of adatom-adatom interactions being stronger than those of the adatom with the surface. This growth usually occurs when there is a large lattice mismatch (larger than that required for S-K growth mode). On the other hand, growth proceeds through Frank-van der Merwe (FM) growth mode when epilayers are grown lattice matched to substrate, resulting from adatoms

attaching preferentially to surface sites forming atomically smooth, fully formed layers. This layer-by-layer growth is two-dimensional, indicating that complete films form prior to growth of subsequent layers [59, 60]. Stranski–Krastanow growth is an intermediary process characterized by both 2D layer and 3D island growth [61]. All the three growth modes are shown schematically in Fig. 2.1.

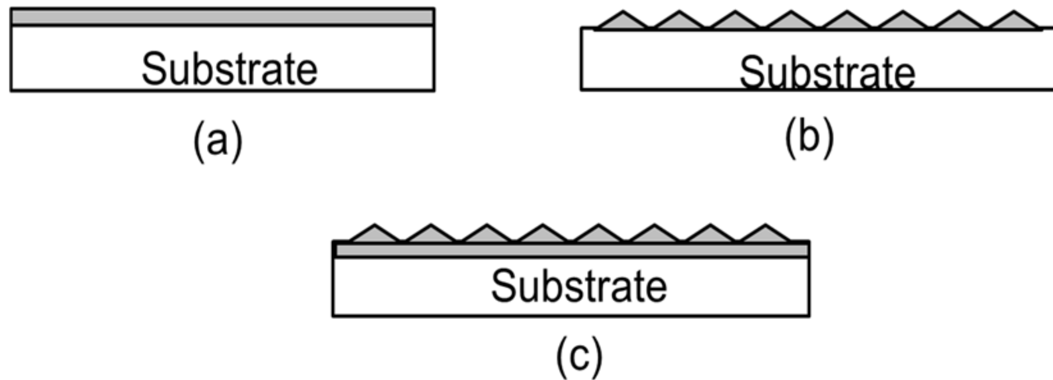

Fig. 2.1. Schematics of three different growth modes: (a) Frank-van der Merwe (FM), (b) Volmer Weber (VM) and (c) Stranski-Krastonow growth modes.

It has been reported that growth of InGaN on GaN by MBE has a 2D – 3D Stranski-Krastanov (S-K) growth mode transition above a critical In composition of ~ 12 % resulting in formation of self-organized InGaN QDs [62]. An extensive growth study of blue-emitting self-assembled $In_{0.18}Ga_{0.82}N$/GaN QDs (λ_{peak} ~ 420nm) on GaN/sapphire templates (dislocation density ~ $1x10^9$ cm^{-2}) was performed along with detailed structural and optical characterization to obtain superior optical performance of QDs. The optimized conditions for the growth of blue $In_{0.18}Ga_{0.82}N$/GaN QDs were then used to derive optimum conditions for green emitting $In_{0.3}Ga_{0.7}N$/GaN QDs on GaN/sapphire templates and visible QD LEDs emitting in both blue and green wavelengths were made

as reported in chapter III. The growth conditions were reproduced on GaN free-standing substrates having threading dislocation densities ~5x10^5 cm^{-2} and their optical properties extensively characterized and reported later in this chapter. Structural characterization of the QDs for growth optimization was performed using atomic force microscopy (AFM) and transmission electron microscopy (TEM) measurements. Temperature dependent and time resolved photoluminescence (PL) measurements were performed by exciting the samples with the frequency tripled output of a mode-locked Spectra Physics Tsunami Ti:Sapphire laser at 267 nm. Optimized InGaN QDs emitting in both the blue and green wavelengths were eventually used to grow, fabricate and characterize visible LEDs and lasers as reported in subsequent chapters.

2.2 Growth and Characterization of n-doped GaN Buffer

The growth of self-assembled InGaN/GaN QDs was carried out in Veeco Gen II and Gen 930 plasma-assisted molecular beam epitaxy systems (PA-MBE). The Gen 930 MBE system used in our lab is shown in Fig. 2.2. Both the Veeco Gen II and Gen 930 RF plasma-assisted molecular beam epitaxy (MBE) systems are equipped with standard Ga, In, Al, Mg, and Si cells, and an rf UNI-Bulb nitrogen plasma source. All our samples were grown on substrates with ~4 μm of Si-doped hydride vapor phase epitaxy grown (0001) GaN on top of c-plane sapphire. The threading dislocation density in the substrates is ~1 x 10^9 cm^{-2}. Before growth, the substrates were first cleaned with standard solvents (TCE, acetone, IPA) and thermally degassed in two steps of 200 ° C/ 60 min followed by 450 ° C/ 60 min to reduce surface contamination. The growth temperature was measured by an infrared pyrometer, calibrated by the reflection high energy electron

diffraction (RHEED) transition of 7x7 to 1x1 of Si (111) substrates.

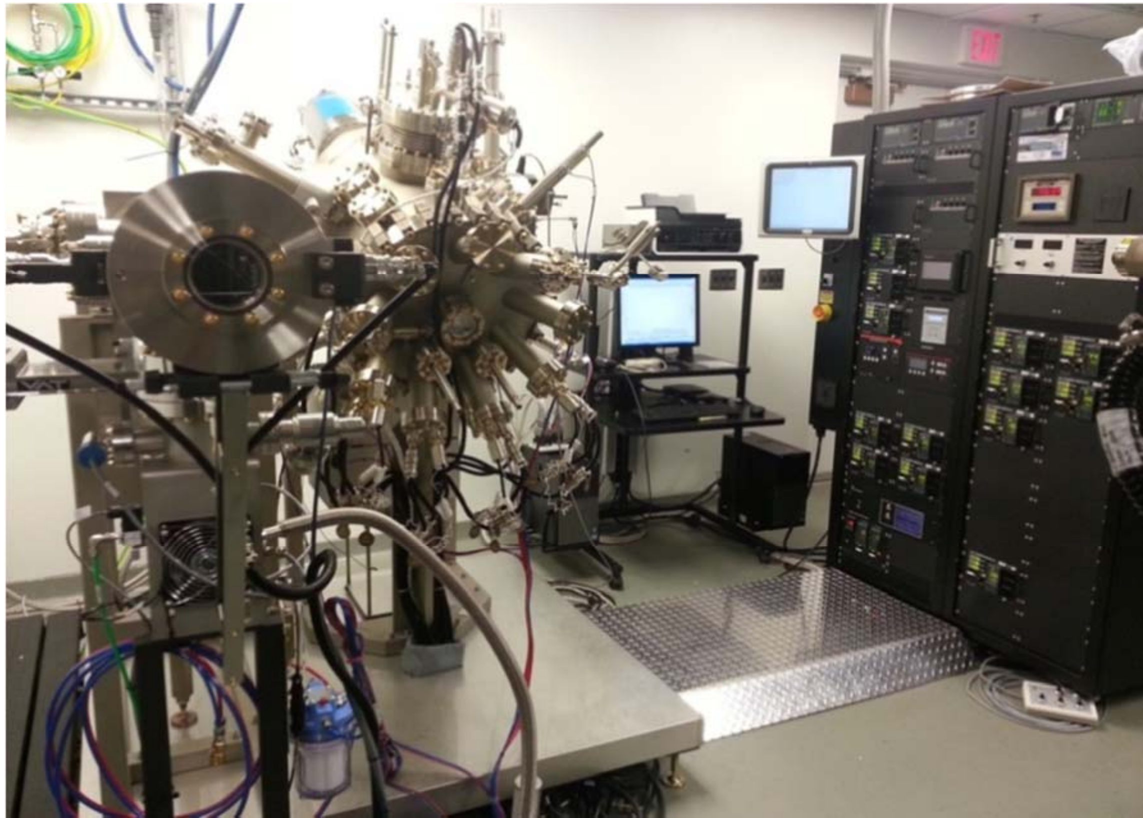

Fig. 2.2. Veeco Gen 930 Plasma-assisted molecular beam epitaxy (MBE) system in our lab.

The growth of a high quality n-doped GaN film is essential for growth of uniform quantum dots with high efficiencies. Typical heterostructures for growth optimization of the starting GaN buffer layer and InGaN/GaN QDs used in section 2.3 are shown in Figs. 2.3(a) and (b), respectively. To find the appropriate III/ V ratio for growth of high quality GaN films, 300 nm of Si-doped GaN layers were first grown under different Ga fluxes (Φ_{Ga} = 2.5 to 5 nm/ min) (Fig. 2.3(a)) while keeping the nitrogen flux fixed at 0.5 sccm

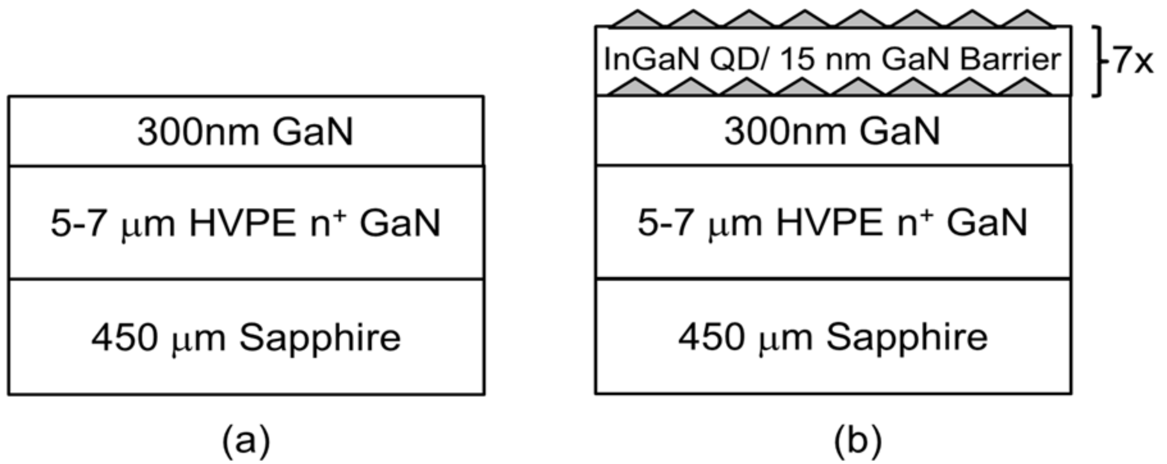

Fig. 2.3. Schematics of typical heterostructures for optimizing (a) underlying GaN buffer layer and (b) InGaN/GaN QD growth conditions for optical and structural characterization.

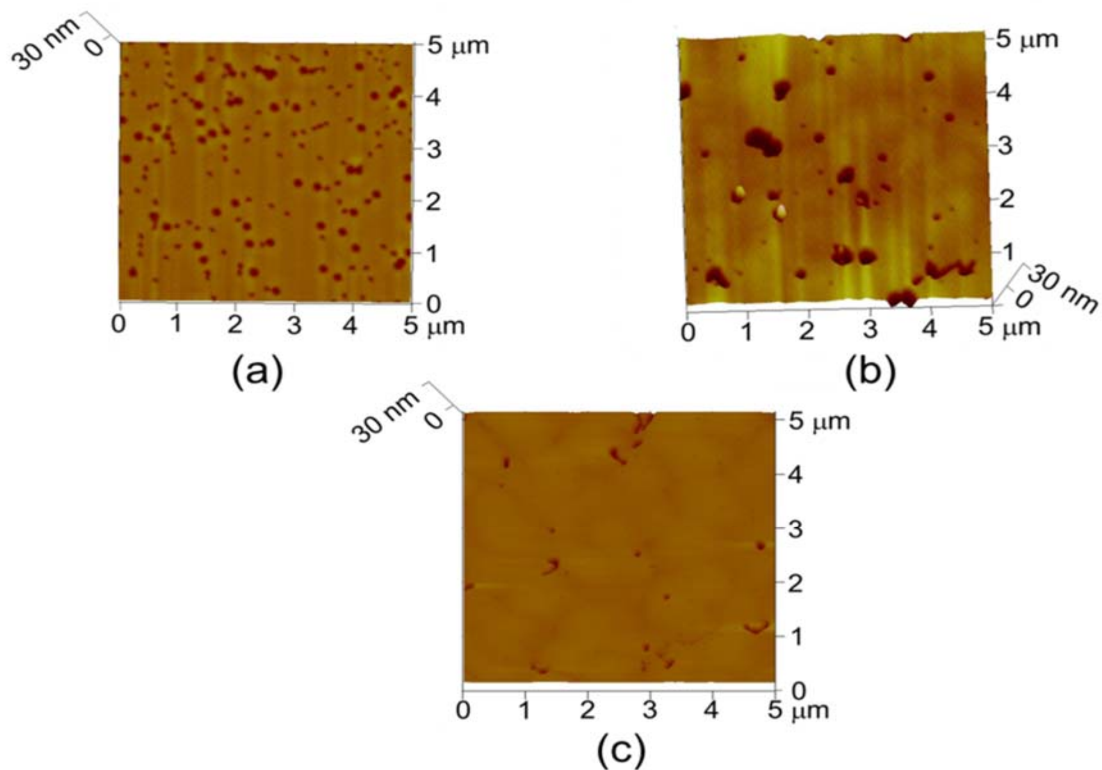

Fig. 2.4. Atomic force microscopy (AFM) images of 300 nm of n-doped GaN layer grown on GaN/sapphire template with different Ga fluxes (a), (b) and (c).

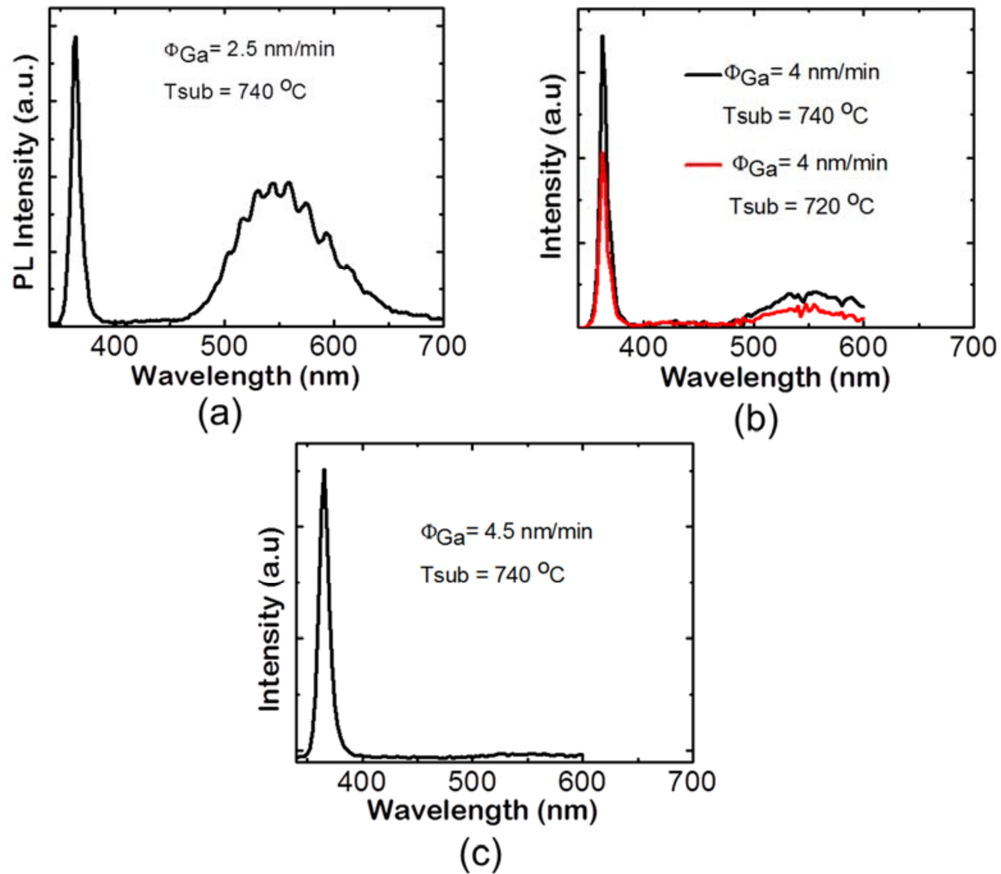

Fig. 2.5. Photoluminescence spectra of n-GaN band edge emission corresponding to Ga fluxes for which the AFMs are shown in Figs. 2.4 (a), (b) and (c).

with an rf power of 300 W at a substrate temperature of 740 ° C for all the epitaxial layers. In-situ RHEED characterization and ex-situ atomic forced microscopy (AFM) and photoluminescence measurements were used to determine the optimum III/ V ratio. At a constant substrate temperature, increase of Ga flux results in a streaky RHEED pattern, reduction of crystal defects and smoother surface morphology as seen from AFM measurements shown in Fig. 2.4. This is because the growth of nitrides using MBE is kinetically driven [63] and requires a presence of metallic bi-layer to reduce the kinetic barrier to adatom incorporation in a step-flow 2-D growth mode. Increasing the Ga flux

progressively from Φ_{Ga} = 2.5 nm/min to 4 nm/min results in reduction of crystal defects as seen in AFM measurements in Figs. 2.4(a) and (b), respectively. This is also accompanied by a reduction of Ga-vacancy related yellow luminescence intensity compared to GaN band-edge emission as seen in Figs. 2.5(a) and (b), respectively. Figure 2.5(b) also shows a PL emission with Φ_{Ga} = 4 nm/min grown at a lower growth temperature T_{sub} = 720 ^oC. It can be seen from Figs. 2.4(c) and 2.5(c) that the n-doped GaN layer grown with Φ_{Ga} = 4.5 nm/min at T_{sub} = 740 ^oC has the smoothest morphology with surface roughness ~0.5 nm and highest PL intensity with negligible yellow band luminescence. A further increase in Ga flux of more than 4.5 nm/min. results in micron-size metal droplet formation which degrades the growth quality (Fig. 2.6). It should be noted that the strong yellow luminescence is stronger than GaN bandedge emission on starting (0001)-GaN templates and is completely suppressed after growth of 300 nm of n-doped GaN at optimum growth conditions which indicate absence of any group III vacancies in MBE-grown GaN.

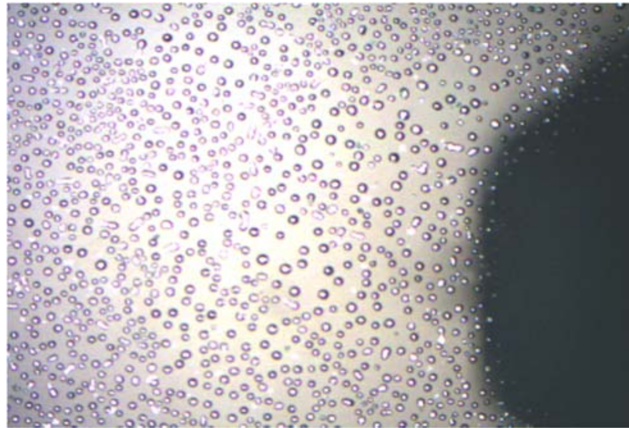

Fig. 2.6. A 10 μm x 10 μm micrograph of a GaN layer growth with metal droplet formation at Φ_{Ga} = 5 nm/min.

2.3 Growth Optimization of Self-Assembled InGaN/GaN Quantum Dots

After growth of 300 nm of Si-doped GaN layer (n ~ 1 x 10^{19} cm^{-3}) with Φ_{Ga} = 4.5 nm/min during which the RHEED pattern remained bright and streaky, the substrate temperature (T_{sub}) is lowered to 560 - 580 °C for growing strong blue emitting InGaN QDs under nitrogen rich conditions (F_{N2} = 0.7 sccm; rf power 380 W). The indium content of the QDs emitting at 420 nm is estimated at ~18 % based on x-ray diffraction (XRD) measurement of a relaxed InGaN calibration sample (equivalent pressure Φ_{Ga}:Φ_{In} ~ 2:1) of same In composition as the QDs. During the QD formation, number of InGaN monolayers (MLs) deposited should be larger than the critical thickness for strain relaxation to form QDs by S-K growth mechanism. It is found that the RHEED turns

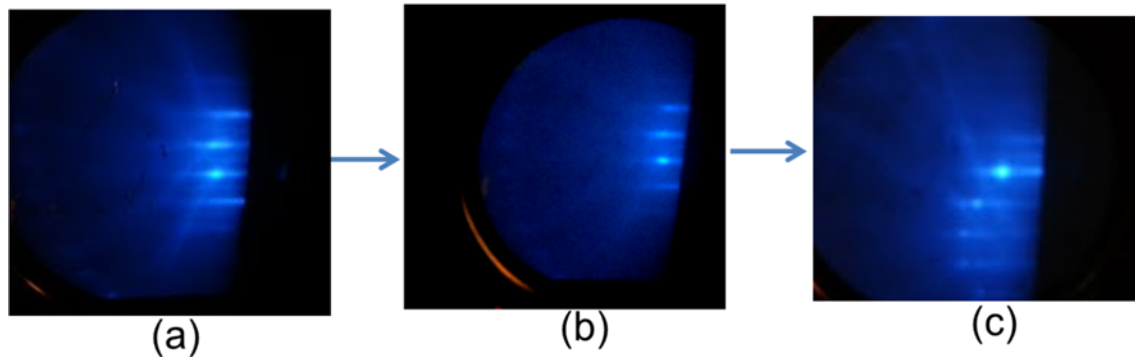

Fig. 2.7. In-situ RHEED characterization during QD formation showing the RHEED pattern changing from streaky (layer-by-layer growth) to spotty (QD or island formation) pattern at (a) t = 0s, (b) t = 15s and (c) t = 20s.

spotty ~18s after opening the In and Ga shutters for growth of the QDs with InGaN growth rate found close to 0.85 Å/s. Fig. 2.7 shows the change in the RHEED pattern during InGaN QD growth at (a) t=0s, (b) t=15s and (c) t=20s. This is followed by the growth of a 15 nm thick GaN barrier layer at the same temperature. Eight such pairs of

InGaN QDs and GaN barrier layers are grown and the growth parameters are optimized to obtain improved characteristics of multiple QD layers. For AFM characterization, samples were grown with the eighth layer of the QDs uncapped, as shown in Fig. 2.3 (b). Influence of InGaN deposition thickness (number of monoloayers (MLs) of InGaN grown), GaN spacer layer thickness between two QD layers and in-situ N_2 interruption times on the optical properties of QDs was determined.

Low temperature PL spectra on various samples were obtained by mounting the samples on liquid He cryostat. The topmost uncapped layers in the QD samples were characterized to determine the dimensions and aspect ratio of InGaN QDs using AFM measurements. PL decay times of QD samples were studied through a time resolved PL measurement performed using a Hamamatsu streak camera with an overall resolution of ~5 ps. PL decay times are fitted to obtain total carrier lifetimes for the QD samples.

2.3.1 Optimization of number of InGaN monolayers (MLs)

Room temperature photoluminescence (PL) intensity from eight layers of $In_{0.18}Ga_{0.82}N$/ GaN self-assembled quantum dots depend strongly on the number of InGaN MLs used to form quantum dots. The difference in in-plane lattice parameters between the $In_{0.18}Ga_{0.82}N$ epilayer and the GaN layer is $\Delta a/a = 1.85$ %. For this amount of strain, the critical thickness for the 2D – 3D growth mode transition is ~4 – 6 MLs [62]. Three QD samples were grown with ~9, 12 and 14 MLs of InGaN grown to form a self-assembled InGaN QD layer. Eight such layers of InGaN/GaN QDs were grown and characterized to see the effects of InGaN ML on structural and optical properties of the QDs. Highest PL intensity is obtained from the QD sample with 12 MLs of grown InGaN as seen in Fig. 2.8 (a). A 1x1 μm^2 AFM scan of topmost eighth layer of uncapped InGaN

QDs show that the QDs have a base diameter of ~30 nm and height of ~4 nm, with a typical dot density of ~5 x 10^{10} cm^{-2}. For QDs grown with 14 MLs of InGaN, the PL

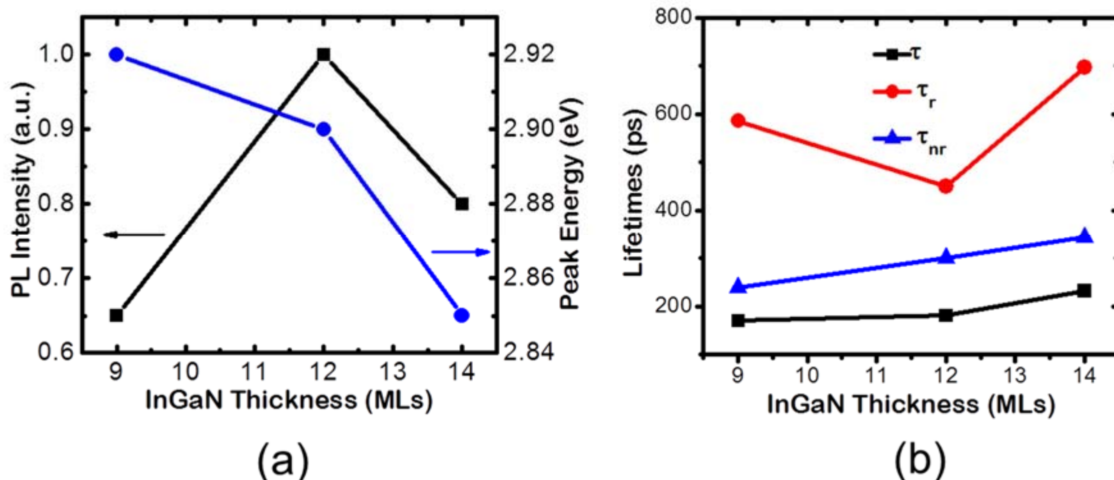

Fig. 2.8. Influence of the number of monolayers (MLs) of InGaN deposited to form QDs on its (a) PL intensity and peak energy, and (b) lifetimes.

intensity from the same number of dot layers (eight) was found to be lower. This is possibly due to a larger dot size resulting from increased growth time. Large sized QDs result in reduced e-h wavefunction overlap which is confirmed by longer radiative carrier lifetimes measured on these samples (Fig. 2.8(b)). Growth of QDs with only 9 MLs of InGaN results in formation of incomplete QDs with reduced size (height ~2.25 nm, base ~ 30 nm) and low aspect ratio resulting in lower PL intensities due to electron wavefunctions extending into barrier regions [47]. An optimum number of MLs is required to obtain QDs with highest intensities. For blue emission, ~12 MLs of $In_{0.18}Ga_{0.82}N$ are optimum to obtain QDs having strong intensities and efficiencies.

2.3.2 Optimization of N_2 growth interruption time for each dot layer

After the growth of 12 MLs of the InGaN layer on GaN at 560 ^{o}C to form the QDs, growth was interrupted and the QD layer was annealed in-situ under the presence of

nitrogen flux for various times before the growth of GaN barrier. Fig. 2.9(a) shows the variation of PL intensities and shifts in peak energies for 15, 30 and 45 s interruption

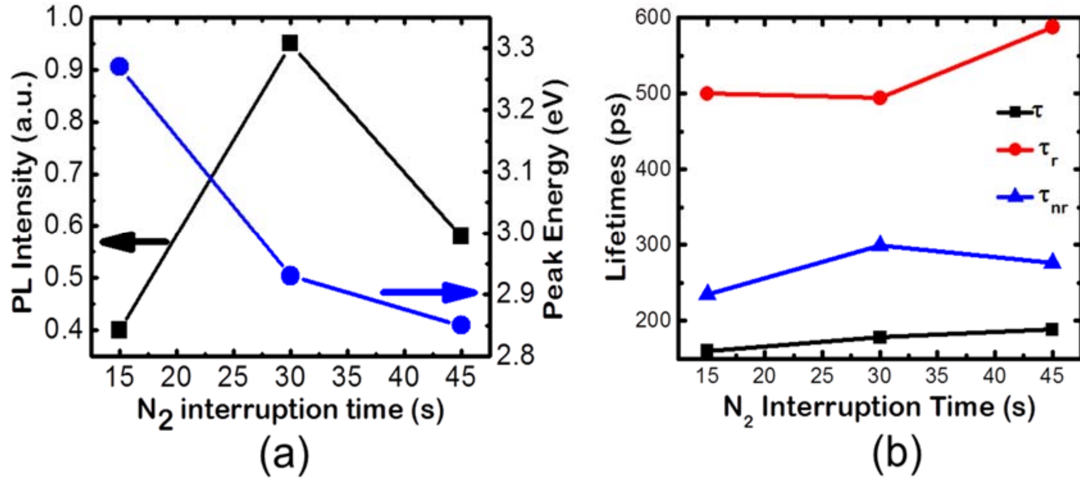

Fig. 2.9. Influence of N_2 interruption times after each layer of InGaN QD formation on its (a) PL intensity and peak energy, and (b) lifetimes.

times. For increase in interruption time from 15-30 s, an increase in dot density was observed due to enhanced adatom surface mobility in presence of nitrogen flux during growth interruption. This causes enhanced PL intensity and reduced radiative carrier lifetimes in well-formed high density QDs (Fig. 2.9(b)). A further increase in interruption time ($t > 30$ s) showed an increase in average dot size and resulting non-uniformity in dot size from AFM measurements. Larger annealing times possibly result in coalescence of smaller dots to form bigger dots due to Ostwald ripening [64]. This explains both the lowering of the PL intensity and an observed increase in carrier lifetimes. Highest PL intensity and lowest carrier lifetime were obtained for in-situ annealing time of 30s as shown in Fig. 2.9. An optimum interruption time after QD layer growth enhances the optical properties of the QD layers significantly. A continual red-shift in peak PL

emission from QD samples is observed with increasing annealing times. This follows from the increasing dot size which causes comparatively larger piezoelectric polarization field in the dots resulting in red-shift in emission.

2.3.3 Optimization of GaN barrier layer thickness

A sufficient GaN spacer layer thickness in between two layers of InGaN QDs is required to relax the tensile strain present in the spacer layer and promote growth of uniform uncoupled QDs. If the barrier thickness is too low, the different QD layers may exhibit significantly different structural, and hence, optical properties. This would cause broadening of PL spectrum and reduced efficiencies. The growth conditions of the GaN barrier layers were calibrated at InGaN QD growth conditions. Quantum dot samples with 7, 12 and 16 nm of GaN barrier thicknesses were grown and characterized. A reduction in the linewidths (full width half maxima (FWHM)) of the room temperature PL spectra from 38 to 31 nm was observed with increasing GaN barrier thickness in the QD samples as shown in Figs. 2.10(a) and (b). PL intensities show a progressive increase with increasing barrier thickness (Fig. 2.10(a)). Reduction of the linewidth and increase in PL intensity is due to the formation of more uniform and smaller uncoupled QDs with increasing barrier thickness which is also indicated by reduction of carrier lifetimes obtained in these samples as seen in Fig. 2.10(b). A blue-shift of peak emission energy with increasing spacer or barrier layer thickness indicates that the dots are less vertically coupled (Fig. 2.10(c)) and thereby, have decreasingly lower FWHMs.

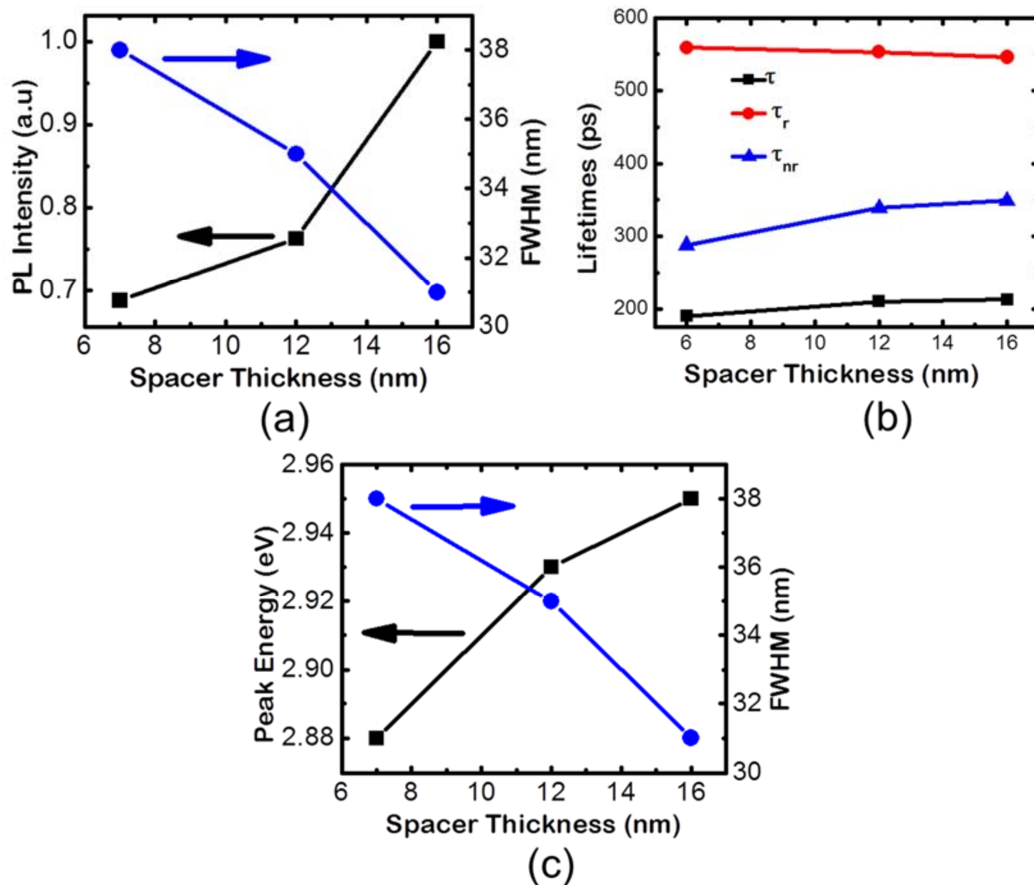

Fig. 2.10. Influence of GaN barrier layer thickness after each layer of InGaN QD formation on its (a) PL intensity and peak energy, and (b) lifetimes.

2.4 Optical Characterization of Optimized Blue and Green InGaN/GaN Quantum Dots

Optimized growth conditions were then used to grow capped eight layers of QDs and their optical properties characterized by performing temperature dependent and time-resolved PL (TRPL) measurements. The radiative efficiency and lifetimes in these dots are limited by the threading dislocation density propagating from the GaN/sapphire

templates. To overcome this limitation, optimal growth conditions were used to obtain InGaN/GaN QDs emitting in the blue and green wavelengths on GaN substrates with dislocation density of 5×10^5 cm^{-2} for these optical measurements. High radiative efficiencies of ~60% for blue emission and ~38% for green emission were obtained as shown later in this section. AFM measurements were carried out on optimized InGaN QDs on GaN/sapphire templates and the size distribution of the QDs were fit with scaling theory to indicating good epitaxial growth conditions during QD formation. Transmission electron microscopy were also performed on such samples. Temperature sensitivity of the QDs with different radiative efficiencies was measured for InGaN/GaN QDs grown on GaN/sapphire to realize the thermal activation of the dots under different growth conditions.

2.4.1 Temperature dependent and time resolved photoluminescence measurements

Temperature dependent photoluminescence (PL) and time-resolved PL (TRPL) measurements were performed on both the blue- and green-emitting samples. For measurement at low temperatures, the samples were cooled using a liquid He closed-loop cryostat and excited by a frequency tripled mode-locked Spectra Physics Tsunami Ti:sapphire laser (λ = 267 nm) with a pulse width of 130 fs and repetition rate of 80 MHz. Sample emission was detected using a spectrometer with 0.03 nm resolution and a photon counter. Fig. 2.11(a) shows a plot of the variation of PL intensity with temperature for blue-emitting InGaN QDs. The blue-emitting $In_{0.18}Ga_{0.82}N$/GaN QD (λ = 420 nm) sample grown on a GaN substrate was found to have a radiative efficiency or internal quantum efficiency of η_i=60%, assuming that non-radiative centers are frozen in the QDs at 20 K. Similar measurements were performed on green-emitting

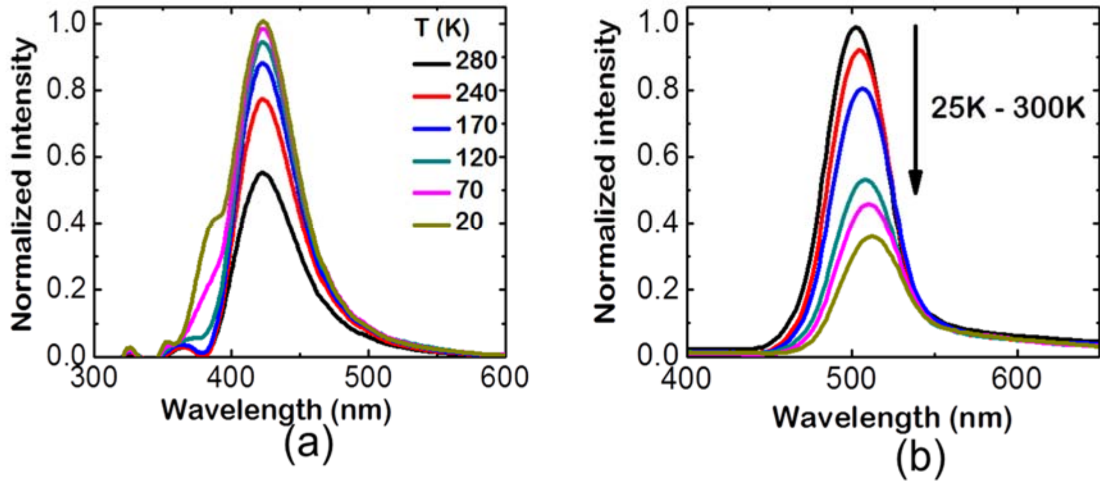

Fig. 2.11. Photoluminescence spectra of (a) blue-emitting and (b) green-emitting eight layers of InGaN/GaN QDs grown on free-standing GaN bulk substrates under different temperatures.

$In_{0.32}Ga_{0.68}N$/GaN QDs (λ = 530 nm) and η_i=38% was obtained as shown in Fig. 2.11(b). As reported in the literature [53, 65], at low temperatures, injected carriers are confined in the localization potential of the quantum dots or in the potentials due to compositional fluctuations. The carriers acquire enough thermal energy with increasing temperature to overcome the potential barriers and recombine at non-radiative traps in the barrier and wetting layer regions. Then the ratio of the saturated peak PL intensity at 30 and 300 K at high excitation powers is an approximate measure of the internal quantum efficiency, η_i (at room temperature). The thermionic emission of carriers and recombination in other layers at elevated temperatures may result in an underestimation of η_i. However, by measuring the dots at high excitation where the dots are saturated with carriers, this effect was minimized. All our temperature dependent and time-resolved PL measurements were carried out at the highest excitation power of ~30 mW with a focused laser spot being ~50 μm diameter.

Luminescence decay times of QD samples were measured using a Hamamatsu streak camera with an overall resolution of ~5 ps. Measured decay times are analyzed with a stretched exponential model to obtain total carrier lifetimes for the QD samples:

$$I = I_0 exp\left[-\left(\frac{t}{\tau}\right)^{\beta}\right] \quad (2.1)$$

where β is the stretching parameter which is calculated to be ~0.95 for both blue and green emitting QD carrier decay times indicating absence of strong polarization field or In composition fluctuations in the InGaN QD region. Most commonly, deviation of β from unity is explained by change in lifetime with carrier depopulation due to carrier screening of piezoelectric field or a degree of compositional fluctuations in the dots as seen in InGaN quantum wells with β~0.5-0.7 [66]. The fitting of the room temperature PL decay time from TRPL measurements for blue QDs are shown in Fig. 2.12. Similar measurements were performed as a function of temperature to obtain total lifetimes as a function of temperature. At room temperature, blue and green QDs were found to have a total lifetime of 276 and 555 ps, respectively. Radiative (τ_r) and non-radiative lifetimes (τ_{nr}) at all temperatures were obtained using equations:

$$\frac{1}{\tau} = \frac{1}{\tau_r} + \frac{1}{\tau_{nr}} \quad (2.2)$$

and

$$\frac{I(T)}{I(20K)} = \frac{1}{1+{\tau_r}/{\tau_{nr}}} \quad (2.3)$$

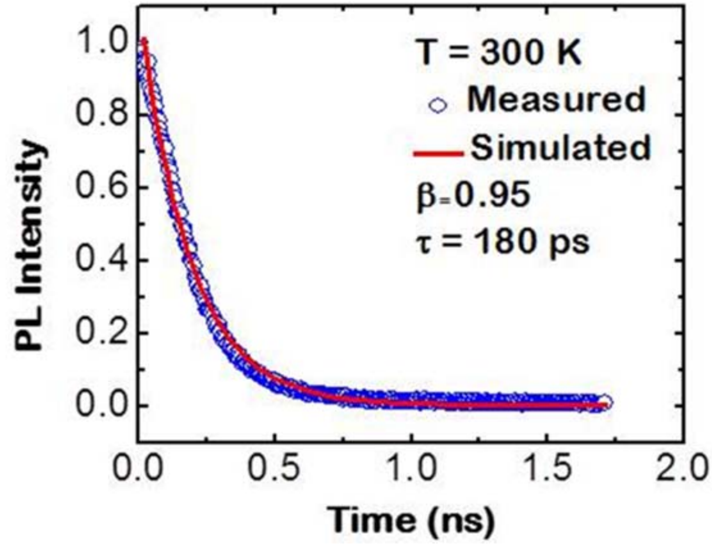

Fig. 2.12. Room temperature carrier decay times obtained from time-resolved PL measurements and fit with stretched exponential model for blue emitting InGaN/GaN QDs.

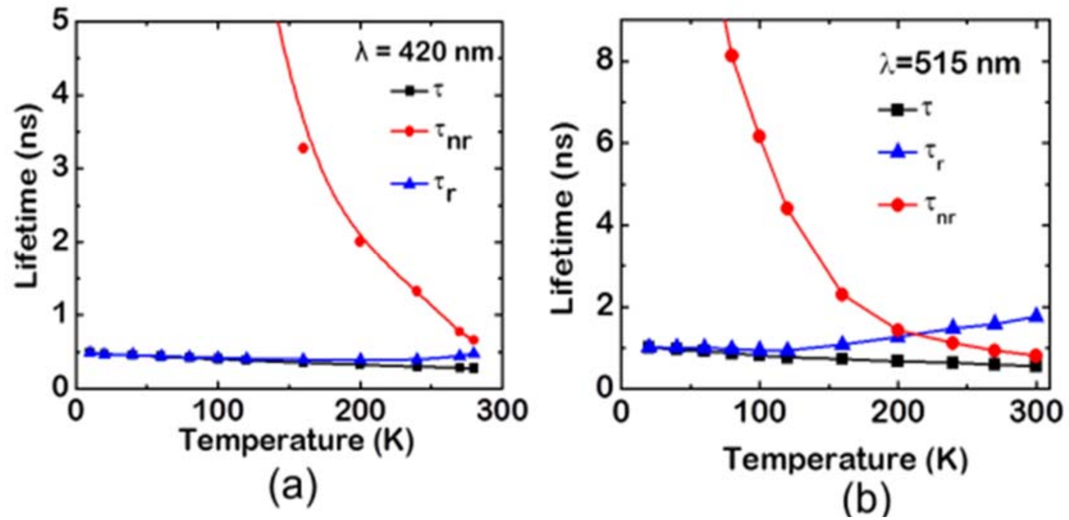

Fig. 2.13. Total, radiative and non-radiative carrier lifetimes obtained from TRPL and time dependent PL measurements for (a) blue and (b) green emitting InGaN/GaN quantum dots.

and are shown in Figs. 2.13(a) and (b). For blue-emitting QDs, τ_r remains nearly constant at 461 ps while for green-emitting QDs, it increases with temperature from ~1ns at low

temperatures to 1.46 ns at room temperature. For both the samples, the radiative and total lifetimes are at least an order of magnitude lower than equivalent quantum wells [67] which match well with theoretical calculations [47] and indicate stronger confinement in QDs resulting in better e-h wavefunction overlap. Non-radiative centers are thermally activated, and as such, non-radiative lifetimes decrease and become comparable to radiative liftimes with increasing temperatures. It should be noted that while for blue dots τ_{nr} is larger than τ_r at room temperature, green dots have lower τ_{nr} as a consequence of a lower η_i. The carrier lifetimes were also measured using a high excitation power of the injection laser where efficiency gets saturated and is independent of In clustering effects or large polarization fields.

2.4.2 Thermal activation energy for InGaN/GaN radiative recombination

Photoluminescence intensities from QD samples are expected to exhibit lower sensitivity to temperature due to their discrete density of states resulting in stronger confinement of carriers preventing their escape to non-radiative centers. This would provide higher efficiencies from QD samples. The ratio of integrated PL intensities at 300 K and 10 K provide an efficiency value of ~44 % for our QD samples grown on GaN/sapphire template. Fig. 2.14 shows the Arrhenius plot of the integrated PL intensity to determine the activation energies associated with QD structures. The solid line is a fit to the measured PL intensities using the formula

$$I = C[1 + Ae^{-\left(E_1/kT\right)} + Be^{-\left(E_2/kT\right)}] \qquad \text{(Equation 2.4)}$$

where I is the integrated PL intensity, and E_1 and E_2 are the two activation energies reflecting the behavior of PL intensity change at two different temperature regimes T >

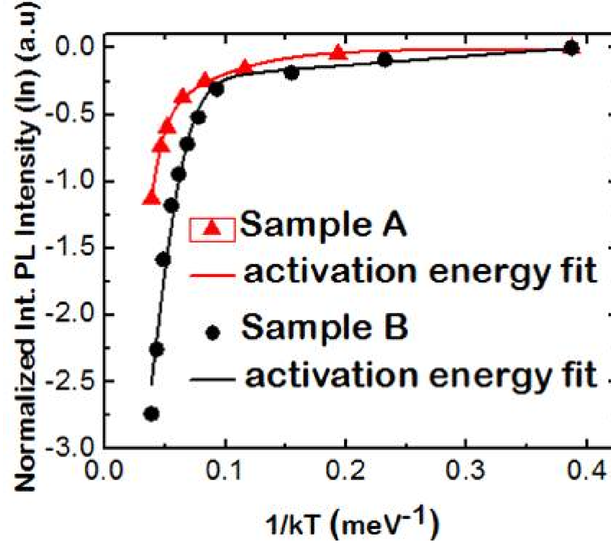

Fig. 2.14. Thermal activation of blue emitting QD photoluminescence grown on GaN/sapphire templates. Sample A: radiative efficiency 44%; Sample B: Radiative efficiency 18%.

200 K and T<100 K. For T<100 K, an activation energy E_1~20 meV was found. At higher temperatures, E_2 ~140 meV was obtained which is significantly higher compared to the values reported for quantum well samples. This activation energy is indicative of the energy required for the carriers to escape confinement from the QDs to undergo non-radiative recombination. The ground state energies of $In_{0.18}Ga_{0.82}N$ QDs have been calculated using a simple band energy calculation for an equivalent QW structure using a finite barrier model and including the spontaneous polarization field. Bhattacharya *et. al.* have shown that $In_{0.27}Ga_{0.73}N$ green QDs have a reduced polarization field of ~ 70kV/cm [49]. Taking into account the calculated $In_{0.18}Ga_{0.82}N$ band-gap of 2.743 eV, an ΔE_C : ΔE_V ~ 60 : 40, and involving heavy-hole ground state calculations, emission energy was calculated to be ~2.85 eV which is close to the PL emission peak of 2.95 eV. The first electron ground state for a QW with a dimension of 4 nm was found to be ~100 meV resulting in a barrier height of ~ 275 meV. However, lower activation energy for the QD

samples (140 meV) compared to their barrier height (~275 meV) indicates that the excitons in the QDs are not completely isolated [40]. There is an efficient coupling between the excited states of the adjacent dots thereby reducing the barrier required for the carriers to escape and undergo non-radiative recombination. This is also responsible for reducing the radiative efficiencies of the QDs.

2.4.3 Temperature dependent photoluminescence shift: absence of S-shaped behavior

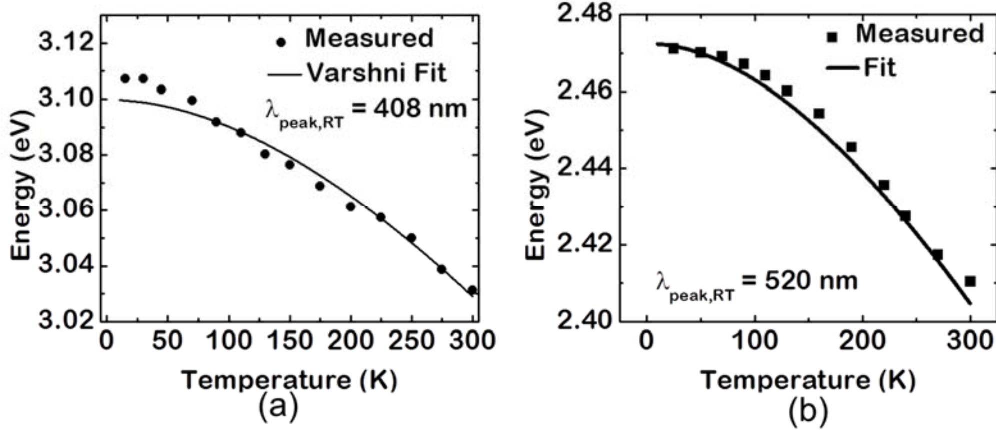

Fig. 2.15. PL peak energy shift with temperature for (a) blue and (b) green emitting InGaN/GaN QDs fit with Varshni equation.

The peak PL emission energies are plotted in Fig. 2.15 for both blue and green emitting InGaN/GaN QDs. Interestingly, and quite contrary to the S-shaped behavior observed in InGaN/GaN quantum wells [68, 69], the peak emission shift with temperatures indicate a close match with Varshni relation [70]. The temperature dependent band-gap shift from the Varshni equation is given by:

$$E_g(T) = E_g(0) - \frac{\alpha T^2}{T+\beta} \quad \text{(Equation 2.5)}$$

where α and β parameters are used for fitting the curve for blue and green InGaN quantum dots measured and shown in Fig. 2.15. The absence of S-shaped behavior for QD PL peak emission energy shift indicates little or no Indium composition fluctuation present in the InGaN/GaN QDs region. It should be noted that the experimental data for the blue QDs (λ=408 nm) does not fit that well with the Varshni fit (Fig. 2.15(a)). This is probably because the blue QDs with very short wavelengths have low In composition and thereby, difficult to form resulting in poor dot formation and a deviation from Varshni relation.

2.5 Structural Characterization of InGaN/GaN Quantum Dots

Atomic force microscopy (AFM) and transmission electron microscopy (TEM) were performed on several samples to better understand the distribution of QD height across the sample, the distribution of In atoms in the QDs and to show that the QDs were grown by elastic relaxation of highly compressively strained InGaN layers on GaN substrates through the formation of a wetting layer as expected from S-K growth mechanism.

2.5.1 Atomic force microscopy (AFM) and scaling theory

The QD height distribution in the uppermost uncapped QD layer was obtained using AFM measurements for optimized blue and green emitting InGaN/GaN QDs. The AFM measurements were done with a Veeco Nanoman AFM facility using tapping mode microscopy. Typical AFM measurements are shown in Fig. 2.16. From Fig. 2.16 (a), the typical QD height and base width for blue InGaN/GaN QDs are ~3 nm and ~30 nm, respectively. The QD height and base width for green emitting InGaN/GaN QDs are ~5

nm and ~45 nm respectively as can be seen in Fig. 2.16(b).

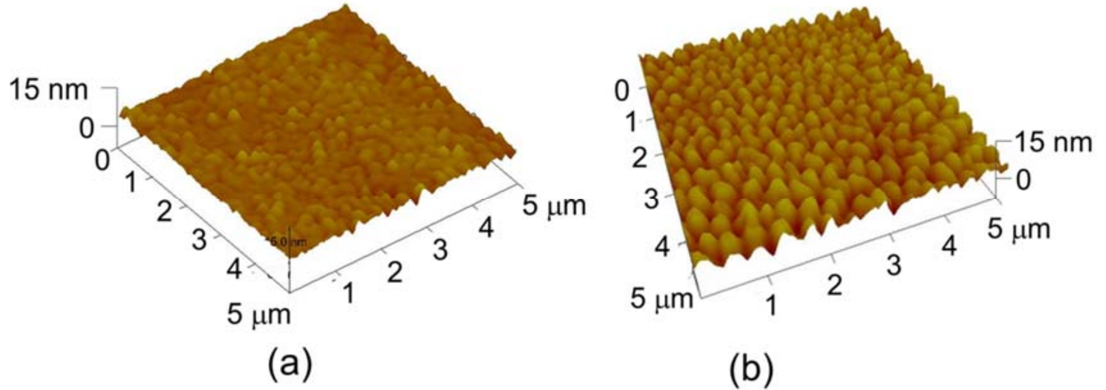

Fig. 2.16. Atomic force microscopy (AFM) measurements of a (a) blue and (b) green emitting InGaN/GaN QDs.

Also, for both sets of QDs, the size distribution of the grown quantum dots follows the scaling distribution, which is given approximately by the form [71]:

$$f_i(u) = C_i u^i e^{-i a_i u^{\frac{1}{a_i}}} \qquad \text{(Equation 2.6)}$$

where C_i and a_i are constants which satisfy the sum rules for $f_i(u)$, i is defined as one less than the critical dot cluster size, and u is the normalized size.

The distribution of quantum dot heights is analyzed for the blue and green dots as shown in Figs. 2.17(a) and (b), respectively. Both the blue and green dot heights fit well with the scaling functions, indicating good epitaxial growth of both sets of quantum dots. The dots are of an average height of <s>~3 nm for the blue dots and an average height of <s>~4 nm for the green dots. The differences in the dot sizes arise from changes in the substrate temperature that the dots were grown at, and from the ratio of gallium to indium flux during the quantum dot growth. The blue and green dots were grown at substrate temperatures of 565°C and 542°C, respectively. Furthermore, the blue dots were grown at

equivalent group III pressures of Φ_{Ga}: Φ_{In} = 2:1 while the green dots were grown at a flux ratio of Φ_{Ga}: Φ_{In} = 3:2. The temperature and pressure differences give rise to an increase in 'i' parameter from i=3 in the blue dots to i=5 in the green dots, indicating critical cluster sizes of 4 atoms and 6 atoms, respectively [71]. As expected, the green quantum dots are larger than the blue dots. Additionally, from the normalized distributions, it is evident that the larger green dots are more uniform in size.

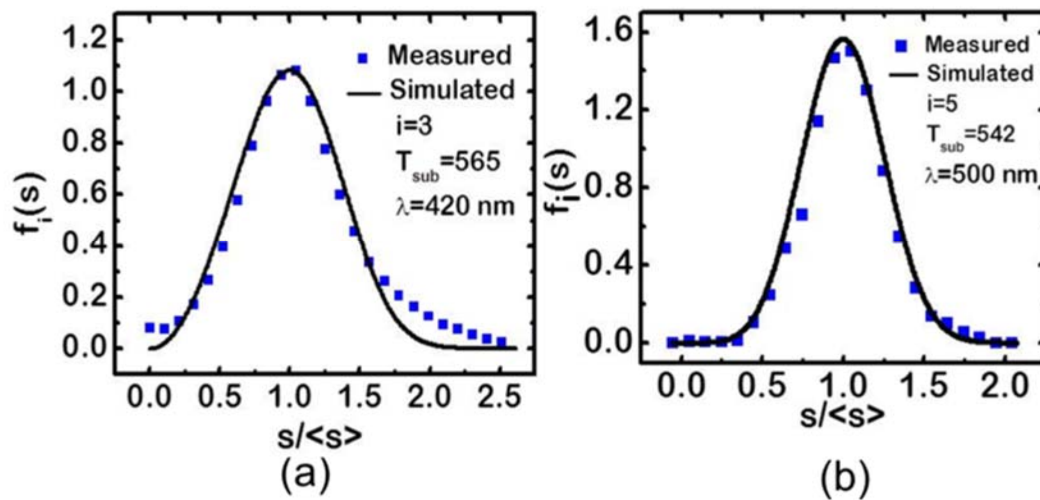

Fig. 2.17. QD height distribution of (a) blue and (b) green emitting InGaN/GaN QDs obtained from AFM measurements and fit with scaling theory showing good epitaxial growth of dots.

2.5.2 Transmission electron microscopy of InGaN/GaN quantum dots

Transmission electron microscopy (TEM) measurements were performed on green emitting InGaN/GaN QDs grown on GaN substrates for ease of sample preparation. Two pieces of the QD heterostructures were bonded together with MBond 600 to protect the QD surface and was mechanically thinned to ~50 μm. The sample was put onto a carbon coated transmission electron microscopy (TEM) grid and further polished to ~500nm

using ion beam milling with Ga ions. The cross-sectional QD heterostructure was imaged using a JEOL 2100F high resolution scanning TEM. Fig. 2.18(a) shows seven pairs of InGaN QDs indicating no evidence of basal plane dislocations. While the first layer is relatively smooth, some degree of interface roughening and faceting are observed in subsequent layers. The propagation of a dislocation originating from the substrate

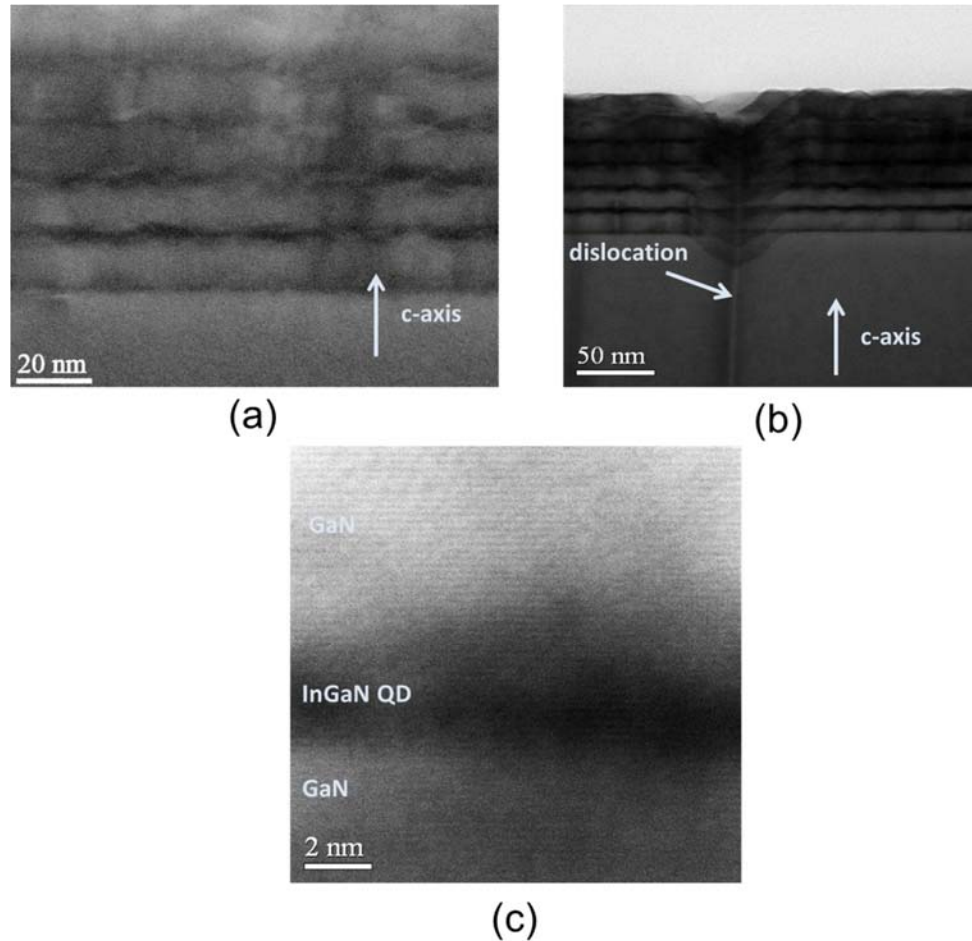

Fig. 2.18. (a)Transmission electron microscope (TEM) image of seven layers of red--emitting InGaN/GaN QDs, (b) bright field TEM indicating how dislocations can propagate through the dots, and (c) high resolution TEM of a single QD.

underneath is seen in the bright field TEM image shown in Fig. 2.18(b). A high resolution TEM of a single InGaN QD shows relatively uniform In composition in the

dots with no In clustering.

2.6 Summary

The role of the active region in optical devices predominantly determines the performances of the devices. InGaN/GaN quantum dots were optimized by changing various growth parameters and optically characterizing such variations to draw correlations which can be repeated for different wavelengths in MBE growth to achieve high radiative efficiency QDs. Other optical and structural characterizations were performed on such QDs, and especially the ones performed on optimized QDs indicated a close to single exponential carrier decay times, low radiative lifetimes (~1.5ns for green QDs), high radiative efficiency (~40% for green QDs), absence of S-shaped behavior in PL peak emission shift, excellent match to scaling theory and crystallinity of the structures from TEM measurements. The optimized QDs were incorporated in device heterostructures and their performances characterized as discussed in subsequent chapters.

Chapter III

InGaN/GaN Quantum Dot Light Emitting Diodes

3.1 Introduction

There has been a vsat amount of research and development into nitride-based light emitting diodes (LEDs) due to their applications in solid state lighting. As discussed in chapter 1, there are numerous challenges facing current state-of-the-art commercial InGaN/GaN quantum well (QW) LEDs including low peak efficiencies, "efficiency droop" at high injections and large peak emission shift due to quantum confined Stark effect (QCSE) [72]. The "efficiency droop" has been mostly attributed to Auger recombination [16, 22] and carrier leakage from quantum wells [17], enhanced by the large polarization field in the quantum wells especially for large In composition for green emission. This polarization field is also responsible for reduced electron-hole wavefunction overlap resulting in poor peak efficiencies. Additionally, the screening of the polarization field with increasing injection results in a strong QCSE and consequently, a large blueshift in the peak emission wavelength (~20-30 nm) [72] in QW LEDs.

The advantages of using quantum dots (QDs) in the active region, over quantum wells, arise from the reduction of the polarization field in the dot layers due to the strain relaxation during the QD formation (by the S-K growth mode) and spatial confinement of

carriers in the dots as discussed in detail in chapter II. The InGaN/GaN quantum dots emitting in both blue and green wavelengths were characterized by nearly mono-exponential carrier decay times, low radiative carrier lifetimes resulting in high radiative efficiencies, absence of "S-shaped" behavior in temperature dependent peak emission shift indicating no In clustering and structural uniformity of the QDs as also seen from atomic force microscopy (AFM) and transmission electron microscopy (TEM) imaging in the previous chapter. This chapter discusses the growth and process optimization of LEDs incorporating the optimized blue- and green-emitting InGaN/GaN QDs in the active region. The performance of these devices are characterized by current-voltage (I-V), light output-current (L-I), and efficiency measurements. Additionally, high speed QD LEDs and state-of-the-art QW LEDs are fabricated and characterized by differential carrier lifetime measurements to understand the recombination dynamics of carriers in different LED heterostructures under various injection levels.

3.2 Growth of InGaN/GaN Quantum Dot Light Emitting Diode Heterostructure

Heterostructures for blue- and green-emitting InGaN/GaN quantum dot (QD) light emitting diodes (LEDs) were grown in Veeco Gen II and Gen 930 plasma-assisted molecular beam epitaxy (MBE) system. The QD LED heterostructures were grown on n-GaN/sapphire template and one such typical heterostructure schematic is shown in Fig. 3.1. As outlined in section 2.2, after cleaning the n-GaN/sapphire templates and degassing in two steps, 300 nm of Si-doped GaN (n ~ 5×10^{18} cm^{-3}) was grown at a nitrogen flux fixed at 0.5 sccm with a rf power of 300 W and a Ga flux Φ_{Ga} = 4.5

nm/min. During the growth of the n-GaN layer, substrate temperature was maintained at T_{sub} = 740 ^{0}C calibrated with a pyrometer for Si (7x7) to (1x1) transition. Growth was initiated only after the background chamber pressure stabilized following the striking of plasma. The RHEED pattern remained bright and streaky through the growth of this layer. This was followed by an increase of N_2 plasma flow rate and power to 0.7 sccm and 380 W, respectively before the growth of InGaN/GaN self-assmbled QDs which

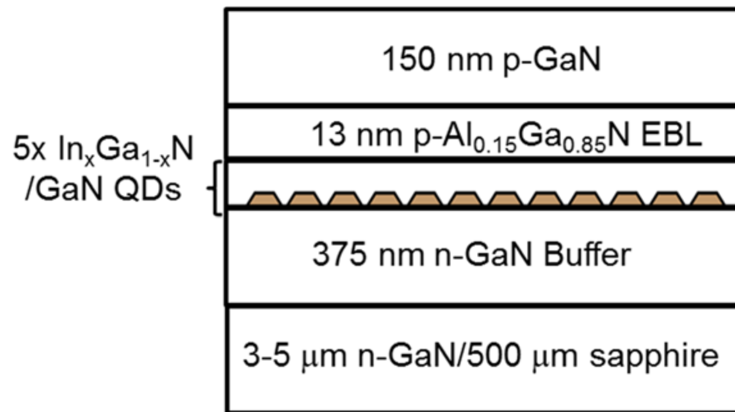

Fig. 3.1. Schematic of InGaN/GaN quantum dot LED heterostructure grown on GaN-templated c-plane sapphire substrates.

form under N_2-rich conditions. Five pairs of the optimized InGaN/GaN QDs, as reported in chapter 2, were then used to form the active region. The QD growth conditions were changed by varying the composition of the dots by varying the In:Ga fluxes and substrate temperatures to obtain emission across various wavelengths. Typically, blue emitting QDs are grown at ~T_{sub}=565 ^{o}C and Φ_{In}: Φ_{Ga} = 2:1. Longer wavelength green emissions are generally obtained by lowering the growth temperatures to ~T_{sub}=545 ^{o}C and by increasing In flux to Φ_{In}: Φ_{Ga} = 3:2. Other growth parameters including III/V ratio, number of MLs required to form the QDs, N_2 interruption times, and GaN spacer layer thicknesses were optimized to get strong optical emissions.

Five layers of capped InGaN/GaN QDs were followed by stabilization of the plasma back at 0.5 sccm and 300 W for growth of successive layers. A thin 5 nm layer of GaN layer was grown at T_{sub}=740 ^{o}C which further aids in recreating a smooth surface morphology and an accompanied streaky RHEED pattern before the growth of p-doped layers. A heavily Mg-doped (p ~8x10^{17} cm^{-3}) $Al_{0.15}Ga_{0.85}N$ 13 nm electron blocking layer (EBL) was grown at T_{sub}=740 ^{o}C to improve LED performance by preventing electron leakage at high injections [73]. The Al composition, AlGaN thickness and the growth temperature were optimized to obtain lower turn-on and series resistance in the devices, as will be shown later. AlGaN growth conditions are reported to be of a better crystalline and electrical quality when grown at high temperatures [74] as Al has a very high sticking coefficient and a lower growth temperature creates a bad surface morphology due to excess Al incorporation in the layer. The AlGaN layer was grown at T_{sub}=770 ^{o}C in the MBE with Φ_{Al}: Φ_{Ga} = 1:6 with the corresponding AFM image, photoluminescence (PL) and X-ray diffraction (XRD) data shown in Fig. 3.2. As seen from the figure, clear XRD peaks corresponding to the AlGaN and GaN epilayers were observed from the XRD measurement. The room temperature PL of the AlGaN calibrating layer showed a strong band edge emission (Fig. 3.2(b)) indicating absence of any optically active defects present in the material. The surface morphology was slightly spotty (Fig. 3.2(c)) which resulted from the large thickness (150 nm) of the highly strained AlGaN layer grown. This is not of concern in the LEDs as a thickness of only 15 nm AlGaN is required for the EBL and the surface morphology remained very smooth for $Al_{0.15}Ga_{0.85}N$ layers with such small thicknesses as observed from RHEED.

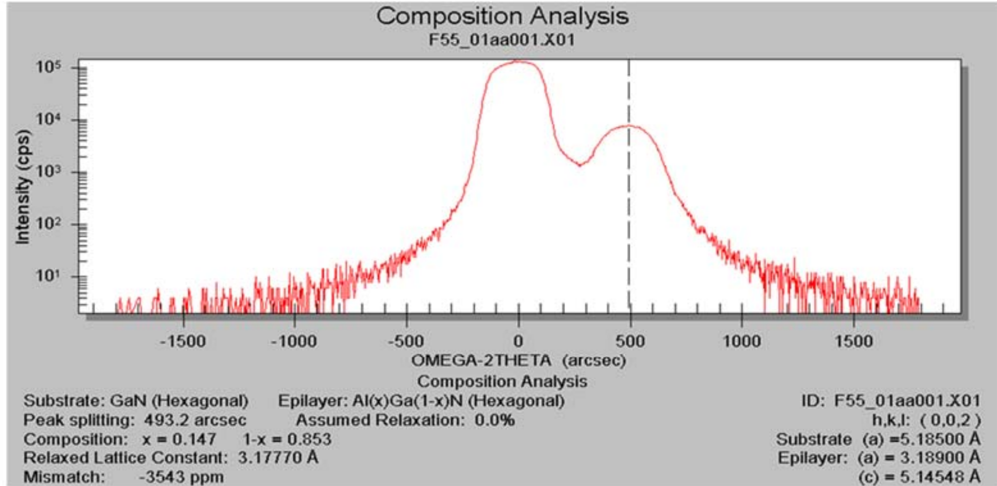

(a)

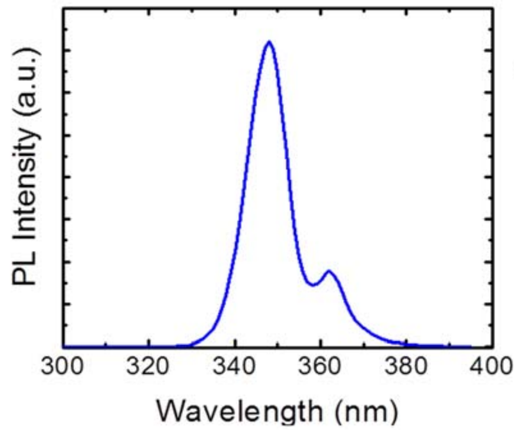

(b)

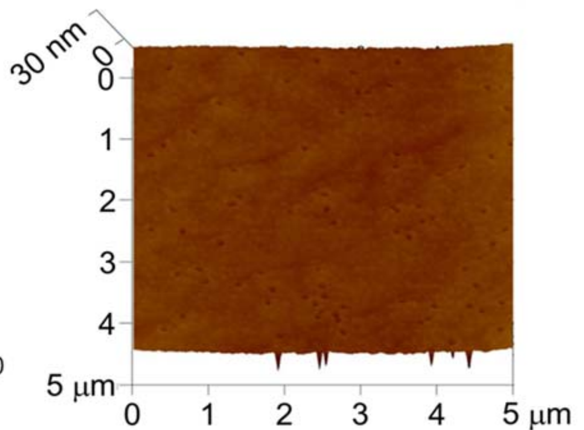

(c)

Fig. 3.2(a) X-ray diffraction (XRD) showing composition of AlGaN, (b) room temperature photoluminescence showing AlGaN and GaN band-edge emissions, and (c) a 5µm x 5 µm atomic force microscopy (AFM) image of 150 nm $Al_{0.15}Ga_{0.85}N$ layer on GaN/sapphire template for electron blocking layer.

The final Mg-doped p-GaN layer was grown 150 nm thick followed by a 5 nm thick p^+-GaN region for improved ohmic contact formation. As discussed in chapter 1, growth of p-doped GaN layers by metal organic chemical vapor deposition (MOCVD) was finally achieved after lengthy research by post-thermal annealing method [31] to get rid of the Mg-H complex formed. However, the doping efficiency of the Mg atoms was still substantially low (~1-3%) as they have high activation energy of ~170 meV. The

possibility of Mg-doped p-GaN growth at lower T_{sub}=710 ^{o} and absence of hydrogen in a high vacuum MBE chamber has created better p-doping in MBE-grown layers. For sufficient Mg incorporation, the layers had to be grown under Ga-rich (Φ_{Ga}=5nm/min) conditions to maintain continuously smooth surface morphologies during heavy Mg incorporation which can easily roughen the surface in the absence of a metallic bilayer during growth [75]. The p-doping levels for such growth conditions were measured to be ~$8x10^{17}$ cm^{-3} from Hall measurements. Small proportion of In ($In_{0.01}GaN$) was also introduced during the p-GaN growth which acts as a surfactant preventing the roughening of the surface morphology.

3.3 Fabrication and Characterization of Quantum Dot LEDs

3.3.1 Fabrication of a typical LED

A typical fabricated LED heterostructure schematic is shown in Fig. 3.3(a). Figure 3.3(b) shows a micrograph of a fabricated LED. Contact photolithography (MJB 3 aligner) was used to make all the patterns of the LED structure. The first step involved making a p-contact mesa for current injection. A 300 μm x 300 μm mesa pattern was first created by etching out the remaining p-GaN and active region upto n-GaN. Generally, after calibrating the etch rates in reactive ion etch tool (LAM 9400), 350 nm of heterostructure thickness was etched out. Care was taken to clean the residue after the RIE etching using O_2 plasma in a plasma asher. The second step involved metallization for the p-contacts. A thin layer of native gallium oxide can prevent good ohmic contact formation. After developing a 280 μm x 280 μm opening on top of the mesa, the native oxide was removed by dipping the sample in $HCl:H_2O$ (1:1) for 10 minutes before

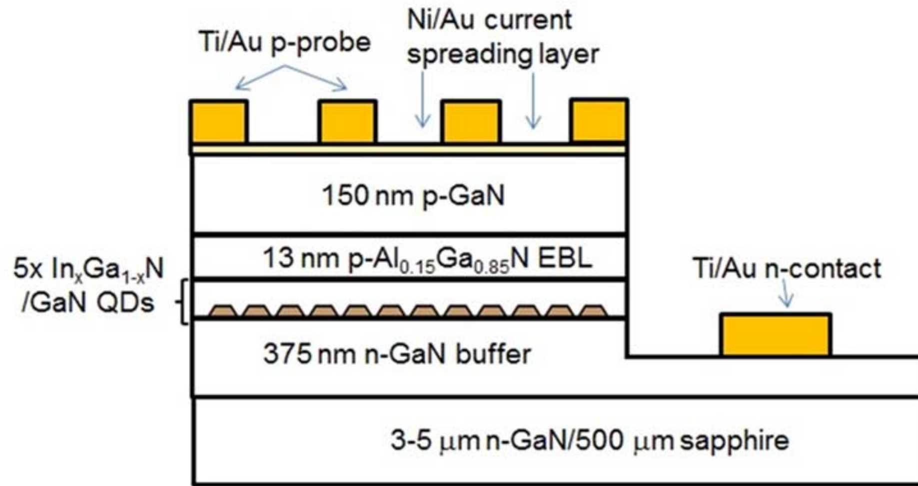

Fig. 3.3(a) Schematic of a fabricated QD LED heterostructure and (b) photo micrograph of fabricated LEDs from top.

quickly loading it into an e-Beam evaporator chamber. A thin 5 nm Ni/ 5 nm Au current spreading layer was selectively deposited using metal lift-off. This was followed by annealing of the p-contacts at 550 ^{o}C for 5 min in a N_2/O_2 1:1 environment in a rapid thermal annealing (RTA) tool to create a Ni-O layer at the interface providing good ohmic contacts to p-GaN. The final step in the LED fabrication involved depositing a thick 25 nm Ti/ 300 nm Au metal serving as an n-contact around the mesa and as a p-contact probe on top of the current spreading thin layer as shown in Fig. 3.3(b).

3.3.2 Fabrication of High Speed LEDs

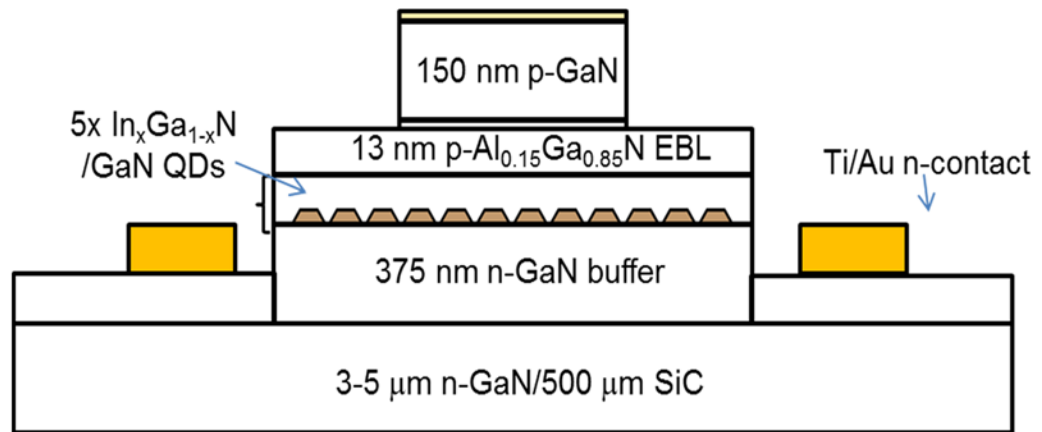

(a)

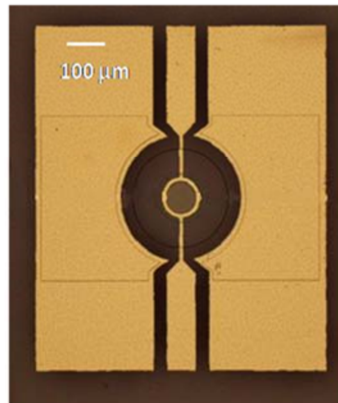

(b)

Fig. 3.4(a) Schematic and (b) micrograph of a fabricated high-speed QD LED heterostructure for measurement using G-S-G probe.

High speed LEDs were fabricated to measure the differential carrier lifetimes in QD and QW based LEDs and to help understand carrier dynamics under various injection levels. Details about differential carrier lifetime measurements are presented in the next section. Figure 3.4 shows (a) a schematic and (b) a photo micrograph of a fabricated high speed

device. High-speed LEDs were fabricated by projection lithography [GSA Auto Stepper] techniques. For realization of high speed LEDs and accurate measurement of differential lifetimes, a current confining aperture with a diameter 114 µm was patterned by inductively coupled plasma etching down to the $Al_{0.15}Ga_{0.85}N$ electron blocking layer. Five nm/ 5 nm of Ni/ Au was deposited on top of this current confining aperture followed by 5 min annealing in a N_2/ O_2 environment at 550º C to form transparent ohmic contact to p-GaN as discussed in previous section. A second mesa with a diameter 228 µm was realized by etching down to the n-GaN layer to facilitate the deposition of the n-ohmic contact for the LEDs. This restricts the current flow path to the 114 µm mesa and prevents carriers from flowing through the rough sidewalls of the active region caused by plasma dry etching. The current confining aperture, thereby, helps in reducing the capacitance [76] and carrier leakage affecting the IQE of the device. SiO_x passivation and subsequent interconnect metal deposition ensures that the p- and n-ohmic contacts are at the same height and can be probed by a high speed ground-source-ground (G-S-G) probe for measurements.

3.4 Output Characteristics of Quantum Dot LEDs

3.4.1 Current-voltage characteristics

The grown and fabricated QD LEDs were characterized for their output characteristics. The current-voltage (I-V) characteristics were plotted for QD LEDs with optimized growth and fabrication conditions and are shown in Fig. 3.5(a). A clear improvement in terms of reduced turn-on voltage and lower series resistance was observed with improved growth conditions in the EBL as described in Table 3.1. The

thickness, Al composition x, and the growth temperature T_{sub} were varied in the $Al_xGa_{1-x}N$ EBL to obtain device performance with lowest turn-on voltage and smallest series resistance. The EBL was designed to prevent the leakage of electrons at higher injections so that they are mostly confined in the active region QDs and undergo radiative recombination. However, due to the strong polarization field and associated band bending, EBL can act as barrier to uniform hole injection in the LEDs [33]. This can be avoided by having strong p-doping in the EBL and designing an optimum thickness and Al composition for the AlGaN EBL. A very low turn-on voltage of ~ 3.5V and series resistance < 10Ω is obtained for a 13 nm $Al_{0.15}Ga_{0.85}N$ EBL. In a typical device of size $7.8x10^{-4}$ cm^2, a current of 100 mA can be supplied at <6.5V to obtain bright emission as shown in Figs. 3.5(b) and (c) for blue and green QD LEDs, respectively.

Device name	AlGaN thickness (nm)	Al composition	Growth temperature T_{sub} (°C)	Turn-on voltage V_{on} (V)	Diode series resistance R (Ω)
LED I	18	0.17	770	10	High
LED II	13	0.15	753	3.3	12
LED III	12	0.17	753	4.5	14
LED IV	13	0.15	770	3.8	12

Table 3.1. Description of the samples used to optimize the EBL layer for lowest turn-on voltage and series resistance.

3.4.2 Electroluminescence of quantum dot LED

The optimized QD LED output was collected by a broad area optical fiber and fed to an Ocean-Optics 2000+ spectrometer calibrated for measuring visible wavelengths. The emitting blue and green QD LEDs are shown in Figs. 3.5(b) and (c), respectively.

The electroluminescence (EL) spectra of the blue and green QD LEDs at 100 A/cm^2 are

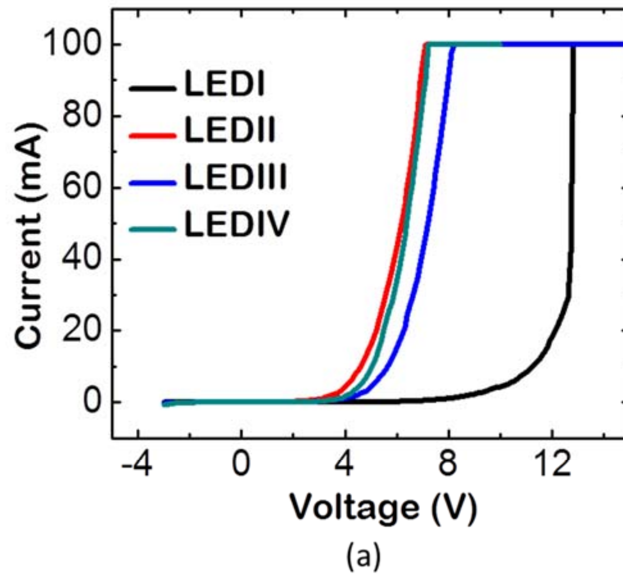

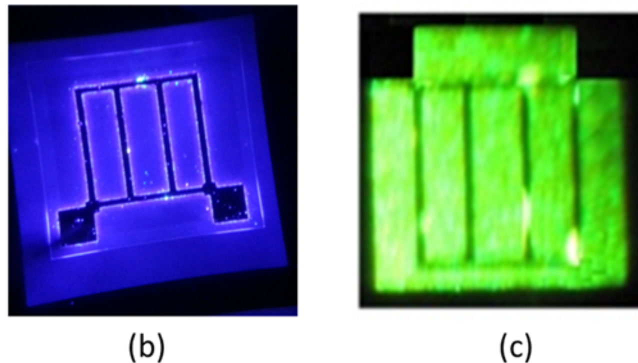

Fig. 3.5(a) Current-voltage characteristics for different EBL layers in QD blue LEDs. Micrographs of (b) blue and (c) green QD LEDs under 100 A/cm^2 injection.

plotted in Figs. 3.6(a) and (b), respectively. The spectra of the blue and green QD LEDs were measured as a function of injection current and the peak emission shift is plotted in the inset to the respective figures. A peak shift of only 3.8 nm corresponds to a built-in polarization field of ~70 kV/cm. Similar measurements for green QD LEDs yield an emission shift of 5.7 nm corresponding to a polarization field of 95 kV/cm [49]. The polarization fields calculated from the injection dependent EL shift in QD LEDs are

significantly smaller in comparison with those measured in QW LEDs grown on c-plane GaN [77, 78]. It should also be noted that the EL emission has a single peak of emission indicating uniformity of the active region under uniform injection of carriers.

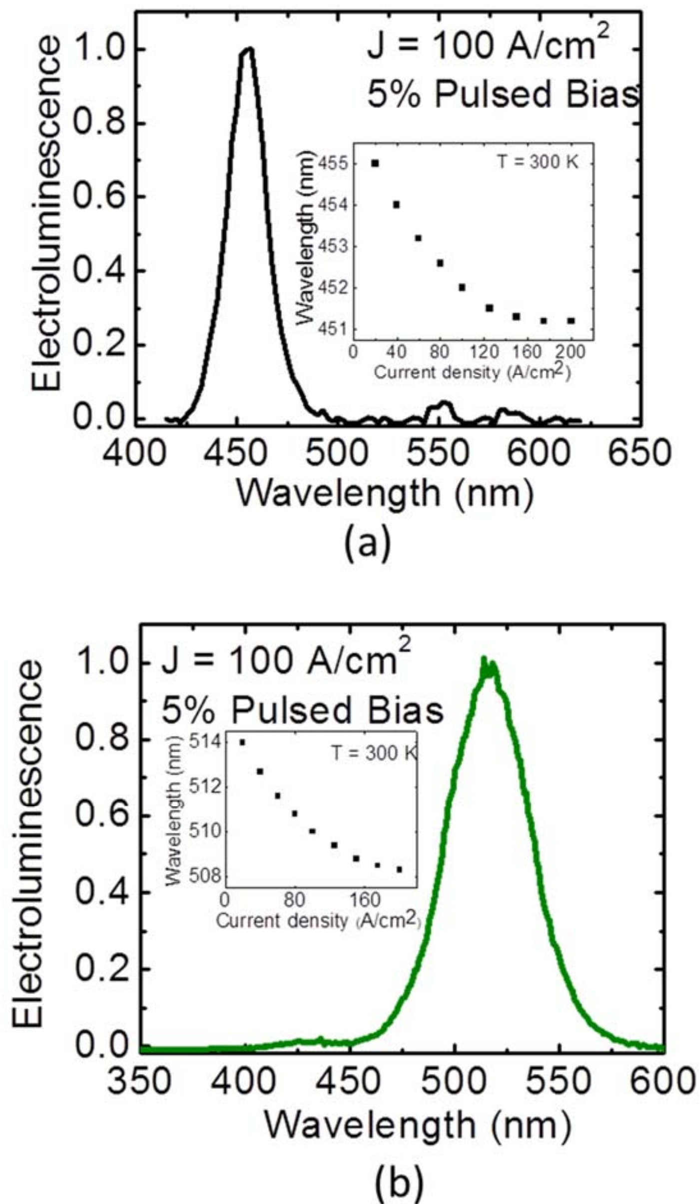

Fig. 3.6. Electroluminescence of (a) blue and (b) green QD LEDs. The injection dependent peak emission shift is shown in the inset for the respective LEDs.

3.4.3 Efficiency characteristics of quantum dot LEDs

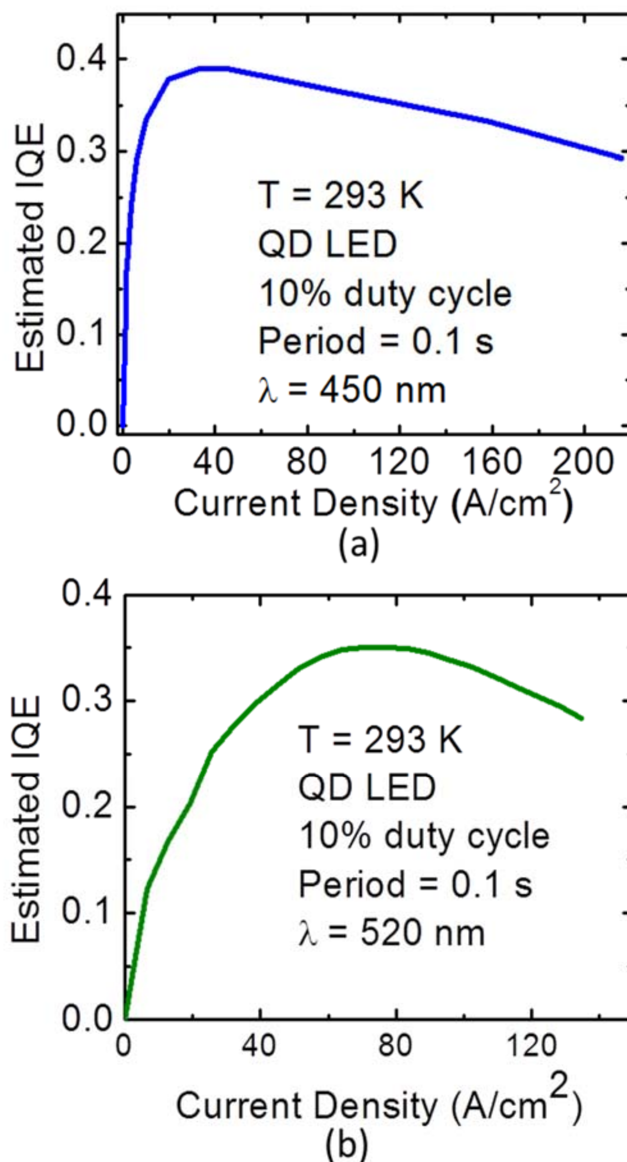

Fig. 3.7. Efficiency characteristics indicating low efficiency droop and peaking of efficiencies at low current densities for (a) blue- and (b) green-emitting QD LEDs.

The light output intensity as a function of injected current (L-I) from blue and green QD LEDs were measured by a Si-Ge detector. The L-I characteristics were used to

obtain relative efficiency as a function of current by dividing the light output by current to obtain the efficiency. The efficiency curves for blue and green QD LEDs are plotted in Figs. 3.7(a) and (b), respectively. The efficiencies peak at much lower current densities compared to the devices made earlier. The y-axis on the plots is adjusted to reflect the radiative efficiencies or internal quantum efficiencies measured on equivalent QDs from temperature dependent PL measurements. The blue QD LEDs have a peak efficiency at 30 A/cm^2 and an efficiency droop of 22%, while the green QD LEDs have efficiencies peaking at 35 A/cm^2 with a measured droop of only 25% when measured between 35 A/cm^2 and 150 A/cm^2. As stated earlier in chapter I and the introduction to this chapter, the efficiency droop is a major problem facing commercial QW LEDs and has been attributed largely to Auger recombination and electron leakage [16, 17, 22], aided by a large polarization field present in the active region. The use of QDs in the active region helps in having reduced polarization field, thereby lowering leakage of electrons and reducing non-radiative Auger recombination at high carrier injections. This helps in attaining lower droop observed in these LEDs without any additional design variations. Additionally, differential carrier lifetime measurements were performed on the high speed QD LEDs and the results compared to QW LEDs. It is a wonderful technique to understand the various recombination mechanisms dominating the carrier dynamics at various injection levels. The processing of the devices have been detailed in section 3.2.2 and the fabricated device heterostructure and micrograph shown in Fig. 3.4. The following section details the measurement and the analysis of the results obtained.

3.5 Differential Carrier Lifetime Measurements of Quantum Dot and Quantum Well LEDs

3.5.1 Introduction

Efficiency droop limits the practical application of current nitride based visible LEDs and is a subject of intense research. The efficiency droop, which typically occurs at a maximum current densities of ~40 A/cm^2 for state-of-the-art c-plane QW LEDs emitting at 415 nm and at ~10 A/cm^2 for 445 nm [79, 80], has been widely attributed to Auger recombination [16, 22], carrier delocalization [79, 81] and carrier leakage from the quantum well active region [17]. The performance characteristics of green InGaN/GaN quantum dot (QD) LEDs had been recently reported by our group [49, 82]. The onset of droop in these devices occurs at higher current densities (~ 220 A/cm^2) and the percentage droop was lower compared to QW LEDs. The advantages of using QDs in the active region of LEDs are reduced polarization field, lower density of structural defects and stronger e-h wave function overlap [47-49]. Differential carrier lifetime measurements [80, 83] on high-speed blue-emitting QD LEDs were carried out and the measured data analyzed and compared to those of blue QW LEDs. Analysis of the measured data helped understand and elucidate the important radiative and non-radiative processes and efficiency characteristics in the two kinds of LEDs. The Auger recombination coefficient in the quantum dots is calculated to be C_0= 2.1x10^{-31} cm^{6}s^{-1}, which is an order of magnitude smaller than the value of the coefficient in the quantum wells. There is also an evidence of a carrier capture bottleneck in the quantum dots, possibly arising from the presence of a wetting layer.

3.5.2 Heterostructure design and measurement

The quantum dot LED heterostructure was grown by MBE containing 5 periods of $In_{0.18}Ga_{0.82}N/GaN$ quantum dots and a 13 nm p-doped $Al_{0.15}Ga_{0.85}N$ blocking layer similar to a typical LED heterostructure mentioned in section 3.1 and 3.3 before and also shown in Fig. 3.4. It should be noted that the LED heterostructure was grown on c-plane GaN-on-SiC substrate for this particular experiment. GaN-on-SiC has lower lattice mismatch of only 3.4% compared to a lattice mismatch of 13.8% for GaN-on-Sapphire. This results in the GaN-on-SiC having a lower density of dislocations ~5-8x10^8 cm^{-2}. The details of the growth are the same as those on GaN-on-Sapphire as mentioned in Chapter 2 and previous sections of chapter 3. Device heterostructures for QW LEDs were grown by metal-organic chemical vapor deposition (MOCVD) on c-plane SiC substrate with the multi-quantum well (MQW) active region consisting of five $In_{0.21}Ga_{0.79}N$ (2.32 nm)/GaN (20 nm) wells. The peak of the measured photoluminescence spectrum for this heterostructure occurs at 450 nm. High-speed LEDs were fabricated by conventional dry etching, metallization and lithography techniques and mentioned in section 3.2.3 in details. SiO_x passivation and subsequent interconnect metal deposition ensures that the p- and n-ohmic contacts can be probed by a high speed ground-signal-ground (G-S-G) probe for measurements.

Room-temperature current-voltage (I-V) and light-current (L-I) characteristics of the high speed QD LED are shown in Fig. 3.8(a). Electroluminescence (EL) measurements made on a QD LED at 98 A/cm^2 show a strong blue emission at 420 nm as shown in the inset to Fig. 3.8(a). The variation of external quantum efficiency (η_{ext}) with

injected current density was obtained from the slope of the L-I curve and is plotted in

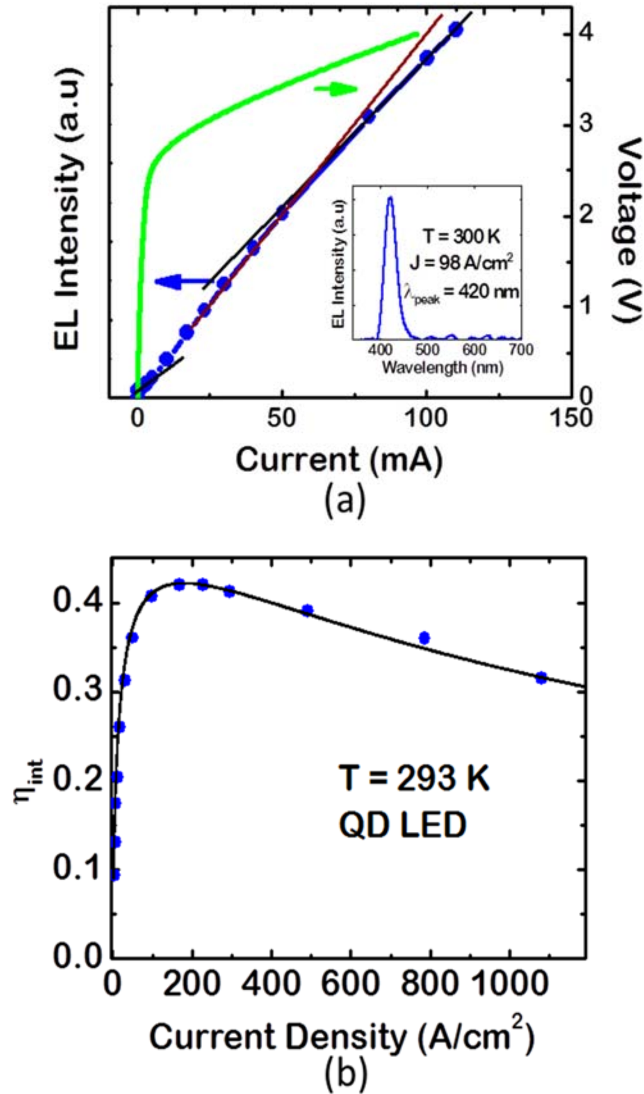

Fig. 3.8(a) Measured current-voltage and light-current characteristics at T = 300K for quantum dot LED. Inset shows electroluminescence spectrum at 300 K, (b) measured internal quantum efficiency of quantum dot LED. The solid curve indicates a fit to the data using the A-B-C model.

Fig. 3.8(b). The peak internal quantum efficiency ($\eta_{int,peak}$) was obtained from temperature dependent photoluminescence measurements at different optical excitation powers and the ratio $\eta_{ext,peak}/\eta_{int,peak}$ is multiplied by η_{ext} to obtain an estimate of the variation of η_{int} with current density, assuming that the extraction efficiency is

independent of current density. From the plot, it may be noted that the IQE of the QD LED peaks at a large current density of ~168 A/cm^2 and then decreases at a slow rate with increasing current, similar to previous observations [49].

For differential carrier lifetime measurements, the LEDs were operated under varying current bias superimposed with a small AC signal (V_{max} = 250 mV) using a high speed G-S-G probe. The phase delay between the light output and the input electrical signal was used to obtain differential lifetimes, τ, and this data was analyzed to obtain the evolution of radiative and non-radiative lifetimes with injected carrier densities in the active region. The measurements were repeated for various frequencies to reduce the measurement noise.

3.5.3 Results and discussion

The measured differential lifetimes for QW and QD LEDs are plotted against current density J in Figs. 3.9(a) and (b), respectively. It should be noted that τ is smaller by an order of magnitude in the QD LED over the entire range of carrier injection, compared to those in the QW LED, as predicted from theoretical calculations [47]. The total recombination rate R is obtained from the injected current density J and active region thickness d by the relation R=J/(qd). The active region thickness in the QW LED is the sum of the width of the 5 quantum wells. For QD LEDs, it is calculated by taking into account the fill factor (82%) given by a dot density of ~8x10^{10} cm^{-2} and an effective base diameter of ~36 nm obtained from an atomic force microscopy (AFM) image of uncapped InGaN/ GaN quantum dots, after accounting for some overlap between the dots. The carrier density undergoing recombination in the active region at a particular injection level is derived from the differential lifetime measurements by the relation $n =$

$\int_0^G \tau dR$. The number of carriers that overflow through the active region, or escape

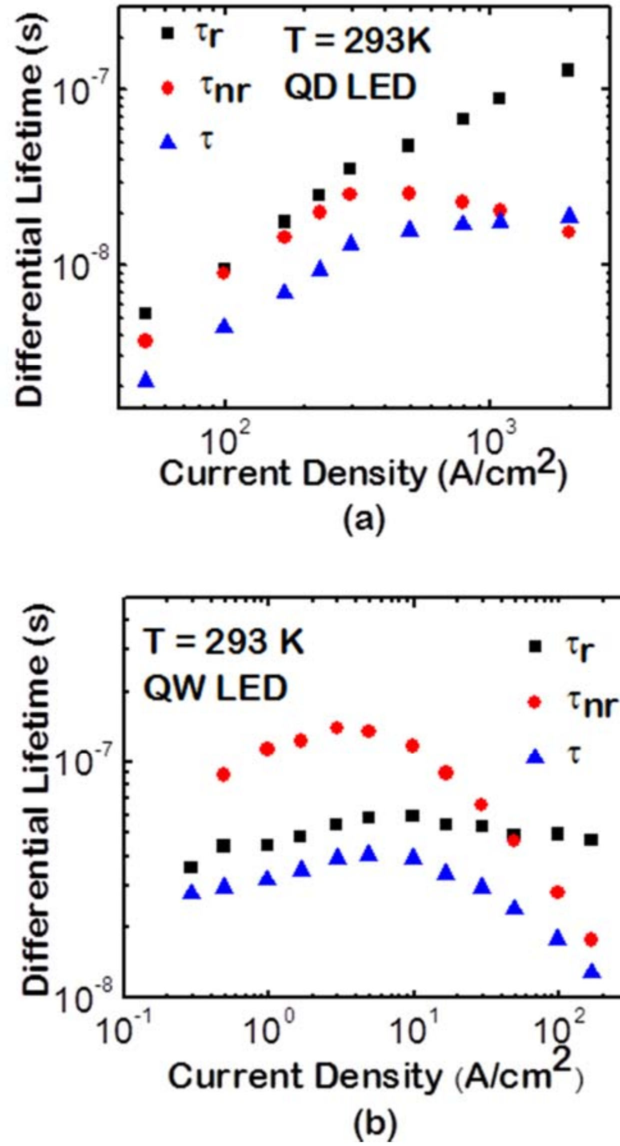

Fig. 3.9. Measured differential lifetime τ and calculated radiative and non-radiative lifetimes, τ_r and τ_{nr}, respectively, as a function of injection current density in (a) quantum dot LED, and (b) quantum well LED.

from the wells/dots without suffering recombination were not taken into account in this analysis. The calculation flow is depicted in Fig. 3.10. The radiative and non-radiative lifetimes as function of carrier (current) density are determined from the measured

variation of τ and η_{int}, taking into account the dynamic change of the lifetimes with

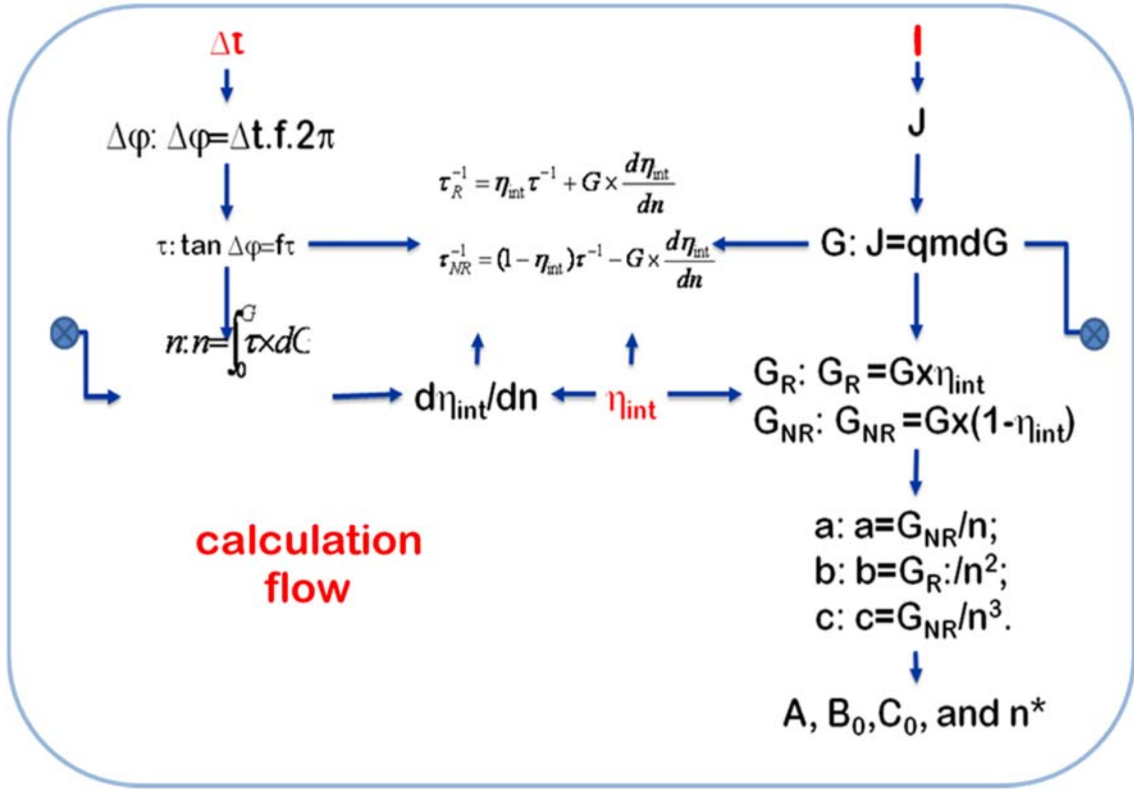

Fig. 3.10. Calculation flow for measuring differential carrier lifetime and analysis of radiative lifetimes, and A, B, C parameters.

carrier density. The calculated lifetimes τ_r and τ_{nr} are also plotted in Fig. 3.9(a) and (b) for QW and QD LEDs, respectively. Carrier leakage, if any, does not play any significant role in the analysis of lifetimes and comparison of the recombination processes in our present study. This is because differential lifetimes that are measured are analyzed independent of carrier densities to obtain the radiative and non-radiative lifetimes. Also, significant leakage would lead to a super-cubic dependence of current, and subsequently IQE, on carriers, however, such is not observed in the measured data.

It is evident from Fig. 3.9 that the trend of τ versus J is qualitatively similar at low

current densities, but is very different at higher injection levels. For the QD LED, τ exhibits a saturating behavior, while there is a sharp decrease with injection for the QW LED. To better understand these trends, it is necessary to examine the current density dependence of τ_{nr} and τ_r. The behavior of τ_{nr} is first analyzed. An undesirable feature common to both QW and QD LED is that τ_{nr} becomes smaller than τ_r at high injection levels, where real devices are operated. The variation of τ_{nr} with injection shows qualitatively similar behavior for both QW and QD LEDs. At low injection levels τ_{nr} increases with n in both devices, which is generally attributed to the saturation of defect-related deep levels (traps) [84]. However, at higher injection levels τ_{nr} decreases at a faster rate with injection in the QW device which, as reported earlier [80], is also true for double heterostructure devices [83]. To gain a better understanding of these trends the parameters describing radiative and non-radiative recombination, namely $a=R_{nr}/n$, $b=R_r/n^2$ and $c=R_{nr}/n^3$ were also evaluated. The variation of a, b and c with n for the QW LED is very similar to the trends reported and discussed by David *et. al.* [80]. The variation of b and c with n for the QD LED is also calculated. A fitting equation of $C = C_0/(1+n/N_{eff})$ is used to derive the Auger recombination coefficient. A reasonable fit to the variation of 'c' with carrier density is obtained by using $A = 1.65\text{x}10^7$ s^{-1}, $C_0 = 2.3\text{x}10^{-31}$ cm^6s^{-1} and $N_{eff} = 1.3\text{x}10^{18}$ cm^{-3}. The value of $C_0 = 5\text{x}10^{-30}$ cm^6s^{-1} obtained for the QW LED compares well with measurements reported earlier [22, 33]. A smaller Auger recombination coefficient for quantum dots compared to that for quantum wells (whose width is comparable to dot height), by more than an order of magnitude, is attributed to stronger carrier confinement and fewer available discrete states for the Auger process [80, 83, 85, 86]. The reduced efficiency droop measured in QD LEDs, as

observed in this study and earlier ones [49, 82], can be directly related to a smaller rate of Auger recombination in QDs. The steeper decrease in non-radiative lifetime τ_{nr} in the QW LED is also believed due to a higher rate of Auger recombination.

There are distinct differences in the variation of τ_r with J for QW and QD LEDs. First, the value of τ_r is considerably lower in the QD LED. At low injection the values of τ_r are 6 ns and 35.5 ns in the QD and QW LEDs, respectively. The numbers almost exactly match theoretically calculated values [48, 49] and confirm the smaller piezoelectric field in the dots. In the QW LED, τ_r increases very slightly with injection at low injection levels. This behavior has been attributed to delocalization of carriers from clusters to the quantum wells, where electrons and holes are separated by the piezoelectric polarization field, resulting in a longer radiative lifetime [67]. With increase of injection, the polarization field is reduced by carrier screening and τ_r decreases as observed in Fig. 3.9. On the other hand, τ_r increases steadily with J in the QD LED and suggests a capture bottleneck. The existence of such a bottleneck is well-known in In(Ga)As/GaAs self-organized quantum dots [87,88] and is a direct manifestation of the higher density of the two-dimensional wetting layer states compared to the number of available states in the dots [89]. Injected carriers occupy the wetting layer states and the relaxation time to the dot states can be very large, which in turn will increase the radiative recombination lifetime. A wetting layer is also formed during the self-organized growth of InGaN/GaN QDs and from *in-situ* reflection high energy electron diffraction (RHEED) observations during growth we estimate the thickness of this layer to be ~ 0.3-0.4 nm. The possibility of a capture bottleneck arising from a higher barrier to uniform hole injection due to the piezoelectric field can be ruled out, since such a barrier of larger

height also exists in the QW LED. The fitting was done using the relation $b=B_0/(1+n/N_{eff})$ and a value of $B_0 = 4.35 \times 10^{-11}$ cm^3s^{-1}. The fitting does improve when higher order terms, to take into account a capture bottleneck, are included. We obtain values of A, B_0 and C_0 equal to 1.65×10^{7} s^{-1}, 4.35×10^{-11} cm^3s^{-1} and 2.3×10^{-31} cm^6s^{-1}, respectively.

3.6 Summary

The growth and fabrication of QD LEDs were improved by optimizing the p-AlGaN EBL layer and improvement in processing of the devices to demonstrate improved output characteristics including efficiency peaking at lower current densities ~30 A/cm^2 with a reduced droop of only ~22% and low peak emission shift with injections corresponding to a low polarization field of ~80 kV/cm apart from good current-voltage characteristics. Differential carrier lifetime measurements were performed on blue emitting QD LEDs, and the measurements were compared to an equivalent QW LEDs to help understand the carrier dynamics responsible for different efficiency droop behavior and efficiency peaking current densities in both QW and QD devices. It is concluded that Auger recombination is possibly responsible for the high efficiency droop observed in QW LEDs while the value of Auger recombination coefficient was orders of magnitude lower in QD LEDs resulting in lower droop behavior.

Chapter IV

Self-Assembled InGaN/GaN Quantum Dots as Dislocation Filters

4.1 Introduction

The solid state lighting industry has been continually trying to improve the performance and yield of the light emitting diodes (LEDs) through improved epitaxy, device design and advancements in device processing and packaging. Epitaxy of the LED heterostructures has been a major roadblock in meeting the efficiency, yield and cost goals. As discussed in previous chapters, state-of-the-art quantum well (QW) LEDs suffer from low peak efficiencies and a large efficiency droop due to the large polarization field and a high dislocation density resulting from epitaxy on mismatched substrates. The incorporation of higher composition In to obtain longer green wavelength emission in InGaN/GaN QWs suffers from In clustering effects contributing to non-homogeneous emission and poor efficiencies [90]. Additionally, the high defect density of the available substrates for GaN crystal growth limits the performances of the LEDs. Sapphire is the current material of choice due to its affordability and the development of the growth technology in producing large single crystal GaN/sapphire wafers for commercial epitaxy of InGaN LEDs. However, the GaN-to-sapphire lattice mismatch is very high (13.8%) as shown in Table 1.1 and the resultant defect dislocation density in commercial state-of-the-art GaN/sapphire templates is ~1 x 10^9 cm^{-2}. This high threading

dislocation density degrades the device performance significantly.

This chapter proposes the use of self-assembled InGaN/GaN QDs as dislocation filter for reducing the defect density in the substrate before the epitaxy of LED heterostructures. Bhattacharya *et. al.* were the first to report the properties of QDs in reducing dislocation density in the arsenide material system [91]. In the present study, we demonstrate a reduction of the propagating threading dislocation density by use of an InGaN/GaN QD dislocation filter grown by plasma-assisted molecular beam epitaxy (PA-MBE). The composition of In in the InGaN/GaN quantum dots and the number of QD layers in the dislocation filter are optimized with calibrated etch pit dislocation density (EPD) measurements and theoretical calculations of dislocation propagation. Subsequent PA-MBE grown layers, including doped GaN and InGaN/GaN quantum dots, on top of the QD filter have been characterized. Multilayer GaN/AlN QDs [92, 93] have also been investigated to compare their dislocation filtering characteristics with those of the optimized InGaN/GaN QD filter. The dislocation filters have been incorporated in green-emitting QD LED heterostructures and the properties of these devices were compared with LEDs grown without any dislocation filter.

4.2 Design, Growth and Characterization of InGaN/GaN Quantum Dot Dislocation Filter

The molecular beam epitaxial (MBE) growth of InGaN/GaN QDs was optimized through calibrated etch pit dislocation (EPD) measurement and with the aid of theoretical calculations to obtain maximum dislocation filtering on GaN/sapphire templates. These are discussed in details in this section.

4.2.1 Growth of InGaN/GaN quantum dot dislocation filter

The heterostructures for etch pit dislocation (EPD) measurement shown in Fig. 4.1 were grown on c-plane n-GaN-on-sapphire templates with a typical dislocation density of ~$8x10^8$ cm^{-2}. The threading dislocation densities were calculated by careful and detailed calibration of EPD measurements on the templates and MBE grown GaN layers grown on such templates with and without quantum dot (QD) dislocation filters. As discussed in previous chapters, the growth temperature was measured by an infrared pyrometer, calibrated by the reflection high energy electron diffraction (RHEED) pattern transition from 7x7 to 1x1 on Si (111) substrates. An underlying n-doped ($5x10^{18}$ cm^{-3}) GaN buffer

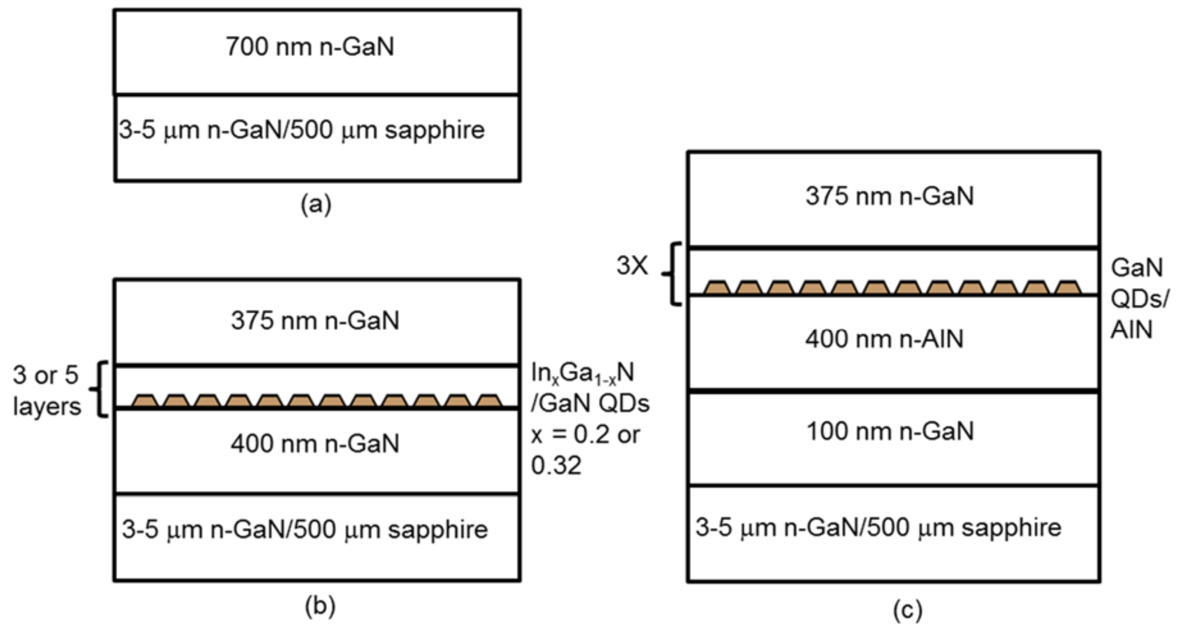

Fig. 4.1. Heterostructure schematics for etch pit dislocation measurements with: (a) no QD dislocation filter, (b) $In_xGa_{1-x}N$/GaN QD dislocation filters having 3 and 5 QD layers, and (c) dislocation filter having 3 GaN/AlN QD layers grown on relaxed AlN.

layer was first grown on c-plane n-GaN/sapphire templates for all samples. This layer was grown at 740°C at a flux of Φ_{Ga} = 4.5 nm/min, during which the RHEED pattern

remained bright and streaky. A heterostructure consisting of 700 nm of n-GaN buffer layer grown on the template without any QD dislocation filter, used as a control sample, is shown in Fig. 4.1(a). The heterostructures for determining the dislocation filtering effect of varying quantum dot composition and number of layers are shown in Figs. 1(b) and (c). The heterostructure shown in Fig. 1(b) has an underlying 400 nm of n-GaN buffer layer followed by the InGaN/GaN dislocation filtering quantum dots, 50 nm of low temperature GaN grown at the QD growth temperature of 565 ^{o}C, and a final 375 nm n-doped GaN layer grown at 740°C in which the dislocation density is measured. The QD layers were grown under N_2 rich conditions at a substrate temperature of 565 ^{o}C. Figure 1(c) shows a heterostructure grown with GaN/AlN QD filter under conditions reported earlier [93] and have demonstrated dislocation filtering properties [92].

4.2.2 Etch pit dislocation measurement

Defect-selective etching is a well-known technique for determining the dislocation density in GaN-based systems [94-96]. There are several methods of obtaining etch pits from selective etching of defects, however, they suffer from inconsistencies and anomalies [96]. In the experiments done here, etch pit dislocation densities were carefully measured on GaN/sapphire templates and calibrated with TEM measurements reported earlier [97] for MBE grown layers. The defects were selectively etched with a eutectic mixture of molten bases (NaOH, KOH and MgO – 53.6%, 37.3% and 9.1% by weight, respectively) at 450 ^{o}C. The control sample with 700 nm of n-GaN grown on a GaN/sapphire template without any QD filter has a threading dislocation density of 5×10^{8} cm^{-2}, calculated from the AFM image shown in Fig. 4.2(a). A dislocation filtering effect is observed in the sample with five layers of $In_{0.32}Ga_{0.68}N$/GaN QDs. The dislocations

merge to form larger pits, which cause an effective reduction of the total dislocation

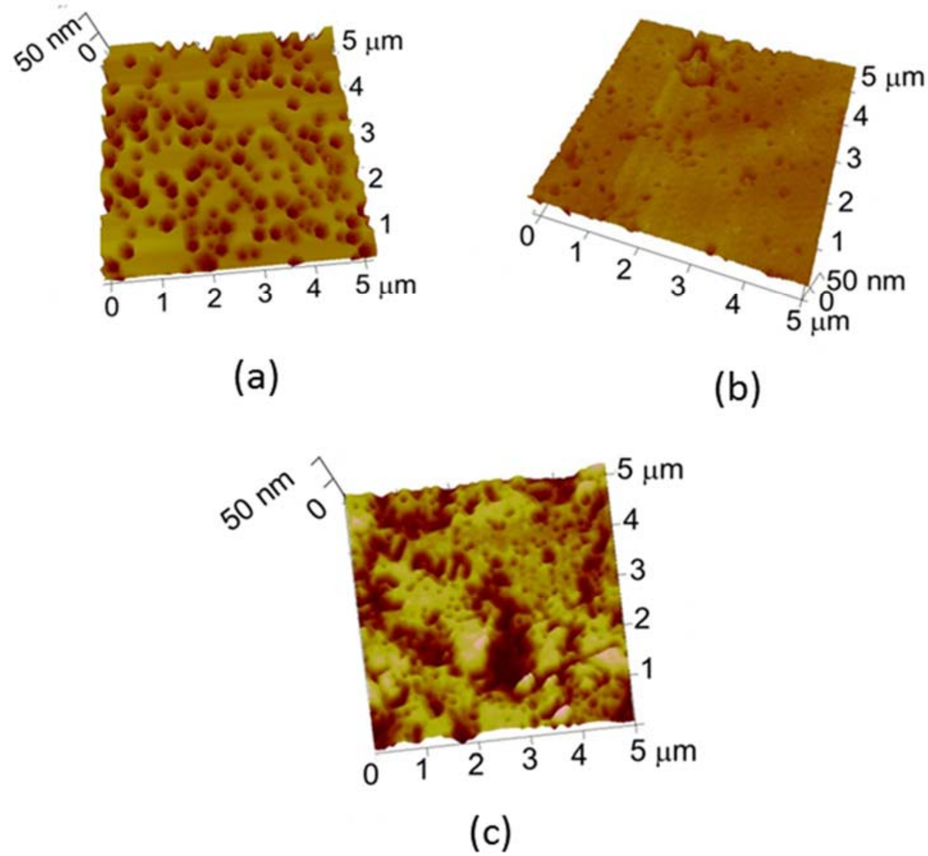

Fig. 4.2. Atomic force microscopy (AFM) images of the GaN surfaces after etch pit dislocation (EPD) treatment on (a) control sample without dislocation filter, (b) sample with 3 layers of $In_{0.2}Ga_{0.8}N$/ GaN QD dislocation filter, and (c) sample with 3 layers of GaN/AlN QD dislocation filter.

density to ~3x10^{8} cm^{-2}. The sample with the 5-period $In_{0.2}Ga_{0.8}N$/GaN QD filter having fewer etch pits and a dislocation density of ~2.7x10^{8} cm^{-2}, which further reduced with three periods of dot layers (Fig. 4.2(b)) to a dislocation density of ~9.8x10^{7} cm^{-2}.

After optimization of the growth of GaN/AlN quantum dots on relaxed AlN buffer layers [93], an n-GaN layer grown on top of the optimized GaN/AlN QD filter was used to determine the etch pit density by AFM imaging (Fig. 4.2(c)). It was found that the GaN/AlN QD filter was less effective than the InGaN/GaN QD filter in reducing the

dislocation density, possibly because they were grown over a relaxed AlN layer which may contain more dislocations than the state-of-the-art commercial GaN/sapphire templates used in our study. The results from AFM measurements of the samples after EPD experiments are summarized in Table 4.1. It should be noted that several AFM measurements were performed on each sample to reduce measurement error in estimation of dislocation density.

4.2.3 Theoretical calculation

From energy minimization considerations, it has been shown that for misfit ≥2%, the island growth mode is preferred [98]. In general the islands are coherently strained, but may also be partially relaxed. In particular, with continuing growth of larger islands,

Sample type	Quantum dots	Number of layers	Average dislocation density (cm^{-2})
GaN with no QD filter	N/A	N/A	5.0±0.5x10^8
GaN on $In_xGa_{1-x}N$/GaN QD filter	$In_{0.32}Ga_{0.68}N$/GaN	5	3.1±0.4x10^8
	$In_{0.2}Ga_{0.8}N$/GaN	5	2.7±0.6x10^8
	$In_{0.2}Ga_{0.8}N$/GaN	3	9.8±0.5x10^7
GaN on GaN/AlN QD filter	GaN/AlN	3	3.5±0.5x10^8

Table 4.1. Description of the samples used for etch pit dislocation density measurements.

the coherency degrades beyond a critical size with the generation of misfit dislocations. Figure 4.3(a) is a transmission electron microscopy (TEM) image of a sample with seven layers of $In_{0.2}Ga_{0.8}N$ QDs showing how dislocations may propagate or get annihilated at the quantum dot layers, depending on composition and size of the dots. It can be seen from Fig. 4.2(b) that three layers of lower composition $In_{0.2}Ga_{0.8}N$ QDs work as a good

dislocation filter. A larger number of dot layers increases the mismatch strain, which may lead to the generation of new misfit dislocations in the uppermost QD layers. The bending of dislocations with In(Ga)As/GaAs quantum dot multilayers has been

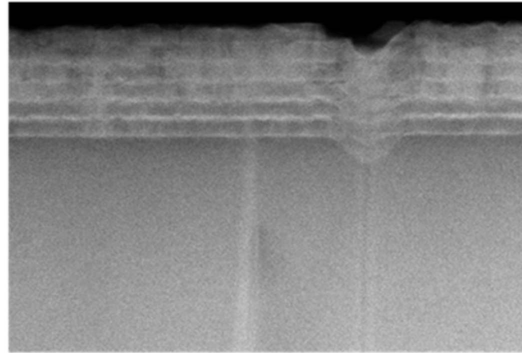
(a)

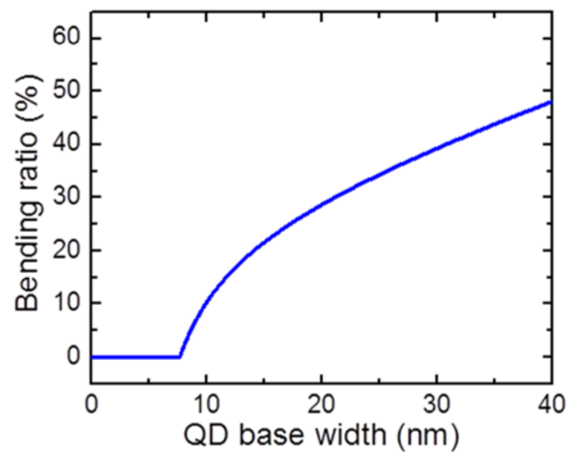

(b)

Fig. 4.3(a) Dark field transmission electron microscopy image showing annihilation and propagation of dislocation through QD dislocation filter and (b) calculated bending ratio of threading dislocation as a function of dot base width.

previously modeled by Bhattacharya *et. al.* [99]. According to this model dislocation bending will occur when the strain energy released by the generation of a misfit dislocation is equal to or greater than the dislocation self energy. The bent misfit dislocation glides underneath the islands. Figure 4.3(b) shows the calculated bending area

ratio of $In_{0.2}Ga_{0.8}N$ QDs as a function of the QD base width. The bending area ratio of a single QD is defined as the bending area divided by the area of the QD base. From this figure, it is apparent that for $In_{0.2}Ga_{0.8}N$/GaN QDs with a base width of ~30nm the bending ratio is ~30%, which is similar to the dislocation density reduction seen for the sample shown in Fig. 4.2(b). Further increase of the In composition in the dots or increasing the number of dot layers possibly leads to the generation of new misfit dislocations, which is seen in the other samples. Alternatively, for a dot composition of less than 20% In, sufficient mismatch strain for island formation may not be generated.

4.2.4 Deep level traps in n^+-p GaN junctions on quantum dot dislocation filter

In order to investigate the effect of the QD dislocation filter on the characteristics of deep level traps in the material grown on top of it, transient capacitance measurements were made on suitable junction diodes. Measurements were made on two samples. In Sample I, 600 nm of Si-doped n-GaN was grown on a GaN-on-sapphire template with a doping concentration of n ~9.2×10^{18} cm^{-3}, followed by 400 nm of Mg-doped p-GaN with a doping level of p ~5×10^{17} cm^{-3}. Sample II is identical to sample I except the n^+-p GaN junction diode was grown on top of the optimized multilayer $In_{0.2}Ga_{0.8}N$ QD dislocation filter. The diodes were mounted in a closed-loop He cryostat and the capacitance transients due to deep level emission were measured by a Boonton 1 MHz capacitance meter. The transient data was analyzed to determine the trap activation energy and capture cross-section in accordance with the equation:

$$1/\tau = \sigma v_{th} N_{c(v)} exp(-\Delta E/kT) \qquad (1)$$

where τ is the trap emission time constant, v_{th} is the thermal velocity, $N_{c(v)}$ is the density of states in the conduction (valence) band, and ΔE and σ are the trap activation energy

and capture cross-section, respectively. It is being assumed that ΔE and σ are not thermally activated. The trap concentration N_T

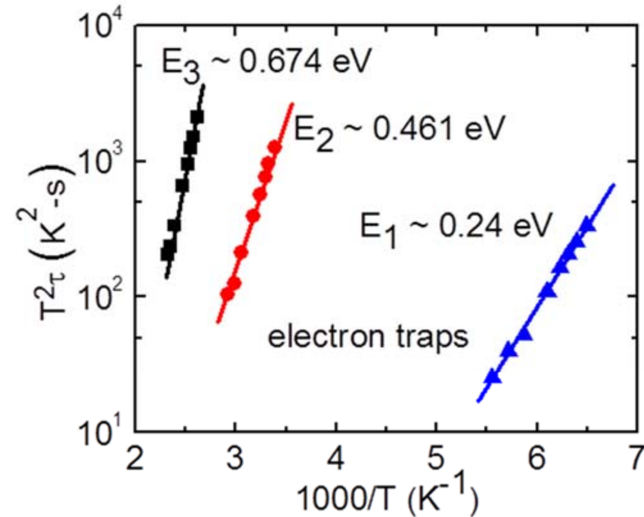

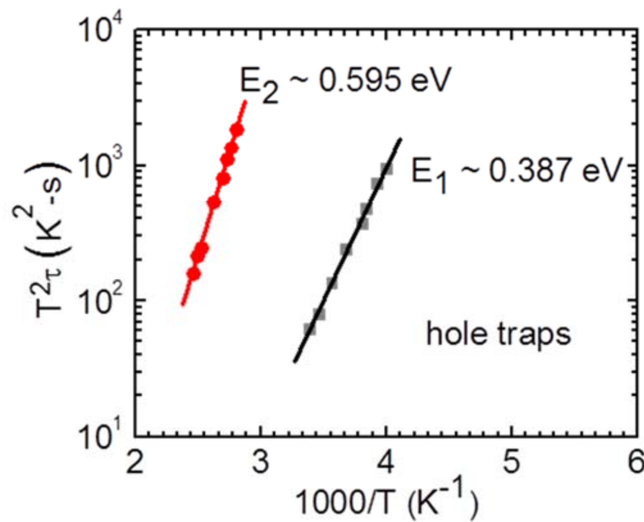

Fig. 4.4(a) Arrhenius plot of the emission time constant versus reciprocal temperature for (a) electron traps and (b) hole traps measured in n^+-p GaN diodes grown without a dislocation filter.

was estimated from the change ΔC in the n^+-p diode capacitance during the trap filling cycle of the applied bias. Due to the doping asymmetry of the grown junctions, the deep

levels in the lightly doped p-GaN layer were probed by the capacitance measurements.

The background doping in this layer was accurately determined by capacitance-voltage measurements. Both minority carrier (electron) and majority carrier (hole) traps were characterized with suitable biasing sequences. The characteristics of the traps in the control diode (Sample I) and the diode grown on the dislocation filter (Sample II) are summarized in Table 4.2. The dominant electron traps have activation energies ΔE = 0.24, 0.461, and 0.674 eV and the hole traps are characterized by ΔE = 0.387 and 0.595 eV as shown in Figs. 4.4(a) and (b), respectively. In examining the trap densities it is evident that there is a general reduction in all trap densities, as much as by a factor of 3, by the incorporation of the QD dislocation filter. Similar observations have been reported on using a SiN filter on GaN template [100]. The reduction in trap density is, in general, in agreement with the reduction in dislocation density due to the incorporation of the filter. Edge and screw dislocations are known to contribute to the formation of traps and the localization of carriers. It seems, therefore, that the traps identified here are directly or indirectly related to the dislocations in the material.

4.3 Optical Properties of Green-Emitting Quantum Dot active Region on Dislocation Filter

Temperature dependent and time resolved photoluminescence (TRPL) measurements were performed on green-emitting QD samples without (sample A) and with (sample B) optimized dislocation filter incorporated in the GaN buffer layer underneath. The samples were mounted in a closed loop He cryostat and excited non-resonantly by a frequency tripled and pulsed 80 MHz mode-locked Ti:Sapphire laser

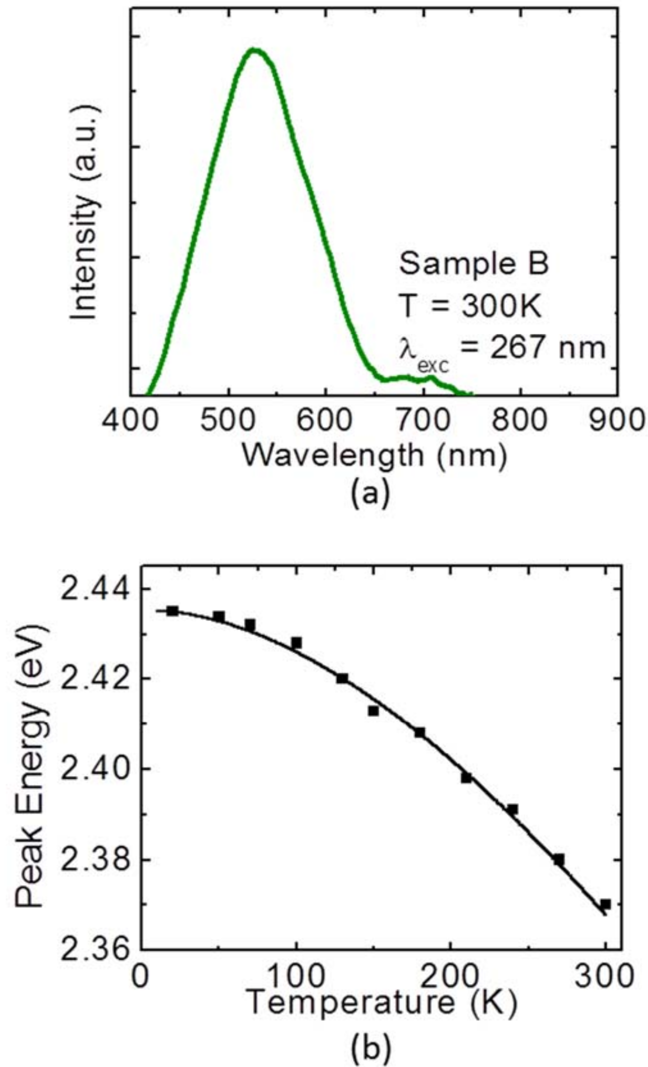

Fig. 4.5(a) Photoluminescence spectrum of the $In_{0.35}Ga_{0.65}N$/GaN QDs grown on QD dislocation filters and (b) temperature dependence of the peak emission energy showing a good fit with the Varshni equation.

(hυ=4.66 eV). The luminescence was analyzed by a monochromator (resolution ~ 0.03 nm) and focused on to a single photon detector (measured system response time ~ 50 ps). Growth of green-emitting $In_{0.35}Ga_{0.65}N$/GaN QD layers in the active region was optimized [49, 101] to have strong room temperature photoluminescence (PL), as shown in Fig. 4.5(a). The variation of the peak energy of the PL spectra of sample B with

temperature is plotted in Fig. 4.5(b). The trend closely follows the Varshni equation [70]. Furthermore, no "S-shaped" behavior was observed in the data. The similarity of the trend of these data with those measured on InGaN/GaN QDs without any dislocation filter [102] suggests that the incorporation of the QD filter does not give rise to any compositional non-uniformity or clustering effects.

GaN n^+-p diodes	Electron traps			Hole traps		
	ΔE (eV)	σ (cm^2)	N_T (cm^{-3})	ΔE (eV)	σ (cm^2)	N_T (cm^{-3})
Device I w/o dislocation filter	0.24	$5.154x10^{-16}$	$2.11x10^{15}$	0.387	$5.08x10^{-17}$	$3.62x10^{16}$
	0.461	$2.242x10^{-16}$	$5.12x10^{15}$	0.595	$1.136x10^{-16}$	$6.25x10^{16}$
	0.674	$1.22x10^{-15}$	$4.63x10^{15}$			
Device II with dislocation filter	0.236	$3.86x10^{-16}$	$9.23x10^{14}$	0.392	$6.34x10^{-17}$	$1.68x10^{16}$
	0.464	$2.52x10^{-16}$	$2.92x10^{15}$	0.591	$1x10^{-16}$	$3.72x10^{16}$
	0.67	$1.08x10^{-15}$	$2.07x10^{15}$			

Table 4.2 Characteristics of deep levels in GaN obtained from transient capacitance measurements.

From temperature dependent PL measurements, the five layers of $In_{0.35}Ga_{0.65}N$/GaN QD layers grown without (Sample A) and with (Sample B) $In_{0.2}Ga_{0.8}N$/GaN QD filter yield an internal quantum efficiency (IQE) of ~26% and 40.5%, respectively, assuming all non-radiative centers are frozen at low temperatures (Fig. 4.6(a)). It should be noted that the efficiencies were measured as a function of injection excitation density and were compared for high excitation densities where the efficiency gets saturated and is independent of In clustering effects or high polarization fields. The improved efficiency of the quantum dots in sample B is believed to be a direct consequence of the reduced dislocation density and consequent reduction of the density of non-radiative centers, such as the deep levels described earlier.

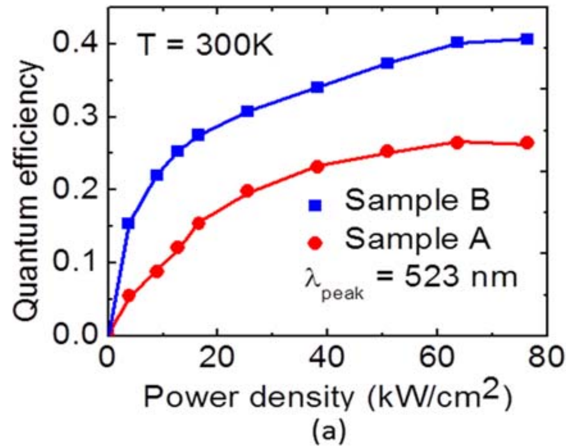

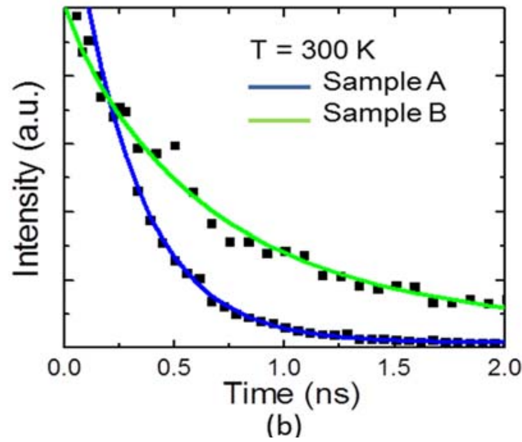

Fig. 4.6(a) Excitation dependence of quantum efficiency in $In_{0.35}Ga_{0.65}N$/GaN QD samples grown without (sample A) and with (sample B) dislocation filter. The solid lines are joins of the data points and (b) luminescence decay transients measured for samples A and B. The solid lines are obtained from the rate equations.

Carrier recombination dynamics were obtained for both the samples at room temperature from TRPL measurements. The luminescence decay transients are shown in Fig. 4.6(b). The total carrier recombination time for sample A and sample B are estimated to be 464 ps and 550 ps, respectively. The increase in recombination lifetime in sample B reflects an increase in the non-radiative lifetime in the QDs, resulting in an increase of the internal quantum efficiency. Additionally, the lifetimes show a single exponential decay even when grown on top of QD dislocation filter indicating absence of any In clustering effect due to the dislocation filter underneath.

4.4 Output Characteristics of Green-emitting QD LEDs on QD Dislocation Filter

The LED heterostructure, shown schematically in Fig. 4.7, has five periods of green-emitting $In_{0.35}Ga_{0.65}N$/GaN QDs grown at a substrate temperature of 530 °C under N_2 rich conditions at an equivalent pressure of Φ_{Ga}: Φ_{In} ~ 1:1 and at a quantum dot growth rate of 0.5 Å/s. The LEDs were grown with no dislocation filter (device A), the optimized InGaN/GaN dislocation filter as shown in Fig. 4.7 (device B), and with the optimized GaN/AlN QD dislocation filter (device C). The active region was grown on n-GaN above the dislocation filter and followed by a 13 nm thick $Al_{0.15}Ga_{0.85}N$ electron

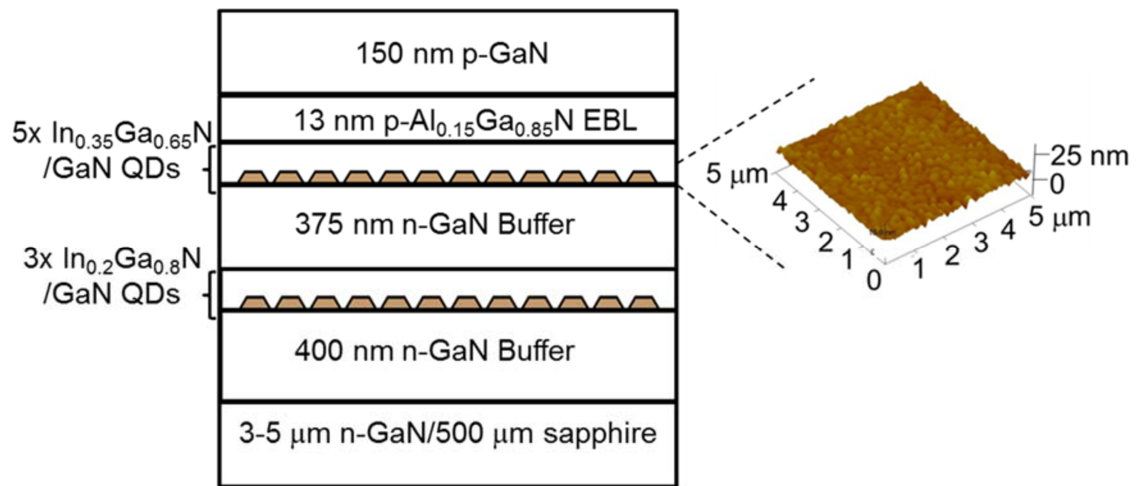

Fig. 4.7. A typical green-emitting InGaN/GaN QD LED heterostructure with QD dislocation filter and an AFM image of the green-emitting dots shown alongside.

blocking layer grown at 750°C and a final p-doped GaN layer (p~7×10^{17} cm^{-3}) for injection of holes. Mesa-shaped LEDs of dimension 400 µm x 400 µm were fabricated using standard photolithography, reactive ion etching (RIE), and contact metallization techniques as discussed in section 3.3.1. An AFM image of an uncapped layer of $In_{0.35}Ga_{0.65}N$/GaN QDs is shown in the inset to this figure with the dots having an

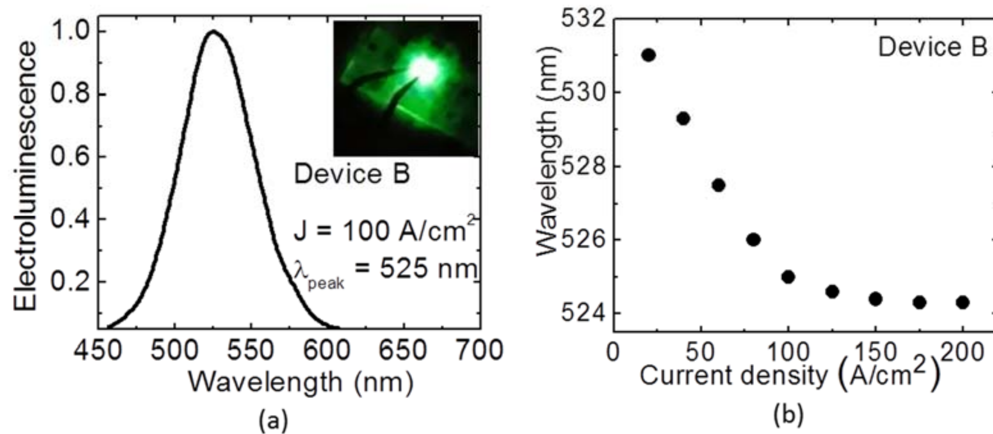

Fig. 4.8 A typical green-emitting InGaN/GaN QD LED heterostructure with QD dislocation filter and an AFM image of the green-emitting dots shown alongside.

average height of ~3nm and base width of ~30nm.

The three green-emitting QD LEDs were characterized by current-voltage (I-V) and light-current (L-I) measurements under pulsed bias with a 5% pulse width and 1 ms period. The measured electroluminescence (EL) spectrum at a current density of 100A/cm^2 is shown in Fig. 4.8(a) for Device B having the strongest luminescence with peak at 525 nm. The micrograph of an active device is shown in the inset. The variation of the peak emission energy with injection current is shown in Fig. 4.8(b). The total peak emission blue shift of 6.2 nm corresponds to a polarization field of ~88 kV/cm, which is much smaller than values of 2-3 MV/cm measured in equivalent quantum well-based devices [77, 78]. The polarization field is also in agreement with values for InGaN/GaN quantum dots reported earlier. Figure 4.9(a) shows the measured I-V characteristics of all the three devices. It is evident that the LED grown on GaN/AlN dislocation filter (Device C) has a very high leakage current below the turn-on voltage while Device B with an optimized InGaN/GaN dislocation filter has the smallest leakage current. Additionally, Device B exhibits a sharp increase in forward current beyond the turn-on voltage, which

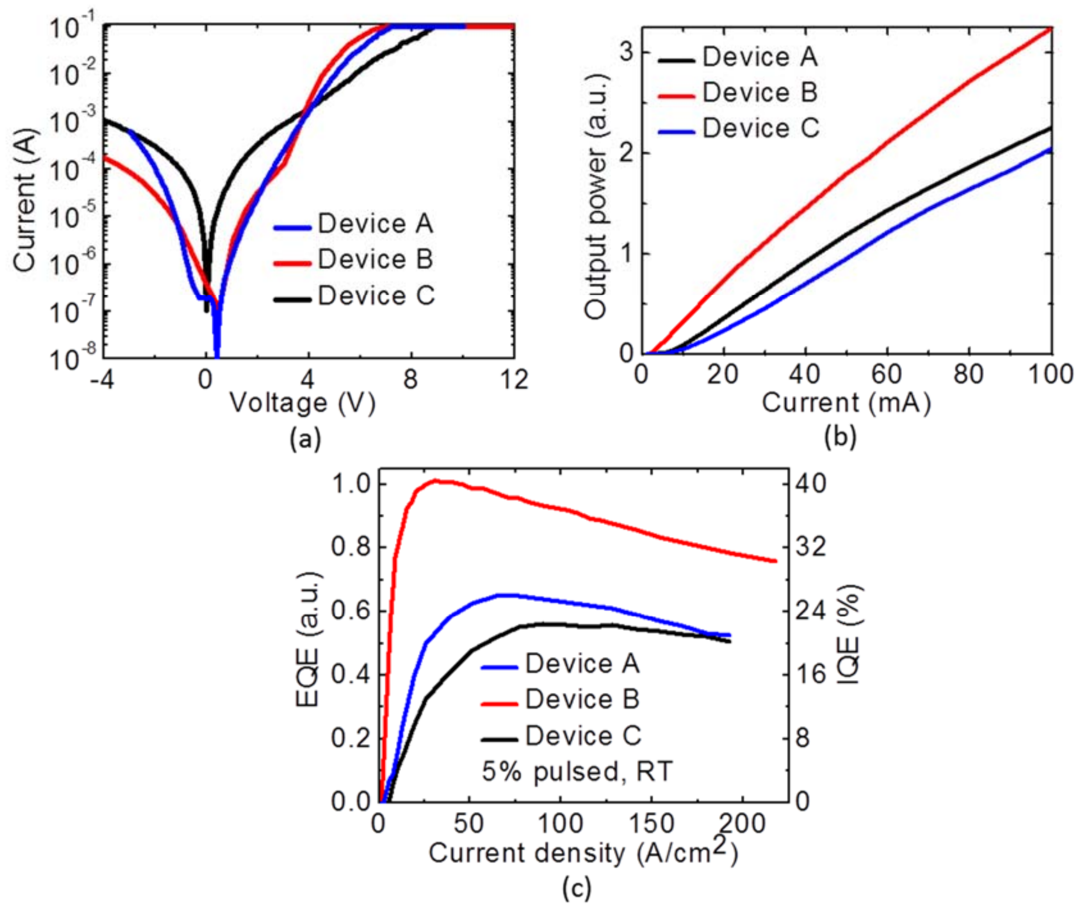

Fig. 4.9 Measured current-voltage characteristics(a), light-current characteristics(b), and external quantum efficiency as a function of injection current density(c) for green-emitting QD light emitting diodes with and without QD dislocation filters.

results in higher currents at low forward voltages compared to the LEDs without dislocation filters. The turn-on voltage is ~3.5 V with a series resistance of less than 10 Ω for this device.

Light-current measurement data from the three LEDs A, B and C are shown in Fig. 4.9(b). Device B was found to have a significantly higher light output at similar current densities compared to devices A and C which have higher dislocation densities in the active region. The data is also in agreement with the observed trends of radiative efficiency and deep level trap density. Threading dislocations have been reported to play

a key role in the formation of compositional inhomogeneity and the formation of non-radiative recombination centers in the active region. This situation gets particularly aggravated during the high temperature growth of the subsequent p-GaN layer when the InGaN material near threading dislocations can get decomposed and form more non-radiative centers [103, 104]. Figure 4.9(c) shows the external quantum efficiencies (EQE) measured for the different LEDs. It should be noted that the measured EQE is in arbitrary units and the relative values in the three devices are of importance here. The peak efficiency of device B is substantially higher than those of devices A and C. The injection current density at peak efficiency are J_{max} = 65 A/cm^2, 27 A/cm^2 and 75 A/cm^2 for devices A, B and C, respectively. A large radiative recombination rate of carriers at low current densities indicates reduced Shockley-Read-Hall (SRH) recombination. At high current densities (~ 200 A/cm^2) the efficiency of device B remains much higher than those of devices A and C. The efficiency droop calculated for device B is ~22.6% between injection current densities of 27 A/cm^2 and 192 A/cm^2, which is lower than those measured in green-emitting state-of-the-art c-plane quantum well LEDs.

4.5 Summary

In conclusion, 3 layers of self-assembled $In_{0.2}Ga_{0.8}N$/GaN QD layers have been optimized and used as a dislocation filter to obtain significant reduction in dislocation density to ~9.8x10^7 cm^{-2} from calibrated etch pit dislocation measurement. The optimized QD dislocation filter lead to fewer traps in GaN n$^+$-p junctions, and improved the optical properties of the green-emitting (λ =525 nm) QDs showing improved IQE (~40%) and longer carrier lifetimes. Finally, green-emitting QD LEDs were grown on

dislocation filter and their electrical and optical properties characterized and compared to QD LEDs without filter. The LEDs on filter have a higher light output with efficiency peaking at a low current density of 27 A/cm^2. This technique could be used to obtain better performances from LEDs grown on mismatched substrates including GaN-on-sapphire or GaN-on-silicon.

Chapter V

InGaN/GaN Quantum Dot Lasers

5.1 Introduction

Visible solid state lasers find many large scale applications in various fields including in blue-ray disc readers, medical prostatectomy, military dazzlers, pico-projectors and heads-up displays in automobiles [105, 106]. Diode-pumped solid state lasers have been used to emit blue and green light and can be energy efficient. Thereby, there has been large scale research to develop commercial blue and green emitting InGaN/GaN lasers. State-of-the-art commercial nitride based lasers incorporate InGaN/GaN quantum wells (QW) in the active region [10, 11, 77, 107-109]. As discussed in earlier chapters, these quantum wells have a strong inherent polarization field, and the associated band bending causes poor electron-hole wavefunction overlap, poor radiative efficiencies, blueshift of peak emission with current density due to the quantum confined Stark effect (QCSE) and a high leakage of carriers in devices incorporating such QWs in the active region. Additionally, the incorporation of more In, necessary to obtain longer (green) wavelength emission in InGaN/GaN QWs, leads to In clustering effects contributing to non-homogeneous emission and poor radiative efficiencies. A critical parameter in the operation of a junction laser is the threshold current, which in turn determines the overall power conversion efficiency. The threshold

current in addition to the dynamic characteristics of a laser are ultimately determined by the differential gain, dg/dn, and hence it is important to optimize this paramter as well. The current state-of-the-art InGaN/GaN QW lasers suffer from a very high threshold current density of lasing as was discussed in chapter 1. Recently, laser diodes have been demonstrated on the non-polar GaN planes (most often the m-plane) which have reduced polarization field as compared with c-plane QW laser structures [11, 110]. However, difficulty in incorporating higher composition of In in the InGaN/GaN QWs can impede the growth and performance of lasers grown on these substrates [111, 112]. Alternatively, the use of quantum dots in the active region of visible lasers grown on polar c-GaN promises improved performance due to increased carrier confinement, smaller piezoelectric field, smaller quantum confined Stark effect (QCSE) and blue shift of the emission peak, reduced carrier recombination lifetimes and a smaller rate of recombination at dislocations and defects [47-49]. Additionally, the growth of such lasers have been carried out by plasma-assisted molecular beam epitaxy (MBE) which has lagged behind the growth and demonstration of nitride visible devices using Metal Organic Chemical Vapor Deposition (MOCVD). Bhattacharya *et. al.* have successfully demonstrated QD lasers grown by MBE emitting in the blue [101, 113, 115, 116] and green [114] wavelengths.

This chapter discusses the growth calibration for optimizing the various layers in the laser heterostructure including the full laser heterostructure, their fabrication in ridge geometry waveguide devices and finally, the results obtained from extensive characterization of their optical properties. The challenges and design constraints in obtaining a nitride QD laser are also discussed when possible. The characteristics of blue

and red-emitting QD lasers are described.

5.2 Design and Growth of InGaN/GaN Quantum Dot Laser Heterostructures

The laser heterostructure, as shown in Fig. 5.1(a), were grown by a plasma-assisted Veeco Gen II molecular beam epitaxy (PA-MBE) system equipped with standard Ga, In,

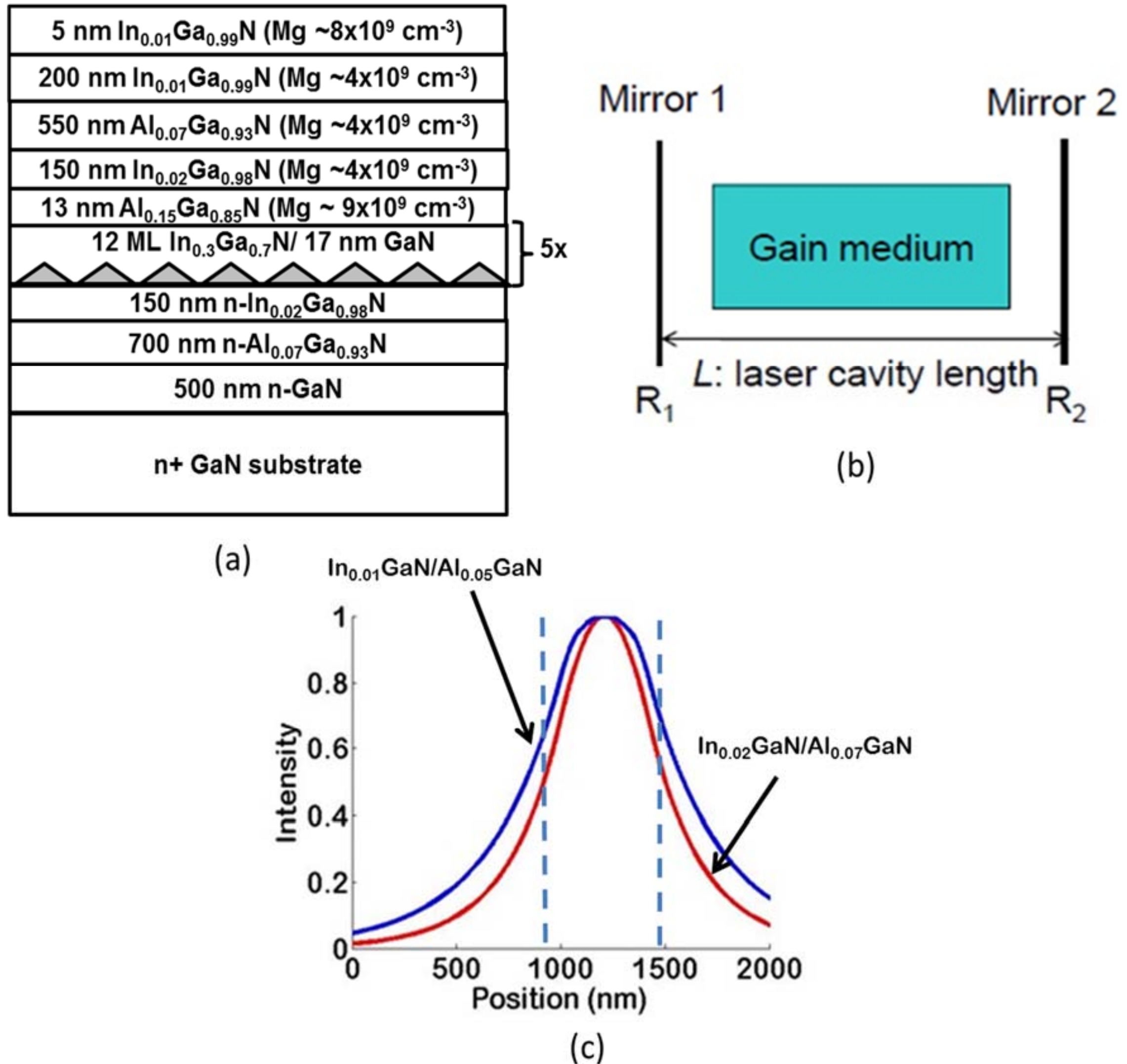

Fig. 5.1(a) Schematic of InGaN/GaN quantum dot laser heterostructure grown on a n-GaN bulk substrate with corresponding Mg flux used for each layer mentioned, (b) schematic of gain + feedback mechanism for laser operation, and (c) simulated transverse optical mode profiles for two different combinations of InGaN waveguide/AlGaN cladding layers. The dashed lines indicate the waveguide region.

Al, Si, and Mg effusion cells, and a UNI-bulb nitrogen plasma source as described previously. However, unlike the growth characteristics and optimization of the InGaN/GaN QDs and QD LED growth, the samples for QD lasers were grown on c-plane of n-GaN bulk substrates having a low defect density of ~$5x10^6$ cm^{-2}. Five hundred nanometers of molybdenum was also deposited on the backside of the samples to assist in the calibration of the growth temperature using radiative heating. The growth temperature of each layer was measured by an infrared pyrometer as outlined in previous chapters.

Any semiconductor laser structure needs a population inverted gain medium and a feedback mechanism for maintaining sufficient number of photons to cause stimulated emission and to sustain lasing (Fig. 5.1(b)). The gain medium for our devices is a series of InGaN/GaN QD layers which due to their reduced density of states can be inverted easier (with less current injection) than a InGaN/GaN QW active region or a bulk double heterostructure active region [117]. Consequently, the differential gain of QD lasers was found to be higher than equivalent QW devices from cavity length dependent current-output (L-I) measurements performed on the lasers which matches very well with simulated values. This gain medium helps in demonstrating of lasers with reduced threshold current density, and other superior optical properties as discussed in the subsequent sections. The feedback mechanism required for lasing is the cavity confinement of photons and the requirements are similar to QW lasers. The longitudinal confinement is obtained by cleaving along the m-plane to create facet mirrors, followed by dielectric distributed Bragg reflector (DBR) mirror deposition discussed in details in section 5.3. The transverse and lateral confinement of photons is accomplished by using a

low refractive index cladding outside the high refractive index waveguide core (index guiding). The optical mode along the transverse (growth) direction is confined with AlGaN. Simulations were performed using transfer matrix method to determine the optical mode confinement for various compositions of InGaN waveguide and AlGaN cladding (Fig. 5.1(c)). Higher In composition in InGaN waveguide, and higher composition Al in AlGaN create a larger refractive index mismatch and confine the optical modes better (larger optical confinement factor) as shown in Fig. 5.1(c). However, using these materials leads to additional strain and the formation of defects which lead to non-radiative recombination and electrical leakage path degrading laser performance significantly. Thereby, the design constraint for the nitride material system becomes very tight and efforts are made to grow as large a composition of InGaN and AlGaN possible without creating defects. This requires extensive calibration of these layers, followed by characterization of QDs on top of the strained AlGaN cladding and InGaN waveguide layers. These growth calibrations are covered in this section followed by the discussion of the full laser growth.

5.2.1 Growth of AlGaN cladding layer

The c-plane n-GaN bulk substrates were first cleaned using standard solvents, and then thermally degassed in two steps at 200 °C (60 min) followed by 450 °C (60 min) to reduce surface contamination. After cleaning, a 500 nm thick, n-doped ($5x10^{18}$ cm^{-3}) GaN buffer layer was grown at 740 °C, at a flux of Φ_{Ga} = 4.5 nm/min during which the RHEED pattern remained bright and streaky. PL shows strong band edge emission with no defect bands in the GaN spectrum. Following the growth of the buffer layer, samples with 700 nm of n-doped AlGaN (n~$5x10^{18}$ cm^{-3}) with different Al compositions were

grown and their structural and optical properties characterized to determine the optimum

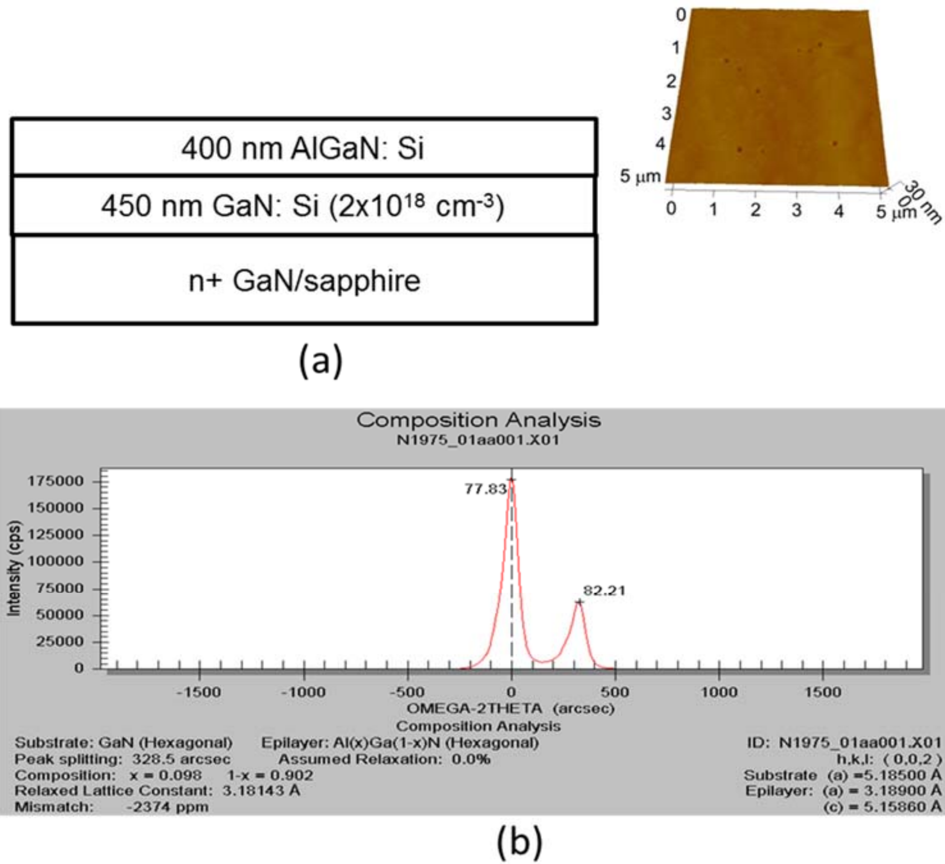

Fig. 5.2(a) Schematic of heterostructure for AlGaN cladding layer calibration. A 5µm x 5µm AFM image showing the surface morphology of 700 nm $Al_{0.098}Ga_{0.902}N$ layer and (b) XRD data of $Al_{0.098}Ga_{0.902}N$ grown on GaN.

growth conditions for the highest composition AlGaN that can be grown without relaxation or creation of defects and associated trap levels. Figure 5.2(a) shows a typical heterostructure that was grown on GaN/Sapphire templates and eventually on GaN bulk substrates for growth optimization. The AlGaN layer was grown at the same substrate temperature (T_{sub} = 740 ºC) as the buffer GaN to reduce growth interruption at the interface which were found to create pit formation from defects as seen from atomic force microscopy (AFM) measurements. Growth of AlGaN was carried out at a flux ratio of Al:Ga (1:9) similar to the required composition of AlGaN layer under metal-rich

conditions. A higher composition $Al_{0.098}Ga_{0.902}N$ layer grown on GaN bulk substrate, as shown in Fig. 5.2(a) were found to have excellent X-Ray Diffraction (XRD) spectra indicating very narrow linewidths for the GaN and AlGaN layers (Fig. 5.2(b)). However, the AFM measurements for the same layer (inset to Fig. 5.2(a)) showed termination of the growth with formation of pits possibly from defect creation during the strained AlGaN layer growth. A lower composition of $Al_{0.07}Ga_{0.93}N$ layer was grown and optimized to show improved AFM characteristics (smoother surface) without formation of pits as shown in Figs. 5.3(a). Additionally, photoluminescence (PL) measurements were performed to confirm the absence of any optically active trap levels in the AlGaN layer (Fig. 5.3(b)). The properties of the XRD spectra remained similar with lowered Al composition but the improved AFM coupled with the good PL properties demonstrated that it was well calibrated for incorporation in the laser heterostructure as cladding layer.

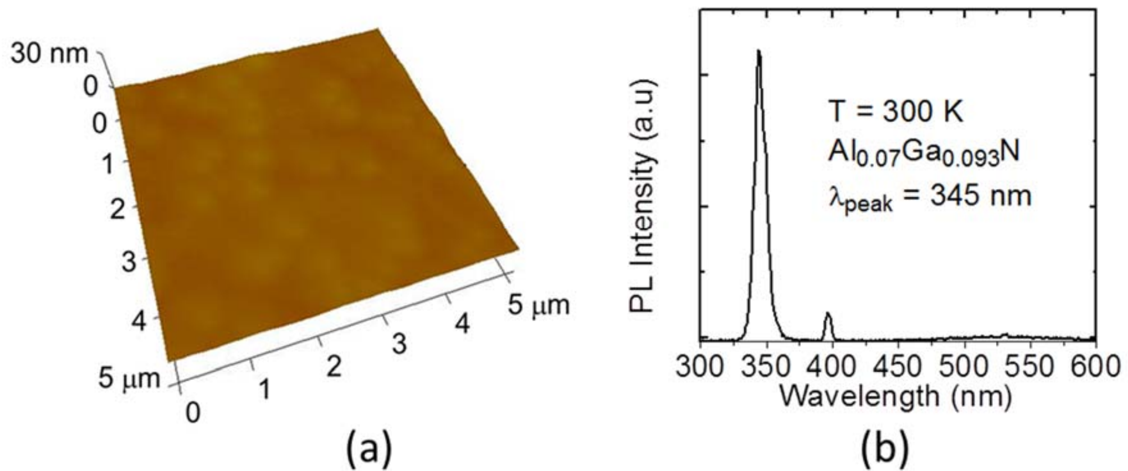

Fig. 5.3(a) A 5µm x 5µm AFM image showing the surface morphology of 700 nm $Al_{0.07}Ga_{0.93}N$ layer and (b) PL of $Al_{0.07}Ga_{0.93}N$ grown on GaN.

5.2.2 Growth of InGaN waveguide layer on top of AlGaN cladding layer

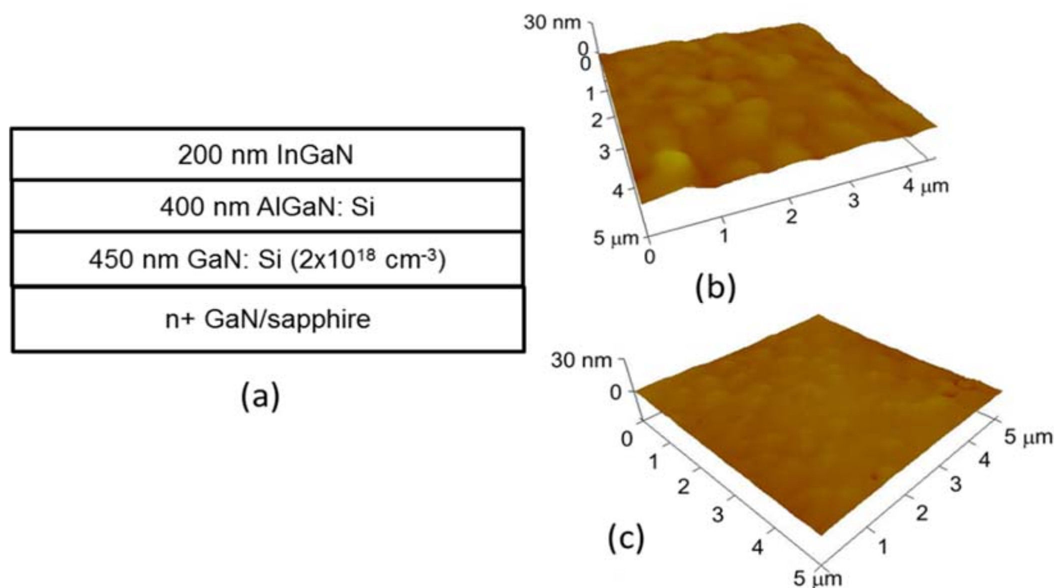

Fig. 5.4(a) Schematic of a typical heterostructure for InGaN waveguide layer calibration. A 5μm x 5μm AFM image showing the surface morphology of different In composition (b) $In_{0.05}Ga_{0.95}N$ and (c) $In_{0.02}Ga_{0.98}N$ waveguide layers.

After growth of a 500 nm thick buffer layer and a 700 nm n-$Al_{0.07}Ga_{0.93}N$ cladding layer, a 150 nm thin layer of undoped InGaN was grown with a typical heterostrucutre shown in Fig. 5.4(a). It should be noted that this layer was calibrated on GaN/sapphire template. To get reasonable In incorporation in the layers and due to the high vapor pressure of In, InGaN layers were grown at a lower T_{sub} = 590ºC for $In_{0.02}Ga_{0.98}N$ layers. However, the growth temperature was much higher than that for InGaN QD layer to get a lower composition InGaN without the initiation of 2D-3D transitions from the accumulation of strain. Figs. 5.4(b) and (c) show AFM images of the surface morphology of two samples grown with different composition $In_{0.05}Ga_{0.95}N$ and $In_{0.02}Ga_{0.98}N$ layers respectively on top of $Al_{0.07}Ga_{0.93}N$ cladding layer. The surface morphology became bad and had a poor

crystalline quality when the In composition was high as seen from Fig. 5.4(b). Thereby, a lower In composition $In_{0.02}Ga_{0.98}N$ with smoother morphology (Fig. 5.4(c)) was used for the laser heterostructure even though the optical mode was poorly confined. It should also be noted that the InGaN layer in the actual laser heterostructure was also kept undoped to reduce losses due to free carrier absorption in the waveguide layer.

5.2.3 The laser heterostructure

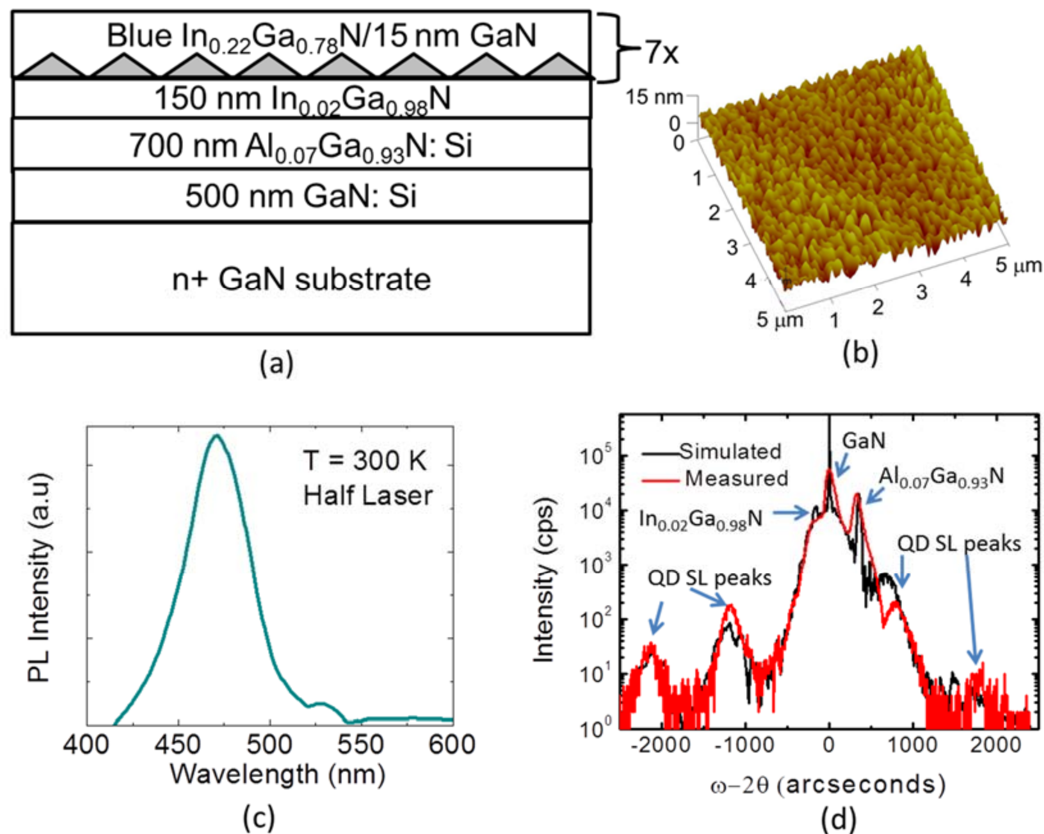

Fig. 5.5(a) Schematic of a typical half laser heterostructure for calibration of the AlGaN cladding, InGaN waveguide and topmost QD layers. (b) A 1μm x 1μm AFM image of the blue $In_{0.22}Ga_{0.78}N$/GaN QDs, (c) room temperature PL of the blue $In_{0.22}Ga_{0.78}N$/GaN QDs, and (d) XRD of the half laser heterostructure showing very good fit with dynamical diffraction theory.

A schematic of a typical laser heterostructure is shown in Fig. 5.1(a) with green-emitting

$In_{0.3}Ga_{0.7}N/GaN$ QDs in the active region. The heterostructure for blue lasers is similar except that the active region has the optimized blue-emitting $In_{0.18}Ga_{0.82}N/GaN$ QDs in the active region. The laser heterostructures were grown on free-standing GaN substrates with a reduced defect density ~$5x10^{6}$ cm^{-2} by Veeco Gen II and Gen 930 plasma-assisted molecular beam epitaxy (MBE) system. As outlined previously, after cleaning the n-GaN bulk substrates and degassing in two steps, 500 nm of Si-doped GaN ($n \sim 5x10^{18}$ cm^{-3}) was grown at a nitrogen flux fixed at 0.5 sccm with an RF power of 300 W and a Ga flux Φ_{Ga} = 4.5 nm/min. During the growth of the n-GaN layer, the substrate temperature was maintained at T_{sub} = 740 ^{o}C calibrated with a pyrometer for the Si (111) transition. It is to be noted that the growth was initiated only after the background chamber pressure stabilized following the striking of plasma as was the case with QD LED growth. The n-GaN growth layer was followed by the growth of the calibrated 700 nm thick n-$Al_{0.07}Ga_{0.93}N$ layer at T_{sub} = 740 ^{o}C and at Φ_{III} = 4.8 nm/min with Φ_{Al}/Φ_{Al+Ga} = 0.1. The RHEED pattern remained bright and streaky during the whole growth of this layer as well as the buffer GaN layer. The surface morphology during the growth of these layers needed close in-situ monitoring through RHEED patterns. If the RHEED pattern starts becoming spotty or the long streaky patterns start getting broken, the group III flux is increased slightly to maintain metallic bi-layer during AlGaN growth as the growth in MBE is kinetically driven [74]. An undoped $In_{0.03}Ga_{0.97}N$ layer is grown on top of the cladding layer from the optimized growth conditions derived in section 5.2.3. This was followed by an increase in the N_2 plasma flow rate and power to 0.7 sccm and 380 W, respectively before the growth of InGaN/GaN self-assmbled QDs which form under N-rich conditions. The optimized growth conditions of the InGaN/GaN QDs, as reported in

chapter 2, were then used to form eight pairs of the active region. The QD growth conditions were changed by varying the composition of In:Ga fluxes and substrate temperatures to obtain emission across various wavelengths. Typically, blue emitting QDs were grown at ~T_{sub}=565 ^oC and Φ_{In}: Φ_{Ga} = 2:1. Longer wavelength green emissions were generally obtained by lowering the growth temperatures to ~T_{sub}=545 ^oC and Φ_{In}: Φ_{Ga} = 3:2. The optimized growth conditions obtained as shown in chapter 2 were slightly altered to maximize PL intensity from the QD active region grown on top of a "half laser structure" containing AlGaN cladding, InGaN waveguide and uncapped dots on top. The heterostructure, AFM, PL and XRD of the optimized half laser stucture after a series of growth calibrations are shown in Figs. 5.5 (a), (b), (c) and (d) respectively.

Eight layers of capped InGaN/GaN QDs were followed by stabilization of the plasma back at 0.5 sccm and 300 W for growth of successive layers. A 5 nm thin layer of GaN layer was grown at T_{sub}=740 ^oC which further aided in recreating a smooth surface morphology and an accompanied streaky RHEED pattern before initiating the growth of p-doped layers. A heavily Mg-doped (p ~ 8x10^{17} cm^{-3}) optimized $Al_{0.15}Ga_{0.85}N$ 13 nm electron blocking layer (EBL) was grown at T_{sub}=740 ^oC to improve device performance by preventing electron leakage at high injections as outlined in chapter 3. A moderately (compensation) doped 150 nm p-$In_{0.03}Ga_{0.07}N$ waveguide (p~1x10^{17} cm^{-3}) was grown followed by a thick 700 nm highly doped p-$Al_{0.07}Ga_{0.93}N$ cladding (p~7x10^{17} cm^{-3}) layer. The final Mg-doped p-GaN (p~7x10^{17} cm^{-3}) layer was grown 150 nm thick followed by a 5 nm thick p^+-GaN region for improved ohmic contact formation. It should be noted that the p-GaN layers were grown with different Mg fluxes at T_{sub}=710 ^oC for

sufficient Mg incorporation under Ga-rich (Φ_{Ga}=5nm/min) conditions in presence of In as surfactant to maintain continuously smooth surface morphologies during heavy Mg incorporation.

5.3 Fabrication of Ridge Waveguide Quantum Dot Lasers

5.3.1 Processing of Ridge Geometry Waveguide Heterostructure

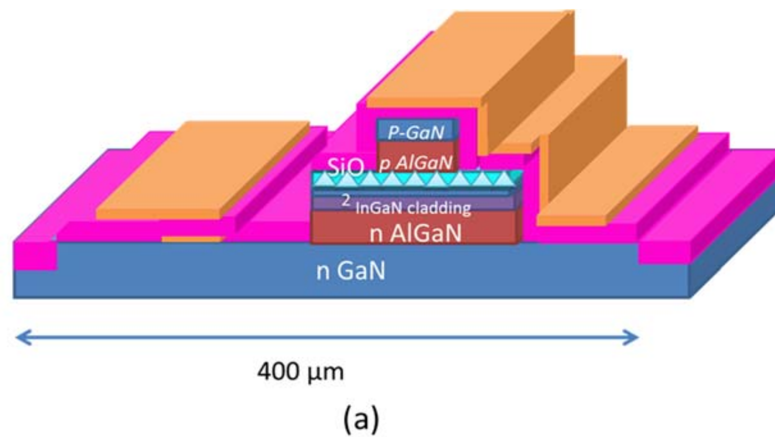

(a)

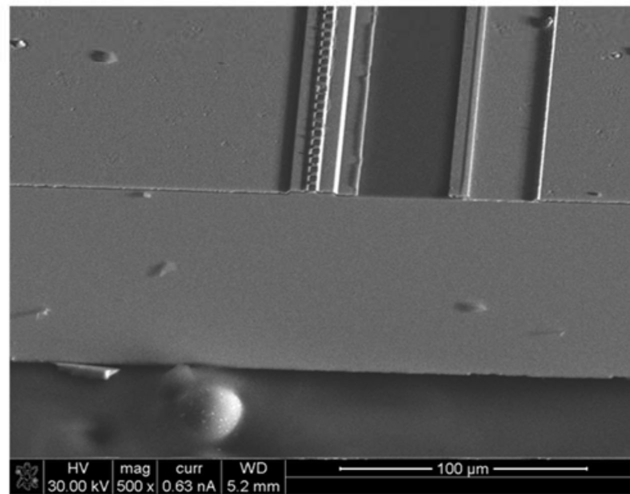

(b)

Fig. 5.6(a) Schematic of a fabricated laser heterostructure showing all the layers and (b) an SEM image of the laser heterostructure showing the fabricated laser heterostructure along with the cleaved mirror facet.

A typical fabricated laser schematic is shown in Fig. 5.6(a). The scanning electron microscopy (SEM) image of a fabricated laser heterostructure is also shown in Fig. 5.6(b). Projection photolithography (GSA Autostepper) was used to make all the patterns in the laser heterostructure. The first step involved making an alignment mark (Ti/Au metal deposition) parallel to the m-plane of GaN on c-plane for subsequent alignment of the laser bars perpendicular to the m-plane so that cleaved facet mirrors could be formed after the fabrication. 2 to 5 μm ridges were etched down to the upper cladding layer-waveguide heterointerface through reactive ion etching (RIE) (LAM 9400) after a careful calibration of the etch rate. This was followed by an etch down to the n-GaN by creating a 20 μm wide mesa pattern on top of the ridge geometry symmetrically reaching out on either sides to maximize the optical confinement factor. Care was taken to clean the residue after the RIE etching using O_2 plasma ashing. The next step involved metallization for ohmic p-contacts. A thin layer of native gallium oxide can prevent good ohmic contact formation. After developing an opening slightly smaller than the ridge waveguide on top of the mesa, the native oxide was removed by wet chemical etching in HCl:H_2O (1:1) for 10 minutes before quickly loading in the e-beam evaporator chamber to prevent new oxide formation. A 5 nm Ni/ 300 nm Au ohmic p-metal contact was deposited through metal lift-off. This was followed by annealing the p-contacts at 550 ^oC in a rapid thermal annealing (RTA) tool to create a Ni-O at the interface providing for good ohmic contacts. An 800 nm thick passivating SiO_x layer was deposited by plasma enhanced chemical vapor deposition (GSI PECVD) across the whole sample. Via openings were patterned and etched (using RIE) on top of the p-contact as well on top of the n-GaN followed by depositing thick 25 nm Ti/300 nm Au metal serving as n-contact

and p-contact interconnect separated from each other by passivating SiO_x layer as shown in the schematic in Fig. 5.6.

5.3.2 Cleaved facet mirrors for longitudinal confinement

GaN is a mechanically hard and stable semiconductor and cleaving of GaN to ~500

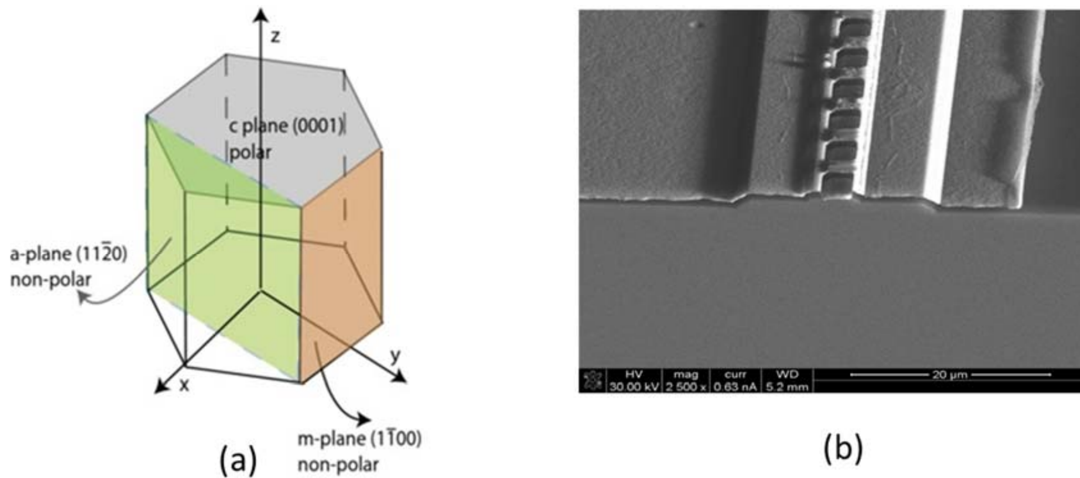

Fig. 5.7(a) Crystal structure of GaN showing the different planes of the crystal along c-plane, m-plane and a-plane and (b) an SEM image of the laser heterostructure showing the smooth cleaved mirror facet along the a-plane.

μm to 1mm bars can only be attained after thinning of the substrate. The backside of the GaN substrate used for laser growth was etched out and the sample thinned down to ~80 – 100 μm in final thickness. Figure 5.7(a) shows the crystal structure of GaN and the favored direction of cleaving along a-plane which is perpendicular to both m-plane and the c-plane, the preferred direction of growth. After putting scribe marks aligned parallel to the m-plane, cleaved mirror facets as shown in Fig. 5.7(b) were obtained with smooth facets by first thinning the sample to ~80 μm, followed by cleaving along a-plane. However, due to the low refractive index of the GaN, the highest reflectivity that can be obtained from cleaved facet is ~18% which is very low, especially compared with GaAs based diode lasers (R~32%). An additional multiple layers of calibrated SiO_2/TiO_2 DBR

are deposited on the facets to improve their reflectivity. Five layers were deposited on one end of the cavity which provided ~99% reflectivity while the other end had three layers deposited with for a reflectivity of ~80% from which side the laser output is measured.

5.4 Characteristics of Blue-Emitting InGaN/GaN Quantum Dot Lasers

The laser heterostructures were grown with optimized QDs emitting at various wavelengths inserted into the active region. Unless otherwise mentioned, all the laser heterostructures have similar cladding and waveguide layers except for the QD active region which is optimized to emit at different wavelengths. Optical output characteristics were measured for QD lasers demonstrating low threshold current density under both pulsed and continuous wave operation. QD lasers with GaN cladding layers were also made and some of their properties measured and compared to conventional QD lasers. Additionally, internal material parameters and differential gain were measured in these devices.

5.4.1 Output-current and spectral characteristics

Light-current (L-I) characteristics of blue QD lasers (λ=418 nm) were measured under pulsed (5% duty cycle, 1 μs pulse width) and CW bias at or close to room temperature. L-I characteristics for a device with 2 μm ridge width and 1 mm cavity length are shown in Figs. 5.8(a) and (b), respectively. The threshold current density measured for both pulsed and CW bias are J_{th} = 930 and 970 A/cm^2, respectively. These values are significantly lower than those measured in nitride-based quantum well visible lasers [118]. The slope efficiency, differential quantum efficiency, η_d, and power

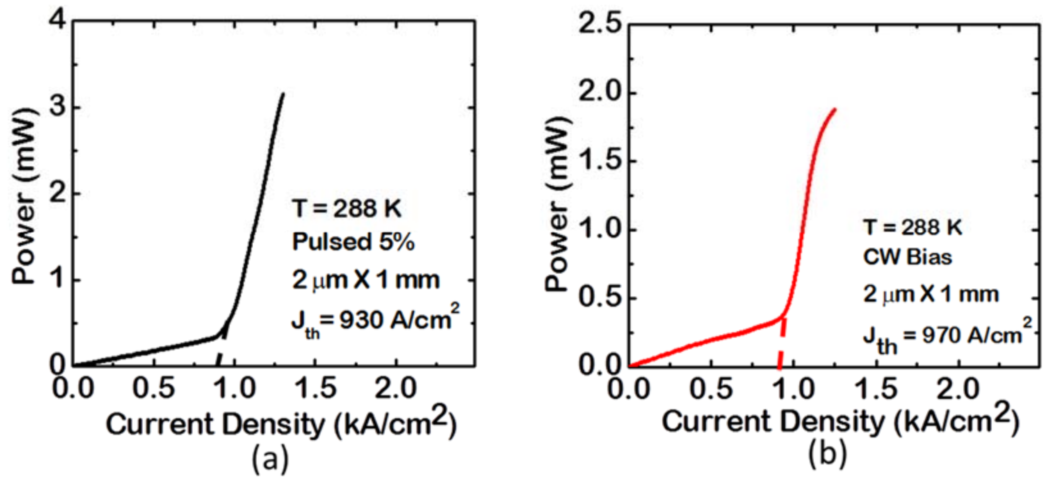

Fig. 5.8. Light output versus current (L-I) characteristics of blue-emitting QD lasers under (a) 5% pulsed and (b) continuous wave (CW) mode operation.

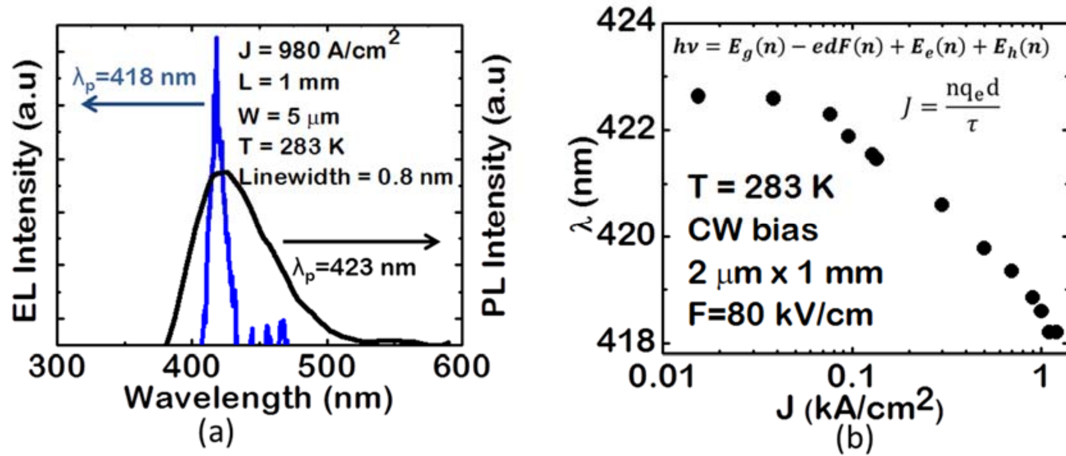

Fig. 5.9(a) Electroluminescence spectra of the laser with the spontaneous recombination from PL shown alongside and (b) peak emission wavelength shift with increasing injection for the laser.

conversion (wall plug) efficiency for CW operation are 0.41 W/A, 13.9% and 0.4% at 1050 A/cm^2. Figure 5.9(a) shows the laser emission spectrum (λ_{peak} = 418 nm) in comparison with the spontaneous emission (PL) spectrum with $In_{0.18}Ga_{0.82}N$ QDs. Figure 5.9(b) shows the measured blue shift of the peak laser emission wavelength with increasing injection current density. The shift occurs due to the screening of the

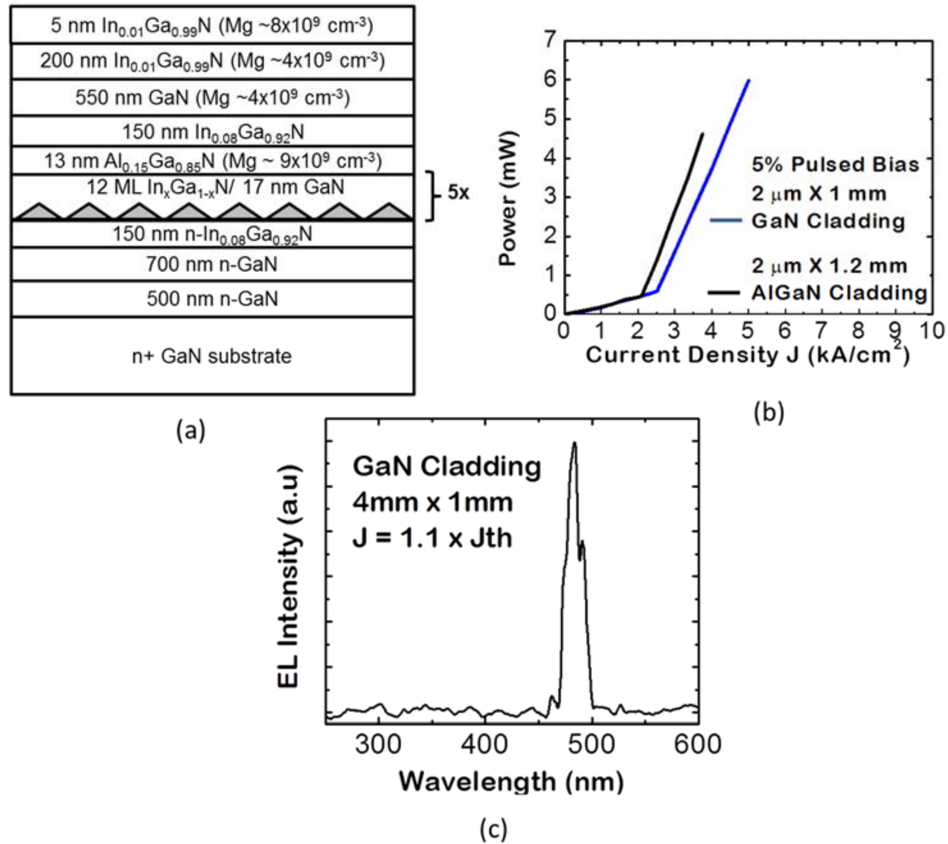

Fig. 5.10(a) Schematic of the laser heterostructure using GaN cladding and a higher In composition InGaN waveguide, (b) light output versus current (L-I) characteristics for a conventional laser heterostructure (Fig. 5.1(a)) and a GaN-clad laser heterostructure (Fig. 5.10(a)), and (c) lasing peak emission for the GaN-clad laser heterostructure.

piezoelectric field in the dots by the injected free carriers. The measured blue shift is only ~4.4 nm, which is an order of magnitude smaller than that measured in comparable InGaN/GaN quantum well devices [77, 78]. It may also be noted that there is no change of emission wavelength beyond threshold, which is a desirable attribute. A piezoelectric field of 80kV/cm in the InGaN QDs is estimated from the measured wavelength shift, compared to a value ~ 2.1 MV/cm reported for equivalent InGaN/GaN quantum wells [119].

After optimizing the growth conditions of the InGaN QDs, longer wavelength

blue (λ=479)-emitting laser heterostructures were also grown on free-standing c-plane GaN substrates. In addition to the heterostructure with $In_{0.02}Ga_{0.98}N$ waveguide and $Al_{0.07}Ga_{0.93}N$ cladding similar to conventional heterostructure shown in Fig. 5.1(a), device heterostructures with $In_{0.08}Ga_{0.92}N$ waveguides and GaN cladding layers were also grown as shown in Fig. 5.10(a). The calculated mode confinement factors of the two designs are 0.07 (almost same as for heterostructure shown in Fig. 5.1(a)) and 0.064, respectively. The device with the GaN cladding is expected to have a lower series resistance, and a lower operating voltage [120]. Additionally, the reduced mismatch strain is expected to result in more uniform QDs. The InGaN, GaN, and AlGaN layers were grown at 590°, 740°, and 760°C, respectively, and the QDs were grown at ~540°C for longer wavelength blue emitting dots (λ=479nm). The 13 nm thick p-$Al_{0.15}Ga_{0.85}N$ (p=6x10^{17} cm^{-3}) layer was grown at 750°C. The p- and n-doping levels in the cladding layers are ~(7-10)x10^{17} cm^{-3}. Light-current characteristics for the lasers were measured under quasi-CW bias (5% duty cycle, 50 μs pulse width) at room temperature. Data for blue-emitting devices with the AlGaN and GaN cladding, with a 2 μm ridge width and 1.2 mm cavity are shown in Fig. 5.10(b). The threshold current densities are 1.8 and 2.3 kA/cm^2, respectively, for the AlGaN and GaN cladding. These values are significantly lower than those reported for nitride based quantum well lasers with similar AlGaN [77] and GaN [120] cladding layers. The slope efficiency, differential quantum efficiency, η_d, and power conversion (wall plug) efficiency for pulsed operation are 0.11 W/A, 4.3% and 0.3% for the blue lasers with GaN cladding, and 0.12 W/A, 4.7%, and 0.3% for the blue lasers with AlGaN cladding, respectively. Due to the increased modal gain from the increased optical confinement, the lasers with AlGaN cladding have a lower threshold

current density in devices with comparable dimensions. Additionally, the reduced optical mode overlap with the (doped) cladding results in a reduced cavity loss and higher slope efficiency. However, the voltage drop is smaller in the GaN cladded devices resulting in similar wall plug efficiencies. The peak emission of lasing is shown in Fig. 5.10(c).

5.4.2 Measurement of differential gain

The threshold current and other dynamic characteristics of a laser are ultimately determined by the differential gain, dg/dn, and hence it is important to measure this parameter. It is obtained from cavity-length dependent L-I measurements. L-I measurements have been made on blue QD lasers (λ=418 nm) of different cavity lengths ranging from 0.6 to 1.6 mm. Figure 5.11(a) shows the variation of η_d^{-1} with cavity length.

$$\frac{1}{\eta_d} = \frac{\gamma}{\eta_i ln\left(1/\sqrt{R_1 R_2}\right)} L + \frac{1}{\eta_i} \qquad (5.1)$$

where η_d is the differential quantum efficiency, Υ is the cavity loss, R_1, R_2 are the reflectvities on the two ends of the longitudinal cavity and η_i is the internal quantum efficiency. From analysis of this plot (solid line) using the previous equation, we obtain a value of η_i = 68% and cavity loss γ = 11 cm^{-1}. This value of η_i is in reasonably good agreement with the value obtained from PL measurements. The variation of the measured J_{th} with inverse cavity length, shown in Fig. 5.11(b), is analyzed using the relation:

$$J_{th} = J_{th}^0 + \frac{qd}{\Gamma \eta_i \tau_r \frac{dg}{dn}} \left[\gamma + \frac{1}{2l} ln\left(\frac{1}{R_1 R_2}\right)\right] \qquad (5.2)$$

where J_{th}^0 is the transparent current density, d is the total thickness of the active (gain) region, Γ is the confinement factor and ℓ is the cavity length. Using the measured values of η_i, τ_r and γ, and Γ = 0.03, calculated as the overlap of the waveguide mode power with the quantum dot layers with the dot fill factor of 0.44 included, a value of

dg/dn = $2x10^{-16}$ cm^2 is derived. The active region thickness, d, was calculated from an effective dot height of 3.5 nm, taking into account hexagonal dot geometry, wetting layer thickness and the fill factor. Calculated and measured values of dg/dn in InGaN/GaN and InGaN/AlGaN strained and strain-compensated quantum well lasers [121, 122] are an order of magnitude lower than the value quoted above for QDs. A value of differential gain (dg/dn) of $1.03x10^{-16}$ cm^{-2} is obtained for long wavelength lasers (λ ~479 nm). It is also instructive to compare dg/dn in the InGaN/GaN QDs with those measured for In(Ga)As/GaAs QD lasers, which are usually an order of magnitude higher [123, 124]. We believe this is a result of the large carrier effective masses and joint density of states in the InGaN/GaN QDs. As a result, the threshold current in InGaN/GaN QD lasers may not reach the low values of J_{th} reported for In(Ga)As/GaAs QD lasers [125].

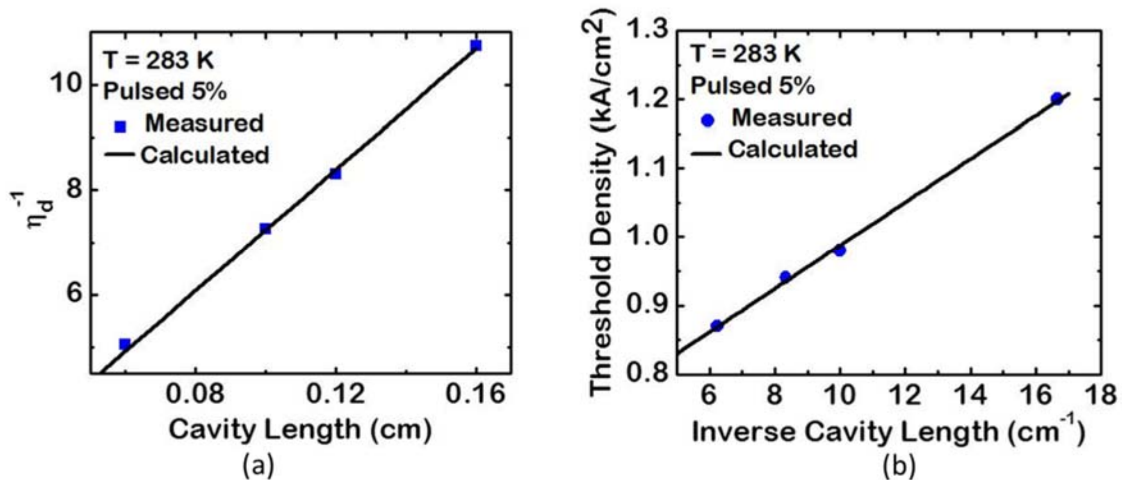

Fig. 5.11(a) Cavity length dependence of inverse differential quantum efficiency and (b) variation of threshold current density with inverse cavity length.

5.4.3 Polarization output and near field characteristics

The output of the lasers emitting at λ=418 nm was probed by measuring the polarization of the light. Figure 5.12 shows the output intensity polarized in the

transverse electric (TE) and transverse magnetic (TM) modes as a function of injection

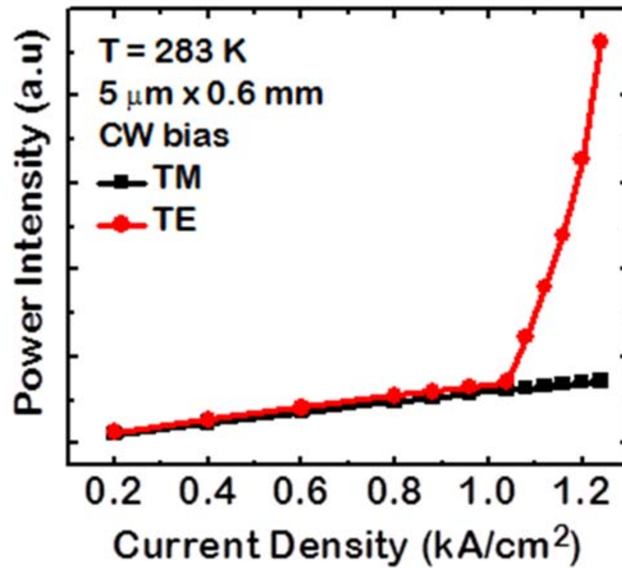

Fig. 5.12. Laser output polarization as a function of injection current density.

current in a 5 μm ridge device with 0.6 mm cavity length. A clear threshold is observed for the TE-polarized output. This is because the TE mode has higher gain above threshold. Additionally, the TE mode is better confined, resulting in a higher optical confinement factor and reduced loss associated with the overlap of the optical mode with doped cladding regions.

A near field image from a 4 μm wide ridge waveguide laser, with a cavity length of 1.2 mm, is shown as a contour plot in Fig. 5.13(a). The measured mode profile in the growth (transverse) direction, intersecting the maximum of the mode, is shown in Fig. 5.13(b), with the mode in the perpendicular (lateral) direction (along the width of the ridge) shown in Fig. 5.13(c). In the growth direction, the relatively narrow thickness allows for a (nearly) single mode output, while the mode in the transverse direction

clearly consists of several higher order modes, as expected in such a relatively wide waveguide. An index guided single mode laser will have to be fabricated with a smaller ridge width and deeper etch, or by utilizing the buried stripe geometry.

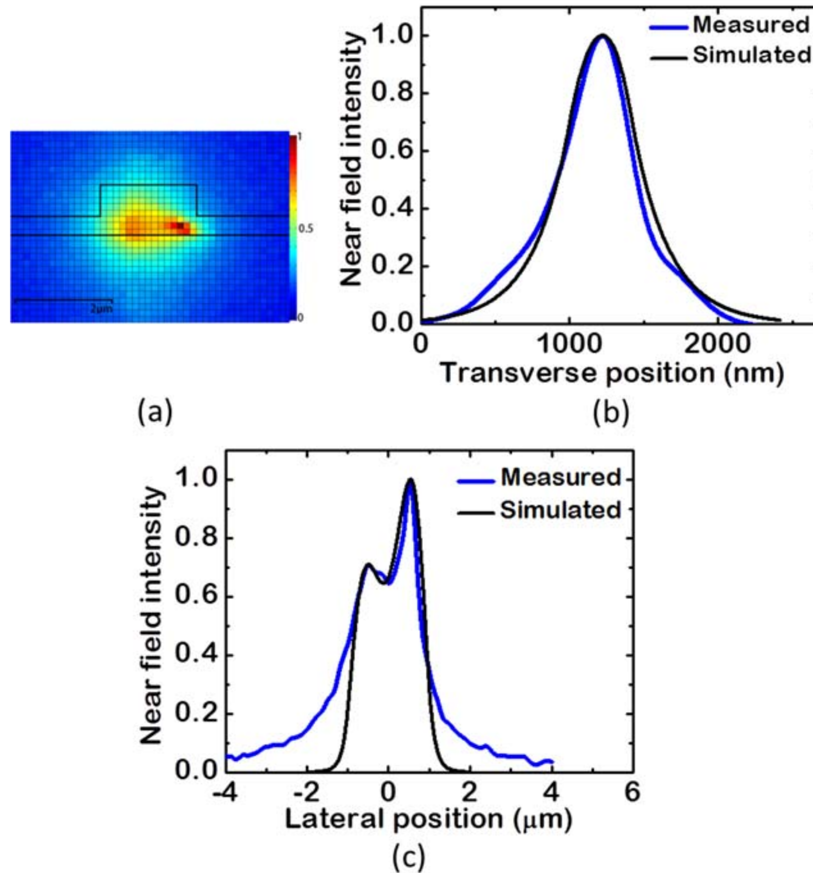

Fig. 5.13(a) Contour plot of the near field image of the laser mode. Laser mode profile in the transverse (b) and longitudinal (c) directions, as compared with the mode profiles simulated by transfer matrix method.

5.5 Characteristics of Red-Emitting (λ=630 nm) InGaN/GaN Quantum Dot Lasers

Lasers emitting in the 600 nm wavelength range are finding large scale applications in optical information processing, plastic fiber communication systems,

optical storage, and full color (RGB) laser displays and projectors [105, 106]. As discussed earlier, lasing at longer wavelengths is difficult to achieve using InGaN/GaN quantum wells (QWs) in the active region mainly due to the large polarization field and In clustering effects which become more significant with high In composition the InGaN

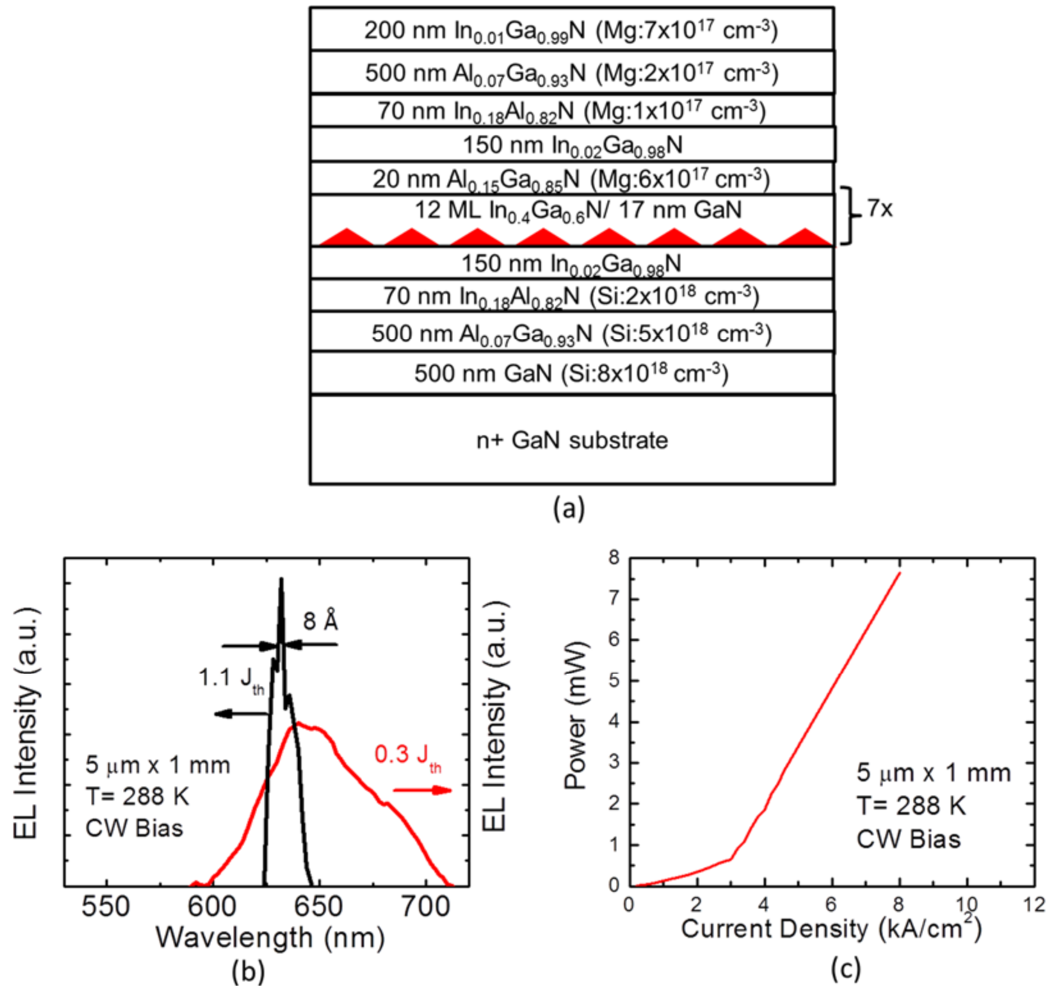

Fig. 5.14(a) Schematic of red $In_{0.4}Ga_{0.6}N$/GaN QD laser, (b) spectral output from a single facet of the laser under continuous wave bias below and above threshold, and (c) light-current characteristics of the laser from a single facet.

QW. Additionally, the threshold density of such QW lasers emitting at even green wavelengths is generally very large due to reduced electron-hole wavefunction overlap in the quantum wells. Lasing beyond green wavelengths has not been achieved from heterostructures incorporating InGaN/GaN QW active regions on c-plane or any non-

polar planes of GaN.

The first nitride-based red lasers were demonstrated incorporating InGaN/GaN quantum dots as the active region on c-plane GaN substrates. The conventional heterostructure was modified with the incorporation of lattice matched InAlN as the cladding layer to provide stronger optical mode confinement with reduced strain as shown in Fig. 5.14(a). The red lasers were characterized by a lasing peak at 630 nm (Fig. 5.14(b)) with a threshold current density of 2.5 kA/cm^2 (Fig. 5.14(c)). The threshold current density is even lower than those obtained for green-emitting nitride QW lasers. The output slope efficiency and the corresponding wallplug efficiency measured for a laser of cavity length equal to 600 μm is 0.05 W/A and 0.4% (measured at 200 mA and 7.8 V). Additionally, a peak emission shift of only 11.6 nm also confirms the weak polarization field present in the InGaN/GaN self-assembled QDs.

5.6 Summary

In conclusion, the characteristics of self-organized $In_{0.18}Ga_{0.82}N$/GaN QD ridge waveguide lasers emitting in the blue (λ = 418 nm) and longer wavelengths $In_{0.27}Ga_{0.73}N$/GaN QD (λ = 479 nm) lasers have been measured. The devices have been operated under pulsed and CW bias conditions. A threshold current of 930 A/cm^2 is measured in a 2 μm ridge laser at 288 K under pulsed bias for the shorter wavelengths. The blue shift due to screening of the piezoelectric field in the dots is 4.4 nm. Longer wavelength lasers emitting at λ = 479 nm were characterized with different cladding layers and threshold current density as low as 1.8 kA/cm^2 were recorded. While the performance of the lasers, in terms of J_{th}, efficiencies and dg/dn, are extremely encouraging, there is considerable room for improvement before the full potential of

using QDs in the active region can be realized. The internal quantum efficiency of the blue dots is $\eta_i \sim 60\%$. While this value is larger than any other reported previously and was achieved after optimizing the growth conditions, it has to be increased further to improve laser performance. We believe that the main reason for the low value of η_i is the large defect density ($5x10^6$ cm^{-2}) in our starting GaN substrate. The value of η_i should be considerably larger with growth on substrates having a defect density $\sim 10^4$ cm^{-2}. Concurrently, the value of J_{th} is expected to be lower and higher output powers can be obtained. The first nitride-based red-emitting lasers were demonstrated incorporating InGaN/GaN QDs in the active region and InAlN in the cladding region. This is the longest emission wavelength achieved with nitride-based heterostructures. The preliminary output characteristics at such long wavelengths demonstrate the ability of the QDs in producing the best lasers at λ=630 nm and possibly at even longer wavelengths.

Chapter VI

Optical and Spin Properties of Carriers in InGaN Dots in GaN Nanowires Grown on Silicon

6.1 Introduction

The lack of a high-quality and low-cost GaN substrate necessitates the nucleation of GaN on sapphire (or silicon) which have large lattice mismatches of 13.8% (or 18%) resulting in a large dislocation density directly or indirectly affecting device performance. Recently, nanowires have been successfully grown by molecular beam epitaxy (MBE) [126-128] and metal organic chemical vapor deposition (MOCVD) [129-131]. In MBE, they grow by Ga self-catalysis mode vertically on (001) and (111) Si along the wurtzite c-axis. Structural and optical characterization revealed that the nanowires were relatively free of extended defects, stacking faults and twins [130-134] because of their large surface-to-volume ratio which provides for strain relaxation. A reduced strain distribution in the nanowires also leads to a weaker piezoelectric polarization field. InGaN disks of 2 nm thickness were inserted into such relatively defect-free GaN nanowires. The typical nanowire diameter in the growth plane was ~30 nm, so the InGaN insertions were ~2 nm x 30 nm. These are of similar dimensions to that of the self-assembled quantum dots (QDs) described earlier. It was seen from the measurements and theoretical calculations performed on self-assembled QDs that due to

quantum confinement and localization of carriers, along with weak polarization field, there is a strong electron-hole wavefunction overlap and superior optical properties [47-49]. The nanowires, by virtue of having similar dimensions of InGaN insertions compared to that of the self-assembled QDs and a large aspect ratio for strain relaxation, are also expected to provide superior optical properties over c-plane quantum wells (QWs). Additionally, the absence of a high defect density in GaN/sapphire or GaN/silicon substrates make the nanowires a highly desirable nitride material system for studying the optical properties and characterizing the devices made out of them.

This chapter discusses the growth and optical properties of the InGaN dots (or disks) in GaN nanowires. The dots emit across the whole visible spectrum. Carrier lifetimes were measured in the dots-in-nanowire heterostructures and a recombination model for the observed carrier decay times proposed. Additionally, spin properties of carriers in quantum confined InGaN dots in relatively defect-free GaN nanowires were measured and the fundamental spin scattering mechanism responsible for spin scattering in the nitride material system was determined.

6.2 Growth and Characterization of InGaN Dots in GaN Nanowires

6.2.1 Growth of InGaN/GaN dot-in-nanowire heterostructure

In(Ga)N nanowires can be grown on silicon substrates using a Ga self-catalyst [125, 136] with lengths up to a few micrometers, diameter varying in the range 30-80 nm and aerial densities in the range 10^8-10^{11} cm^{-2}. They grow vertical to the silicon surface in the wurtzite crystalline form with the c-axis parallel to the direction of growth. GaN nanowires with a density of 1x10^{11} cm^{-2} were grown on (001) n-Si substrate with

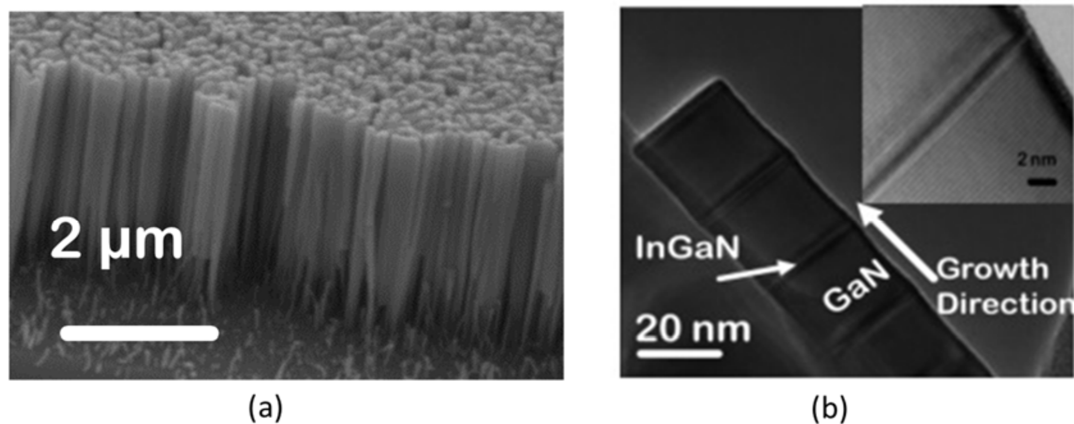

Fig. 6.1(a) High density GaN nanowires grown on (001) Si and (b) HR-TEM image showing a GaN nanowire with multiple InGaN/GaN dot-in-nanowire heterostructures. The high resolution cross-TEM image shown in the inset depicts a single dot-in-nanowire [135].

resistivity < 0.001 Ωcm in the MBE system described in previous chapters. The native surface oxide on the Si substrate was removed with a 900 °C anneal in the growth chamber for an hour after a BHF oxide etch. As was mentioned in previous chapters for 2-D GaN bulk growth, the 1x1 to 7x7 transition in the RHEED patterns were observed for (111) Si to determine the actual temperature on the substrate and calibrate the pyrometer. After cleaning the oxide through in-situ annealing, the substrate temperature was lowered to 800 °C and a few monolayers of Ga were deposited with a Ga flux of $1.5x10^{-7}$ Torr in the absence of active nitrogen. GaN nanowire growth was initiated at the same substrate temperature under N_2-rich conditions by introducing the active nitrogen species. The growth rate of the nanowires was ~300 nm/h. The Ga flux was maintained at $1.5x10^{-7}$ Torr and the N flow rate held constant at 1 sccm. InGaN and GaN layers were grown alternatively to form nanowires containing InGaN/GaN dots (or, disks) in GaN nanowire heterostructures. The InGaN quantum dots were grown at constant Ga and In fluxes of $1x10^{-7}$ Torr and $1.5x10^{-7}$ Torr, respectively, while only the growth temperature

was varied from 500 to 580 °C for emission across the whole visible spectrum.

The structural properties of the nanowires were investigated by scanning electron microscopy (SEM) and high resolution transmission electron microscopy (HR-TEM) imaging. As shown in Fig. 6.1(a), high density ($1x10^{11}$ cm^{-2}) GaN nanowires were grown with diameters ranging from 10 to 50 nm (in different samples) and they exhibited excellent uniformity in length. The TEM image of Fig. 6.1(b) shows a GaN nanowire with a dot-in-nanowire heterostructure, where multiple layers of InGaN dots of 2 nm thickness were self-aligned along the nanowire growth direction. The image depicts a smooth and dislocation-free interface between InGaN and GaN. It is also known from selective area diffraction measurements that the nanowires grow in the wurtzite crystalline structure with the c-axis parallel to the direction of growth.

6.2.2 Photoluminescence of GaN nanowires

The optical properties of the nanowires were examined by photoluminescence (PL) measurements by exciting the samples with a frequency tripled output of a mode-locked Spectra Physics Tsunami Ti:Sapphire laser emitting at 267 nm and focusing the sample emission to a monochromator (with a spectral resolution of 0.03 nm) fit with a photomultiplier tube (PMT). The GaN nanowire PL at room temperature was found to be free of any deep level yellow bands indicating absence of any defect states related to Ga vacancies during crystal growth. Figure 6.2(a) shows a typical room temperature PL from a GaN nanowire grown on (111) Si. Clear excitonic peaks were observed from GaN nanowires at low temperatures originating from the bulk of the nanowire and the surface as shown in Fig. 6.2(b). This further indicates the crystalline quality of the GaN nanowires. The lifetimes of these excitonic peaks were measured and are discussed in the

next section.

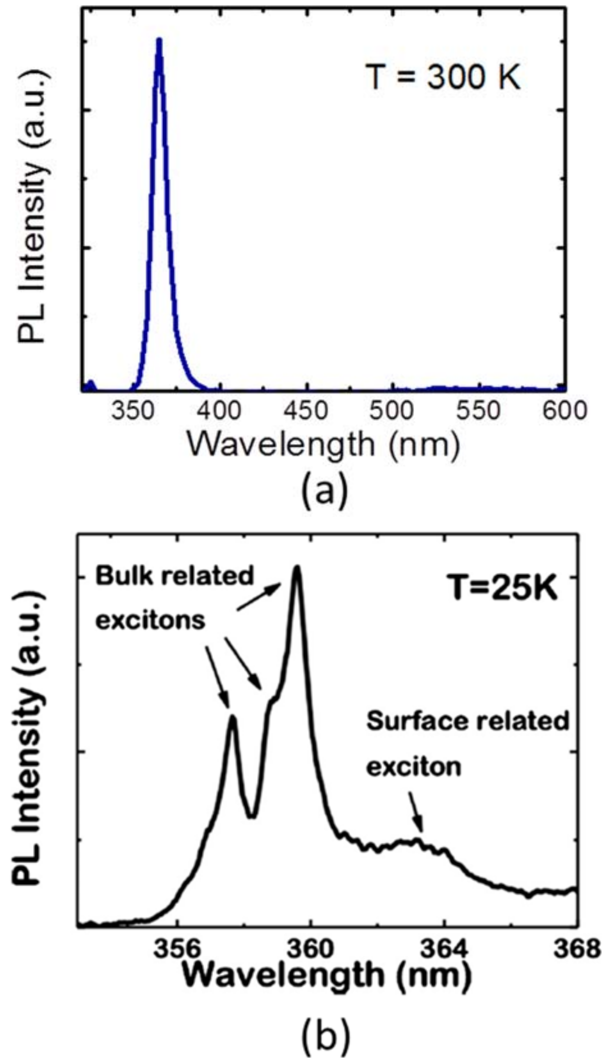

Fig. 6.2(a) Room temperature PL of GaN nanowire ensemble showing absence of yellow band and (b) PL spectra of a GaN nanowire sample measured at 25K showing three sharp bulk related excitons and a broad surface-related defect bound exciton.

6.2.3 Time-resolved photoluminescence of GaN nanowires and InGaN dots in GaN nanowires

Time-resolved photoluminescence (TRPL) measurements were performed at cryogenic temperatures with unpassivated and passivated nanowires at the peak emission

wavelength of the various excitonic transitions. It was found that the PL decay times of the three bulk related exciton transitions were almost constant at ~220 +/- 50 ps (Fig. 6.3(a)). This time constant reflects the intrinsic behavior of the bulk nanowires. On the other hand, the decay time constants of the surface related excitons were 572, 407, and 315 ps for the as-grown, SiN_x-passivated and parylene-passivated nanowires (Fig. 6.3(b)). Due to space-charge related surface depletion [136, 137], electrons and holes

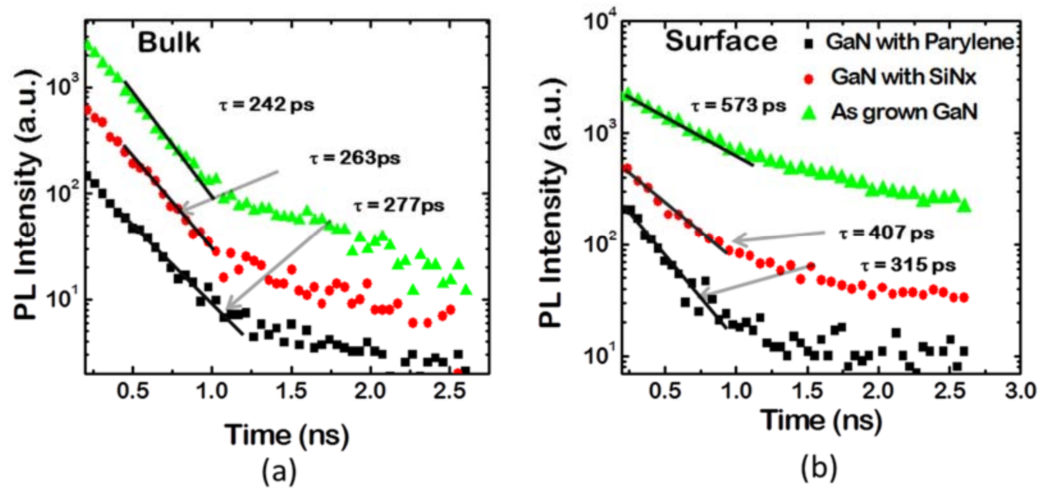

Fig. 6.3. PL decay transients obtained from TRPL on as-grown and passivated GaN nanowires for (a) bulk excitons which remain unchanged and (b) surface excitons which change with passivation.

could be spatially separated, leading to a longer recombination lifetime. With passivation, the surface state density and the extent of the depletion region would be reduced, thereby enhancing the electron-hole overlap and reducing the lifetime. It seems that with parylene passivation, the carrier lifetime approaches that of the free excitons in the bulk of the nanowires and surface recombination is reduced to a minimum. The study has been published elsewhere [126].

TRPL measurements on InGaN dots in GaN nanowires were performed and the carrier lifetimes analyzed. Figure 6.4(a) show the typical carrier decay times obtained for

InGaN dots emitting at 420 nm under resonant excitation. The bi-exponential temporal behavior was characterized by an initial fast decay of the PL, more pronounced at higher temperatures, followed by a transient with a longer time constant. The initial fast decay, with time constant τ_1, was attributed to thermally activated carrier relaxation to energetically lower localization minima caused by In composition fluctuation in the QD [67, 138]. The transient was not observed for the measurements at 480 nm possibly due to a stronger localization of carriers at the lower minima. The subsequent slower transient PL signal had a time constant τ_2 almost independent of temperature. It is believed that τ_2 is a measure of the recombination lifetime of carriers in the dots in nanowires. The results were modeled as described below.

The transient photoluminescence data was analyzed with a three level rate equation model in order to understand the carrier dynamics in the InGaN dots-in-nanowires. According to the model, near-resonant photoexcitation creates a population of carriers n_0 at a higher energy state, from which the majority of them undergo fast relaxation to the ground states of the dots, with a population n_1. A fraction of n_1 relaxes to deeper lying localized states. The carriers in these states, with population n_2, undergo efficient recombination. The relevant rate equations are:

$$\frac{dn_0}{dt} = -\frac{n_0}{\tau_g} \qquad 6.1$$

$$\frac{dn_1}{dt} = \frac{n_0}{\tau_g} - \frac{n_1}{\tau_{r1}} - \frac{n_1}{\tau_{cap}} - \frac{n_1}{\tau_{nr1}} \qquad 6.2$$

$$\frac{dn_2}{dt} = \frac{n_1}{\tau_{cap}} - \frac{n_2}{\tau_{r2}} - \frac{n_2}{\tau_{nr2}} \qquad 6.3$$

and the different lifetimes are indicated in the inset of Fig. 6.4(b) below. The model enables good fits to the measured data of all three samples and at all wavelengths for

temperature ranging from 20 –300 K. The values of τ_1 and τ_2 obtained from analysis of the data of Fig. 6.4(a) in the text and are shown in Fig. 6.4 (b). Here

$$\frac{1}{\tau_1} = \frac{1}{\tau_{r1}} + \frac{1}{\tau_{cap}} + \frac{1}{\tau_{nr1}} \quad 6.4$$

$$\frac{1}{\tau_2} = \frac{1}{\tau_{r2}} + \frac{1}{\tau_{nr2}} \quad 6.5$$

The transient data measured in dots-in-nanowires was analyzed according to the model described above. The average value of τ_2 obtained from the rate equation analysis is ~0.6 ns, which is in good agreement with previously measured data from similar dots [49].

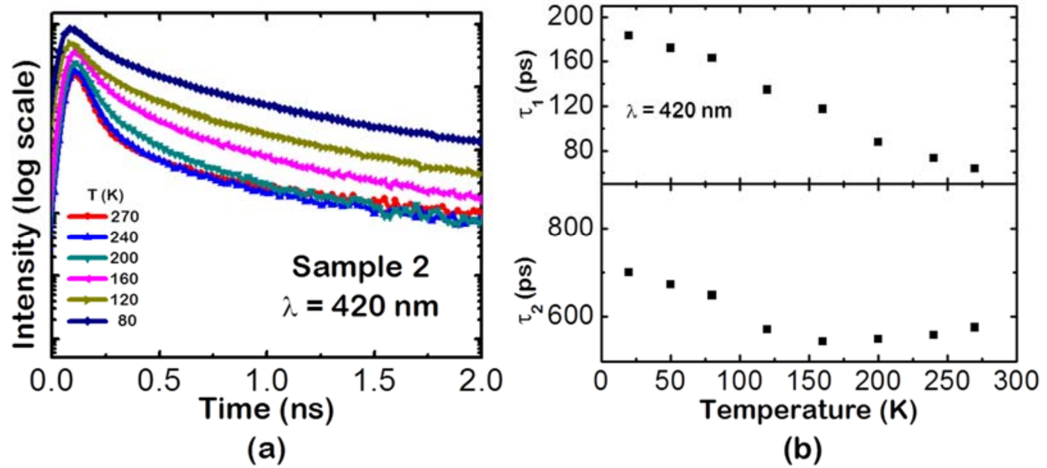

Fig. 6.4(a) Carrier decay time for InGaN dot in GaN nanowire measured at λ=420 nm and at different temperatures and (b) value of τ_1 and τ_2 obtained from rate equation analysis of measured data from (a).

6.3 Properties of Spin Polarized Carriers in InGaN Dots in GaN Nanowires

6.3.1 Introduction

Spin-related phenomena in semiconductors are investigated to gain fundamental understanding of the injection, control, transport and detection of carrier spins. While such phenomena have been widely investigated in Si and GaAs-based materials and

heterostructures [139], much less is known of the spin related properties of GaN and related compounds [140-142]. What makes these materials attractive for future spintronics applications is the weak spin-orbit coupling (SOC) and the associated possibility of long spin relaxation times, even at room temperature. The SOC is a strong function of the average atomic number of the constituent atoms, and as such, is relatively low for GaN. The measurements were performed on InGaN dots in GaN nanowires as the increased quantum confinement is expected to enhance spin relaxation times. Additionally, the low polarization field and relatively-defect free environment due to the large aspect ratio would help in determining the dominant spin scattering mechanism independent of defect-related effects. The work reported in the subsequent sections has been published by the author elsewhere [143].

Nitride based semiconductors are usually grown in the polar wurtzite crystalline form and therefore have inversion asymmetry, which causes a spin splitting of the bands via spin-orbit coupling. The spin polarized carriers undergo spin precession about the resultant effective magnetic field which is the basis of the D'yakonov-Perel' (DP) spin relaxation mechanism [141]. Every momentum scattering event randomizes the effective magnetic field direction and thereby the spin relaxation is impeded. It has been shown that in GaN, the DP spin relaxation is anisotropic [144], which is a direct consequence of the anisotropic SOC in wurtzite structures. Elliot-Yafet (EY) spin scattering mechanism is associated with a momentum scattering event that a spin polarized carrier encounters. It becomes imperative, therefore, to measure the spin relaxation times in these relatively defect-free nitride nanowires to determine the fundamental spin scattering mechanism in these systems. The other spin scattering Bir-Aronov-Pikus (BAP) mechanism is generally

caused by the fluctuations in electron-hole exchange interaction in p-doped semiconductors and is not relevant here. All the experiments that have been performed before were conducted with nitride semiconductors grown on highly mismatched sapphire or silicon substrates with high defect densities of ~ 10^8-10^9 cm^{-2}. In the subsequent sections in the chapter, the measured and theoretically analyzed spin relaxation times of optically excited spin-polarized carriers in InGaN/ GaN quantum dots in GaN nanowires grown on (001) silicon substrates are reported. It was found that the relaxation times vary in the range of 80-140 ps with a weak temperature dependence. The results revealed that DP scattering was the dominant spin relaxation mechanism as described in details in section 6.3.4.

6.3.2 Optical injection and detection of spin polarized carriers

The schematics of the heterostructure used for measurement of spin polarized carriers in InGaN dots in GaN nanowires are shown in Fig. 6.5(a). After the initial growth of 400nm of GaN nanowire at 800°C, the growth temperature was lowered to 580°C and multiple periods of $In_xGa_{1-x}N$ (2nm)/GaN (20nm) quantum dots were grown. The composition x in the dots was varied in the range 0.12-0.25 in different samples. The entire heterostructure was undoped. Scanning electron microscopy (SEM) and TEM imaging indicated that the aerial density is ~$1x10^{11}cm^{-2}$ and the diameter of the individual nanowires were ~30nm. The quantum disks (or dots) therefore had dimensions of ~2nm x 30nm as was mentioned before.

The wurtzite structure of GaN leads to a valence bandstructure consisting of the A (HH), B (LH) and C (SO) states [145, 146], of which the A and B states are energetically very close (separation ~ 15 meV in $In_{0.2}Ga_{0.8}N$) as shown in Fig. 6.5(b). The oscillator

strength of optical transitions between the conduction band and A and B states of the valence band are very comparable (~ 1:0.94) [145] as against GaAs bandstructure where it is 3:1. As a result, photoexcitation with non-resonant circularly polarized light results in almost zero spin polarization.

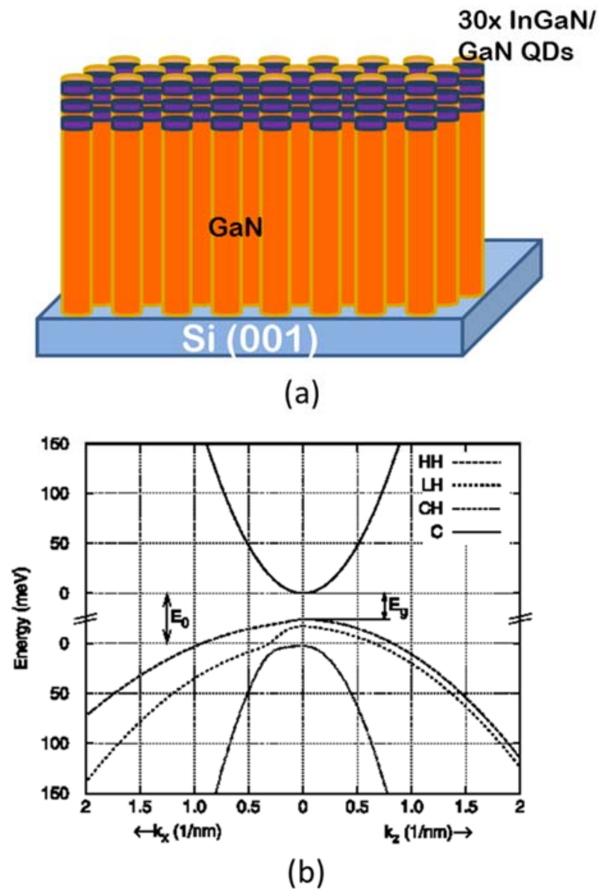

Fig. 6.5(a) Schematic of InGaN dots in GaN nanowire heterostructure used for spin measurements and (b) anisotropic band diagram of GaN showing very low separaction of HH and LH bands [147].

The incident optical excitation for photoluminescence (PL) and time-resolved PL (TRPL) measurements was provided by the frequency-doubled output of a pulsed 80MHz mode-locked Ti:sapphire laser tuned to a wavelength larger than that corresponding to the bandgap of GaN and very close to the InGaN peak emission in order to resonantly excite

the valence band A states-to-conduction band transition in the InGaN dots. The excitation was incident at 20° to the sample normal and the luminescence was collected in the direction normal to the sample and along the c-axis. The luminescence was analyzed by a monochromator (resolution ~0.03 nm) and subsequently focused on to a single photon detector (measured system response time ~ 50 ps). For spin lifetime measurements the incident resonant excitation was circularly polarized and this produced spin-polarized carriers in the InGaN dots where the light was absorbed. These carriers

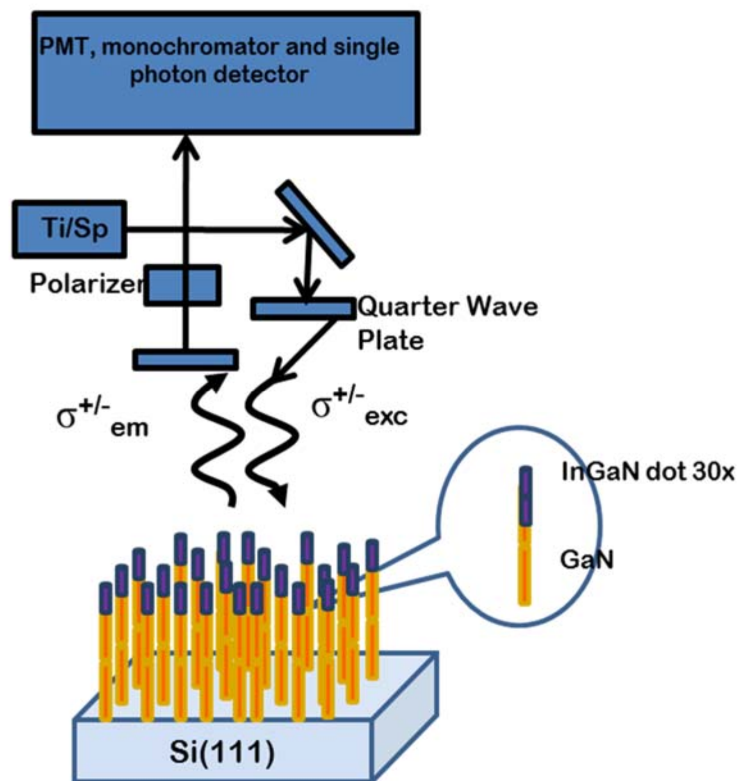

Fig. 6.6. Schematics of the measurement set-up for optical injection and detection of spin properties.

recombined to produce polarized light, which was resolved into the left- and right-circularly polarized components. Temperature dependent measurements were performed by mounting the sample in a continuous flow liquid He cryostat. The measurement set-up

used is shown in Fig. 6.6. The 80 MHz mode-locked light output of the Ti:sapphire laser is linearly polarized (TE). It was converted to circularly polarized light by passing it through a quarter-wave plate (λ/4) before exciting the InGaN dots resonantly and fine-tuning the excitation wavelength till polarized PL emission was observed. Circularly polarized light when absorbed by the InGaN dots with increased splitting of the A and B states (due to strain) such that only CB-A transitions are possible and CB-B transitions are at higher energy than excitation energy, created selective excitation of spin polarized carriers. They undergo spin flip through DP and EY spin scattering mechanisms. The intensity of luminescence emitted by the recombination of spin polarized carriers with unpolarized holes is circularly polarized for a certain spin state of electrons. Thereby a measure of the difference in the intensity of right and left circularly polarized emitted light gives us a measure of the degree of spin polarization present in the InGaN dots in nanowires at that instant of time. The circularly polarized luminescence emitted from the sample was detected by converting it back to linearly polarized light using a quarter wave plate. The right and left circularly polarized light gave linearly polarized light polarized 90° apart from each other after passing through the quarter wave plate. Each component of the linearly polarized light was then selected using a linear polarizer and their intensities measured for PL and TRPL measurements.

6.3.3 Spin polarization lifetimes of electrons in InGaN dots in GaN nanowires

As outlined in the last section, the description of the four samples used in the measurements with the In composition x in the dots being 12, 20 and 25% are shown in table 6.1 [128]. These are being labeled samples 1, 2, 3 and 4 and the peak of the room temperature PL from these samples occurred at 407, 420, 450 and 453nm, respectively.

Sample	InGaN/GaN dot pairs	$\lambda_{emission, peak}$ (nm)
1	8	407
2	8	420
3	30	450
4	8	453

Table 6.1. Description of the samples used for measurement of spin lifetimes.

The excitation wavelength was set at 395 nm for selective excitation of CB-HH (A) states for sample 1. Polarization dependent photoluminescence spectra of sample 1 at T= 300 K, are shown in Fig. 6.7(a) and the data exhibit the polarized σ+ and σ - components. The inhomogenously broadened linewidth of the luminescence is caused by composition variation in the disk-like $In_xGa_{1-x}N$ dots. TRPL measurements were made at different wavelengths in the temperature range of 20-300 K. The measured data for sample 2 at 420 nm are shown in Fig. 6.7(b).

The rate of change of polarization calculated from the carrier decay times for the two different polarized outputs is plotted in the inset to Fig. 6.7(b). It is evident that the polarization decay time is significantly smaller than the radiative lifetime of the spin polarized carriers as described using the model in section 6.2.3. The percentage degree of polarization, defined by P=100 (σ+ - σ-)/(σ+ + σ-) derived from the transient data is plotted in the inset. The polarization at time t=0 was small since the separation of the A and B valence band states in the InGaN dots is comparable to the width (in energy) of the excitation pulse and, as mentioned before, the probabilities of the optical transitions involving these states are comparable in the wurtzite structure. The spin relaxation time τ_s was obtained from the transient polarization data by fitting the latter with a single e

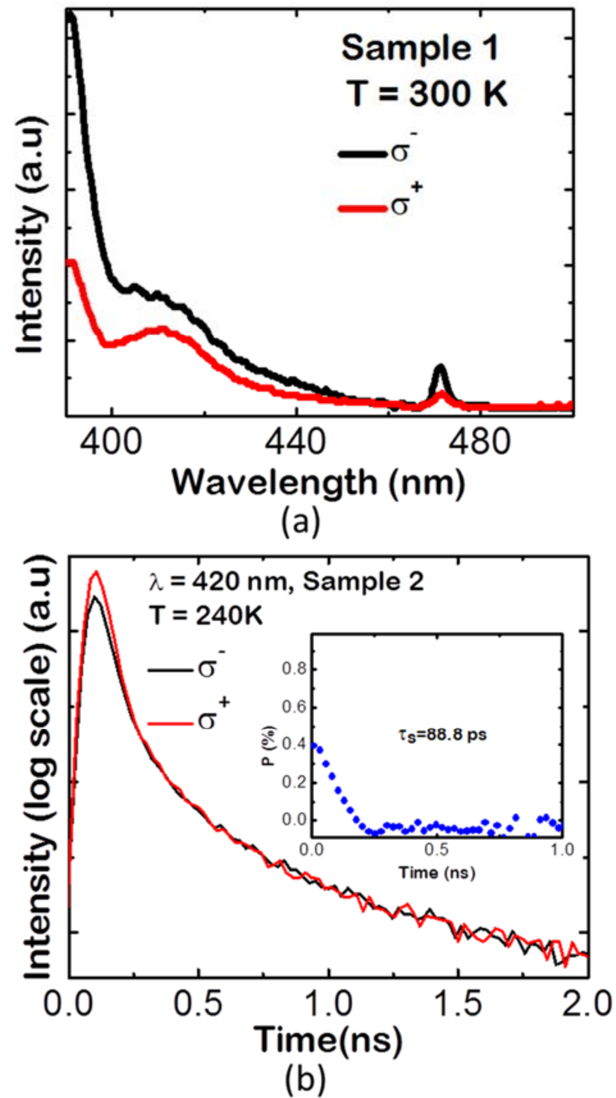

Fig. 6.7(a) Polarization dependent photoluminescence spectra of sample 1 at T = 300 K under resonant excitation (λ = 395 nm) and (b) spin polarized transient photoluminescence at T=240 K for sample 2 measured at λ=420 nm. Inset shows the temporal variation of the degree of polarization.

xponential: $P(t) = P(0) \exp(-2t/\tau s)$. The spin lifetimes measured as a function of temperature in sample 3 measured at λ=420, 450 and 480 nm are shown in Fig. 6.8(a). Similar data comparing the trends in samples 1, 2 and 4, are shown in Fig. 6.8(b). It is evident that spin relaxation times increase with increasing wavelength in the same

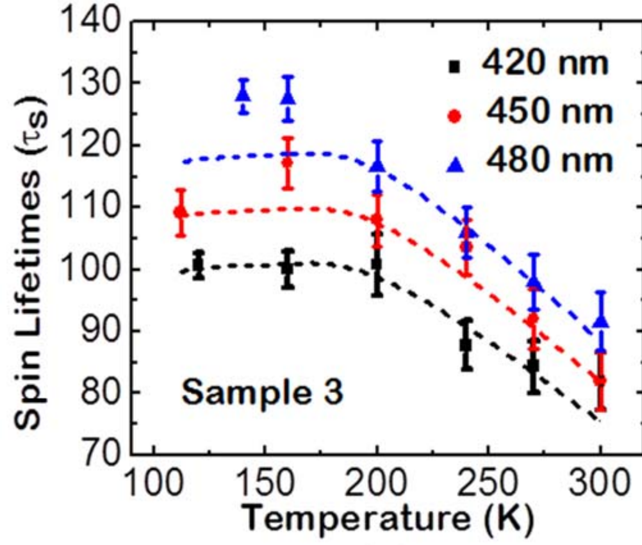

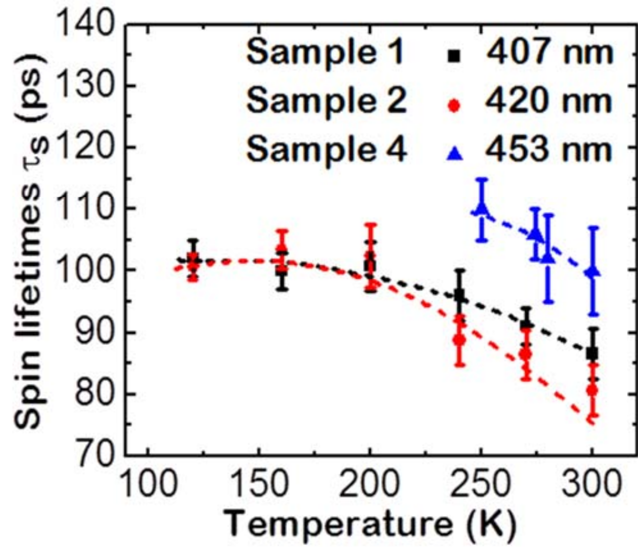

Fig. 6.8. Spin lifetimes as a function of temperature (a) in sample 3 at λ=420, 450 and 480 nm, (b) in samples 1, 2 and 4 measured at their peak wavelength (λ=407, 420 and 453 nm, respectively). The dashed lines are the theoretical spin lifetimes calculated as described in subsequent section.

sample 3, where the increasing wavelength represents a contribution from regions of higher In content in the InGaN dots. A similar trend was seen by directly varying the In composition in three different samples. Nagahara *et. al.* [148] also reported an increase of

spin lifetime with the increase of In composition in $In_xGa_{1-x}N$/ GaN quantum wells. The spin relaxation times in the two sets of data varied in the range of 86-100 ps at 300K. In comparison, the relaxation times in (100)-oriented GaAs and InGaAs quantum wells are ~60 ps and 6 ps, respectively [149, 150].

6.3.4 Discussion and theoretical analysis

Spin relaxation lifetimes were of the order of 80 – 120 ps for all the samples. They increased with increasing wavelength and had weak temperature dependence with decreasing spin lifetimes at higher temperatures. The theoretical analysis behind such a trend is discussed in this section. Also, the extremely weak temperature dependence of τ_s consistently observed in this study is in agreement with the trend observed in In-rich quantum dots formed in InGaN/GaN quantum wells [151]. In contrast, spin lifetimes measured in InGaN/GaN quantum wells reportedly exhibit a rather strong temperature dependence [150]. It has been reported that as a consequence of the anisotropic SOC in the wurtzite structure, spin relaxation in GaN (and also InGaN) will be anisotropic, having a faster rate for spins pointing along the c-axis compared to spins aligned in the perpendicular (in-plane) direction [144]. It is also worth noting that although the InGaN dots in the GaN nanowires have diameters ~30 nm, there is evidence of quasi zero-dimensional behavior in these nanostructures similar to those in self-organized InGaN/GaN quantum dots [49, 113, 115, 116], which also have a base of 30-50 nm.

The DP and EY spin relaxation lifetimes were calculated for a relatively defect free GaN material system and their variations with respect to temperature and wavelength calculated to see the effects of the two scattering mechanisms on spin relaxation times measured. The EY mechanism describes randomization of a spin direction through

momentum changes and the spin relaxation time in confined 2D structures is given by:

$$\frac{1}{\tau_{EY}} = \left(\frac{\Delta_{SO}}{\Delta_{SO} + E_g}\right)^2 \left(1 - \frac{m_e^*}{m_e}\right)^2 \frac{E_c k_b T}{E_g^2} \frac{1}{\tau_p} \qquad 6.6$$

And, the variation of bandgap energy Eg with In composition x in the $In_xGa_{1-x}N$ dots is described by [152]:

$$E_g(x) = 3.4(1 - x) + 1.8x - 2.5x(1 - x) \qquad 6.7$$

Based on the equations 6.6. and 6.7, the plotted EY spin lifetimes as a function of In composition x are calculated and plotted in Fig. 6.9. It is evident that these times are

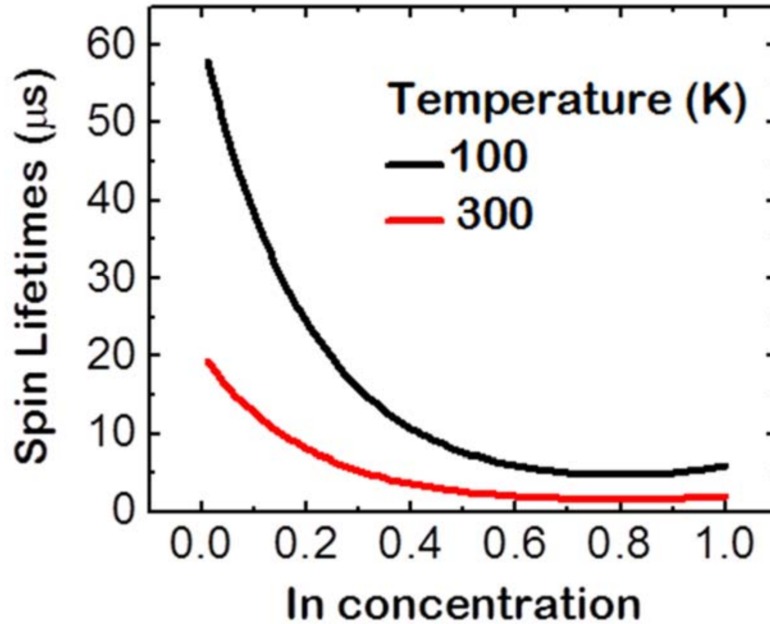

Fig. 6.9. Calculated spin lifetimes limited by Elliot-Yafet scattering in $In_xGa_{1-x}N$ quantum dots as a function of In composition at 100 and 300 K.

much larger and of microsecond order due to quantum confinement of the carrier momentum [153, 154]. More importantly, the spin relaxation time decreases with In composition, which is opposite to the trend observed experimentally in this study and by

others [148, 151]. It was therefore concluded that the EY mechanism is not relevant to the InGaN/ GaN dot-in-nanowires being investigated.

The DP spin scattering mechanism causes the spin polarized carriers to undergo spin precession about an effective magnetic field arising from splitting of the conduction band due to SOC. The direction of the effective magnetic field and hence, spin precession alters due to momentum scattering. In wurtzite structures, intrinsic inversion asymmetry is present and Rashba and cubic Dresselhaus spin-orbit coupling become important. The spin lifetimes limited by DP scattering in two-dimensional wurtzite structures is given by [155]:

$$\frac{1}{\tau_{DP}} = \frac{2\tau_p}{\hbar^2}\frac{I_1}{I_0}\left[\alpha^2 k_T^2 - 2\alpha\beta_3 k_T^4 \frac{I_{\upsilon+2}}{I_{\upsilon+4}} + \beta_3^2 k_T^6 \frac{I_{\upsilon+3}}{I_{\upsilon+1}}\right] \quad 6.8$$

where $I_\nu(\beta\mu)$, the energy convolution of the scattering mechanism is given by:

$$I_\upsilon = \beta^{\nu+1}\int_0^\infty x^\nu \frac{e^{\beta(\mu-x)}}{(1+e^{\beta(\mu-x)})^2}dx, \qquad k_T^2 = \frac{2m^*}{\hbar^2\beta} \quad 6.9$$

and $\beta = 1/(k_B T)$ while the parameter ν depends on the relevant carrier scattering mechanism [154]. The measured data was analyzed considering impurity ($\nu = 0$) and optical phonon ($\nu = 1$) scattering. The resultant scattering time is given by:

$$\frac{1}{\tau} = \frac{1}{\tau_{\upsilon=0}} + \frac{1}{\tau_{\upsilon=1}} \quad 6.10$$

It should be noted that both Rashba and Dresselhaus terms are necessary to obtain a roughly temperature dependent spin relaxation times. The spin orbit coupling parameters are $\alpha = \alpha_R + \beta_1$ where α_R is the Rashba parameter. $\beta_{1,3}$ are the linear and cubic Dresselhaus parameters and T_f is the Fermi temperature, which depends on the In composition. Since the linear Dresselhaus and Rashba parameters are indistinguishable

Parameter	Wavelengths (nm)		
	420	450	480
T_f (K)		681	
α (eV-nm)		$1.64 x 10^{-4}$	
β_3 (J.nm^3)		$4.2 x 10^{-4}$	
m* (x m_e)		0.18	
τ_p (ps)	0.99	0.91	0.84

Table 6.2. Fitting parameter for sample 3 at different wavelengths.

and because our system is essentially strain-free, the influence of the linear Dresselhaus term is disregarded and a Rashba parameter of the order of 1.64 x 10^{-4} eV-nm is considered [156-158]. Using the order of magnitude of the different parameters reported in the literature [151-159], the calculated spin relaxation times are shown in Figs. 6.8(a) and (b) alongside the experimental data. The fitting parameters used for the three different wavelengths of sample 3 in Fig. 6.8(a) and for the three samples with different In composition shown in Fig. 6.8(b) are given in Tables 6.2 and 6.3, respectively. The

Parameter	Wavelengths (nm)		
	407	420	453
T_f (K)	992	681	662
α (eV-nm)		$1.64 x 10^{-4}$	
β_3 (J.nm^3)	$3.95 x 10^{-4}$	$4.2 x 10^{-4}$	$4.2 x 10^{-4}$
m* (x m_e)	0.14	0.18	0.18
τ_p (ps)	0.97	0.85	0.96

Table 6.3. Fitting parameters for sample 1, 2 and 4.

trend in the change of the parameters with change in In concentration used to fit the spin lifetime data for the three different samples (Fig. 6.8(b)) is shown in Table 3, while only the momentum scattering times is varied to fit the experimental data of sample 3 (Fig. 6.8(a)) as shown in Table 2. In both cases, the agreement of the calculated data with the

measured ones, within limits of experimental error, is very good. It is therefore evident that spin lifetimes in the InGaN/ GaN dots-in-nanowire are primarily determined by the Rashba-induced D'yakonov-Perel' mechanism. The Elliot-Yafet scattering is absent, suggesting that defect-related scattering processes are insignificant.

6.4 Summary

In conclusion, TRPL measurements performed on highly resolved PL from GaN nanowires indicate that surface passivation with parylene lowers the recombination lifetimes of the surface related excitons resulting in improved electron hole wavefunction overlap at the surface due to the reduction of surface state density. Additionally, intrinsic spin properties of carriers optically injected in InGaN dots in GaN nanowires were measured and theoretically analyzed to find the dominant spin scattering mechanism inherent in the nitride material system and responsible for spin relaxation. The spin lifetimes measured were in the range 80-120 ps, had weak temperature dependence and increased with increasing wavelength. D'yakanov-Perel (DP) spin relaxation mechanism was found to be the dominant spin scattering mechanism causing spin relaxation in relatively defect-free quantum confined nitride structures.

Chapter VII

Conclusion and Suggestions for Future Work

7.1 Summary of the Present Work

The present study was focused on the research and development of nitride-based light sources which would eventually overcome the challenges and obstacles facing the solid state lighting industry and the development of visible lasers. The optical and structural properties of the self-assembled InGaN/GaN quantum dots (QDs) grown by plasma-assisted molecular beam epitaxy (PA-MBE) were investigated and tuned to make light sources demonstrating superior properties compared to current state-of-the-art quantum well (QW) based devices.

An extensive and systematic growth study has been conducted, as described in chapter II, to understand the influence of different growth parameters on the optical and structural properties of the self-assembled InGaN/GaN quantum dots (QDs) grown by PA-MBE. The QDs with optimized growth conditions exhibited high radiative efficiencies of ~60% for blue-emitting QDs (λ=420 nm) and ~38% for green-emitting QDs (λ=525 nm). The room temperature radiative lifetimes for the optimized blue- and green-emitting QDs were found to be ~476 ps and ~1.76 ns, respectively which were orders of magnitude lower than those reported for equivalent QWs. The QDs were also shown to have minimal In clustering, low polarization field and to have good crystalline

quality from various structural and optical characterization experiments.

The optimized InGaN QDs were incorporated in the active region of an LED heterostructure. The performance of the QD LEDs were improved through optimization of the AlGaN electron blocking layer (EBL), the active region, and p-doped GaN region by improving growth and processing conditions. QD LEDs were demonstrated with efficiencies peaking at low current densities (~40 – 50 A/cm^2), having low efficiency droop (~25%) and low peak emission shift due to weak quantum confined Stark effect (QCSE) discussed in chapter III.

One of the major roadblocks facing the solid state lighting industry has been the use of highly lattice mismatched substrates including sapphire, SiC or Si for LED epitaxy. The high dislocation density (8×10^8 cm^{-2}) present on state-of-the-art GaN-on-sapphire templates most commonly used for commercial LEDs can lead to non-radiative recombination centers in the active region, provide electrical leakage path during LED operation, cause self-heating and ultimately result in significantly degraded device performance. In chapter IV, the properties of InGaN/GaN and GaN/AlN QDs were explored in dislocation filtering through bending of defects at the base of the QDs. A reduction of the defect density to ~9×10^7 cm^{-2} was demonstrated by use the of InGaN/GaN QDs and the green-emitting QD LEDs grown on reduced defect density buffer layers were characterized. The LEDs on dislocation filter showed lower leakage currents and much higher peak efficiencies compared to the ones grown on conventional GaN/sapphire templates without dislocations.

Chapter V details the growth, design and processing challenges faced in some of the first demonstrations of QD visible lasers across all wavelengths. A systematic growth

study of the InGaN waveguide, AlGaN cladding, and InGaN/GaN QDs on cladding layers were performed with detailed material characterization. Electrical characteristics of the laser diodes were measured and QD blue lasers lasing at 418 nm and 479 nm were demonstrated under continuous wave (CW) operation with very low threshold current densities around J_{th} ~970 A/cm^2 for shorter wavelengths and a very low peak emission shift of only 4.4 nm. The slope efficiency, differential quantum efficiency and power conversion (wall plug) efficiency for pulsed operation were measured at 0.41 W/A, 13.9%, and 0.4% respectively. A very high differential gain of 2x10^{-16} cm^2 was obtained from cavity length dependent current-output measurements on such lasers. Lasers with different cladding regions emitting at longer wavelengths (λ=630 nm) were also demonstrated and their effects on output characteristics of the lasers were determined. The results obtained are very promising as the potential advantages of using QDs over state-of-the-art QWs in the lasers can be clearly observed and the results also provide an alternative technology of using MBE growth to obtain lasing.

(In)GaN nanowires having areal density of ~10^{11} cm^{-2} diameter of ~40 nm were grown on silicon substrates. By adding InGaN insertions of 2-3 nm thick, nanostructures were obtained with very similar dimensions compared to self-assembled QDs. Chapter VI briefly discusses the growth and optical characterization of such InGaN dots in GaN nanowires. The properties of spin polarized carriers in InGaN QDs in GaN nanowires were measured for the first time in such a relatively defect free environment to study the dominant spin relaxation mechanism present in the nitride material system. Spin relaxation times as long as ~80-120 ps were measured at room temperature and their dependence on increasing In composition and temperature were evaluated. D'yakonov-

Perel (DP) was found to be the dominant spin relaxation mechanism in quantum confined nitride nanostructures from a theoretical fitting.

7.2 Suggestions for the Future Work

7.2.1 Red-emitting quantum dot LEDs with dislocation filter

GaN-based LEDs and lasers emitting in the longer visible wavelengths (red) are highly desirable because of the need of red emission in making white light sources through red-green-blue mixing as well as many other applications including full-color mobile projectors, heads-up displays, optical information processing systems and a host of medical applications. The longest wavelength emission currently obtained using InGaN/GaN QWs are in the green-yellow wavelengths. Attempts to grow QWs with higher In composition results in large numbers of strain associated misfits in the active region resulting in all carriers undergoing non-radiative recombination with no visible emission in the red region from nitride systems. However, red-emitting $In_{0.4}Ga_{0.6}N/GaN$ QD lasers emitting at λ=630 nm has recently been demonstrated as was discussed in chapter V. The red-emitting QDs can be grown by a very careful control of the growth conditions and have been found to have excellent optical properties. The lasing threshold is obtained from the current-output characteristics indicating a very low threshold density of ~2.5 kA/cm^2.

However, the growth of these red QDs with high In composition on GaN/sapphire templates (dislocation density ~1x10^9 cm^{-2}) is more difficult. The defect-related yellow

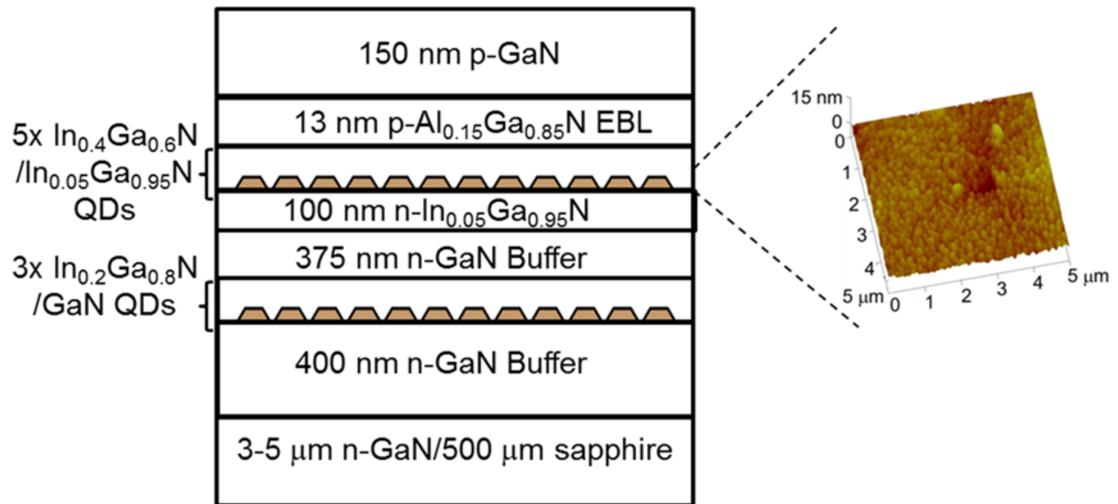

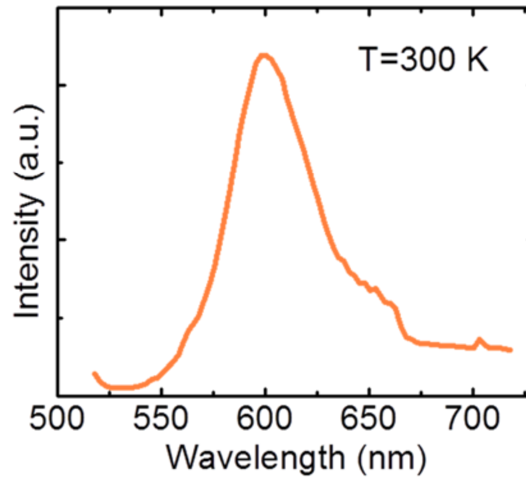

Fig. 7.1(a) Schematic of a proposed heterostructure for growing red QD LED on dislocation filter and (b) PL spectrum of the red-emitting QD grown on dislocation filter with InGaN barrier.

band emission becomes stronger than the red emission from the QDs at room temperature. This is possibly due to the In clustering at dislocations during the growth of the active region [29]. A LED heterostructure is proposed (Fig. 7.1(a)) with a QD dislocation filter optimized in chapter V serving to reduce the threading dislocation densities in the starting GaN/sapphire template. Additionally, an $In_{0.05}Ga_{0.95}N$ layer was grown for QD nucleation and QD barrier growth as shown in the heterostructure. The InGaN barrier layer reduces the strain at the QD/barrier interface preventing the creation

of any further defects. A 1 μm x 1 μm atomic force microscopy (AFM) image of an uncapped layer of red-emitting QDs is shown alongside the heterostructure in Fig. 7.1(a). Strong room temperature photoluminescence (PL) was observed from such QDs and is shown in Fig. 7.1(b). An optimization of the composition and thickness of the InGaN QD barrier layer could significantly improve the optical properties of the active region and the devices.

7.2.2 Red-green-blue (RGB) white light sources

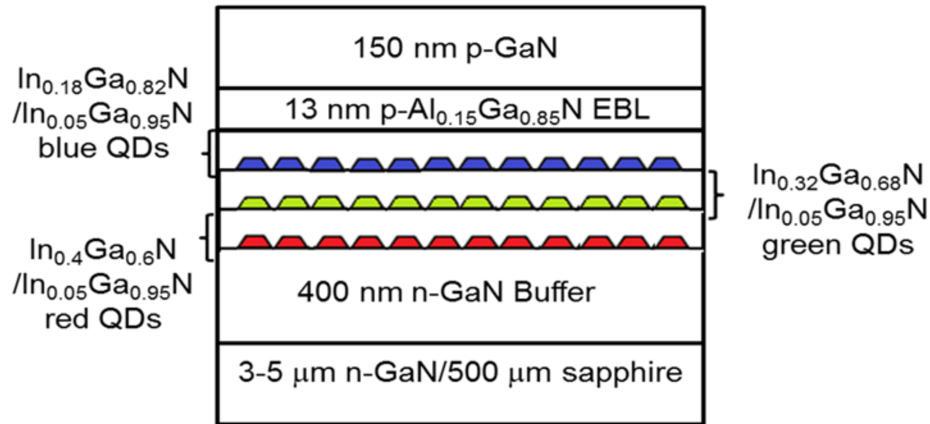

Fig. 7.2. Schematic of a proposed heterostructure for growing white QD LED on GaN/sapphire template.

A heterostructure is proposed, as shown in Fig. 7.2, incorporating vertically stacked blue-, green- and red-emitting QD active regions to obtain color tunable monolithic white LEDs emitting from the top. Current state-of-the-art white LEDs commercialized for solid state lighting use phosphor coatings on blue LED package to obtain white emission, which is inefficient and increases the cost of fabrication [8, 9]. The performance of these white LEDs can be increased significantly and a wide

tunability of the white color can be obtained by mixing blue, green, and red light in a single chip, as proposed. Recently, bulk multi-QW LEDs have been demonstrated emitting in the white region [160]. The heterostructure incorporates low composition blue

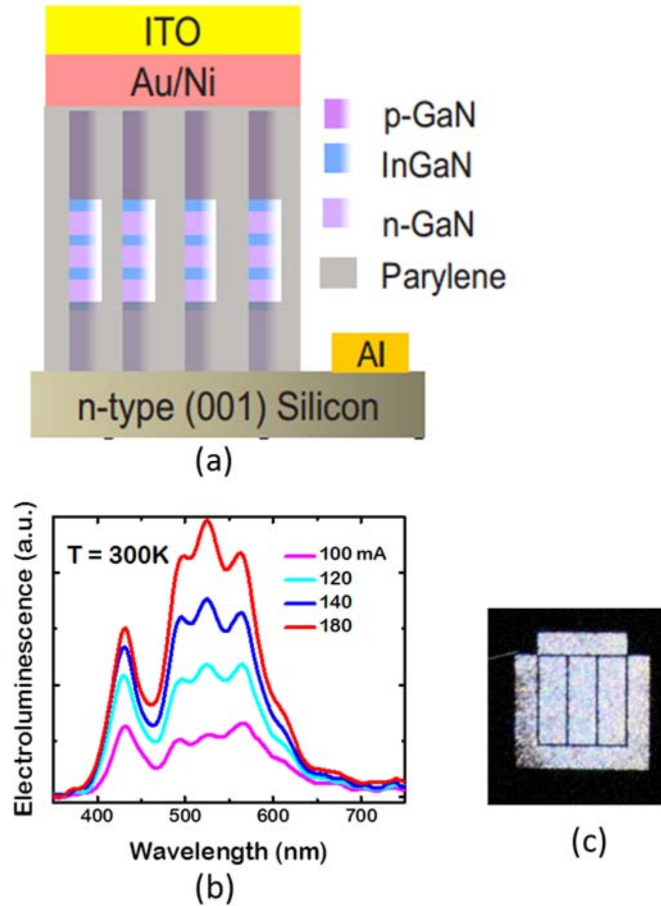

Fig. 7.3(a) Schematic of the heterostructure for white dots-in-nanowire LED on silicon, (b) electroluminescence spectra and (c) micrograph of an active white nanowire LED [127].

InGaN QW underneath the longer wavelength QW region essential for maintaining the crystalline quality of the QD active region. However, this structure would cause absorption of the shorter wavelength emission at the upper QW and the tunability of the white emission is comprised because of the difficulty in obtaining red-emitting InGaN QWs. The heretostructure proposed in Fig. 7.2 can avoid such problems with the growth of longer wavelength red QDs first as the QDs have reduced strain and In clustering

effect maintaining the crystalline quality of the active region while providing a tunable white emission. Additionally, the number of dot layers for each wavelength region should be optimized for getting white light emission. Bhattacharya *et. al.* has shown similar white emitting LEDs on nanowires [127]. The heterostructure and output characteristics of a white LED grown with multiple colored active regions in the nanowires is shown in Fig. 7.3. A micrograph of the active device is also shown in Fig. 7.3(c).

7.2.3 High power quantum dot lasers

The visible laser applications require them to emit at high output power. A major application of high power lasers especially at longer wavelengths are their usage for heads-up displays as shown in Fig. 7.4 [161]. Though promising results in terms of low

Fig. 7.4. A major application of high power laser is in heads-up display used in automobiles.

threshold current density and low peak emission shift has been demonstrated from QD lasers, they suffer from low output power. A flared broad area laser, illustrated schematically in Fig. 7.5, should be fabricated consisting of a standard straight broad area device with one side which is tapered to large dimensions. This would ensure a very high

output power from the QD lasers increasing their range of applications. The QD lasers demonstrated and reported in this thesis have ridge waveguide geometries which provides better modal characteristics (fewer waveguide modes) while a wider laser can produce and withstand higher optical powers with multiple modes supported. The tapered structure schematically drawn in Fig. 7.5 uses the advantage of both the structures by acting as a mode filter in the narrow section while providing for high output power from the broad area. Other advantages of this tapered device design will be lower threshold density due to the increase in optical confinement and reducing series resistance of the forward current operation of the device.

To improve on the standard 5 μm ridge with, typically used in our devices, the ridge should be tapered to ~30 μm, allowing for greatly increased output power. One concern in using these devices would be the inherent loss which is associated with the flare of the laser. To minimize the loss associated with the taper, the tapering angle should be less than 1° [162]. This would make the tapered region ~700 μm long. The design of the lasers in this manner would help in creating QD lasers for high power applications.

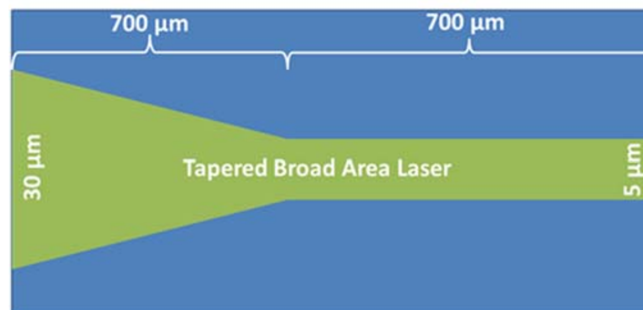

Fig. 7.5. Proposed overhead schematic of a flared broad area laser for high output power.

APPENDICES

APPENDIX A

Substrate Preparation Prior to MBE Growth

The sample must be thoroughly cleaned before introducing into the growth chamber and initiating growth. Five hundred nanometers of molybdenum is deposited at the back of the sample in order to assist pyrometer calibration of substrate temperature through radiative heating. Additional organic and metallic contaminants are present in the sample because of this process apart from the presence of native oxide on the top surface. The molybdenum deposited sample is carefully cleaned in TCE, hot acetone and isopropanol for 10 minutes each followed by DI water rinse. Subsequently, in-situ cleaning of the sample is performed involving i) a 1 hour intro-chamber baking at 200 ^{o}C for removal of moisture and surface contaminants, ii) 1 hour buffer chamber baking at 400 ^{o}C for outgassing of adsorbed gases and surface contaminants, and iii) keeping the sample under high vacuum in growth chamber for 30 minutes prior to growth.

APPENDIX B

Quantum Dot Ridge Waveguide Laser Processing

1. Deposition of Alignment Mark

1.1 Solvent clean:

Acetone: 10 min on hot plate

IPA 10 min

DI water Rinse: 2 min

1.2 Lithography

Dehydrate bake: 2 min, 115 °C hotplate

Resist coating: HMDS, SPR 220-3.0 @ 4.0 krpm, 30 sec

Pre-bake: 90 sec @ 115 °C on hotplate

Exposure: 0.34 sec in projection stepper

Post-bake: 90 sec @ 115 °C

Resist development: AZ 300 MIF 55 sec;

DI water rinse 3 min

1.3 Descum:

30 sec, 80 W, 250mT, 17% O2

1.4 Metal Deposition

Ti/Au 100 Å /300 Å

1.5 Metal Lift-off

2 hours in Acetone

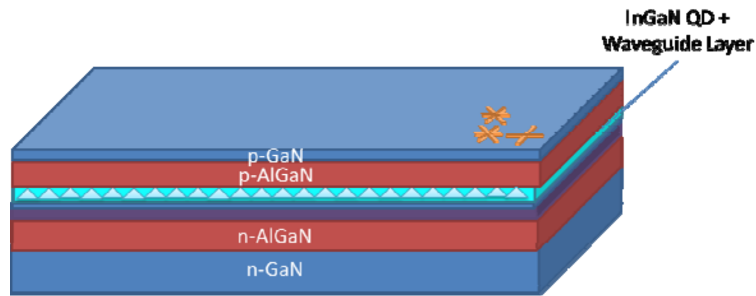

2. Defining Ridge Geometry

2.1 Solvent clean:

Acetone: 10 min on hot plate

IPA 10 min

DI water Rinse: 2 min

2.2 Lithography

Dehydrate bake: 2 min, 115 °C hotplate

Resist coating: HMDS, SPR 220-3.0 @ 4.0 krpm, 30 sec

Pre-bake: 90 sec @ 115 °C on hotplate

Exposure: 0.34 sec in projection stepper

Post-bake: 90 sec @ 115 °C

Resist development: AZ 300 MIF 55 sec;

DI water rinse 3 min

2.3 Plasma Etching

LAM:

ICP etching, etching recipe chlorine based. The etching rate is calibrated to be 4.5-5.5 ns.

2.4 Resist Removal

Plasma Asher: 300 sec, 250 W, O_2 ~17%

Acetone: 10 min on hot plate

IPA: 5 min

DI water rinse: 2 min

2.5 Dektak: measure mesa height

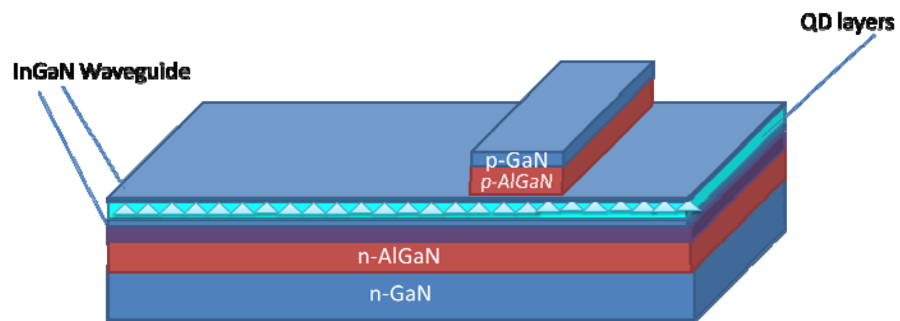

3. Etching till n-GaN

3.1 Solvent clean:

Acetone: 10 min on hot plate

IPA 10 min

DI water Rinse: 2 min

3.2 Lithography

Dehydrate bake: 2 min, 115 °C hotplate

Resist coating: HMDS, SPR 220-3.0 @ 4.0 krpm, 30 sec

Pre-bake: 90 sec @ 115 °C on hotplate

Exposure: 0.34 sec in projection stepper

Post-bake: 90 sec @ 115 °C

Resist development: AZ 300 MIF 55 sec;

DI water rinse 3 min

3.3 Plasma Etching

LAM:

ICP etching, etching recipe chlorine based. The etching rate is calibrated to be

4.5-5.5 ns.

3.4 Resist Removal

Plasma Asher: 300 sec, 250 W, O_2 ~17%

Acetone: 10 min on hot plate

IPA: 5 min

DI water rinse: 2 min

3.5 Dektak: measure mesa height

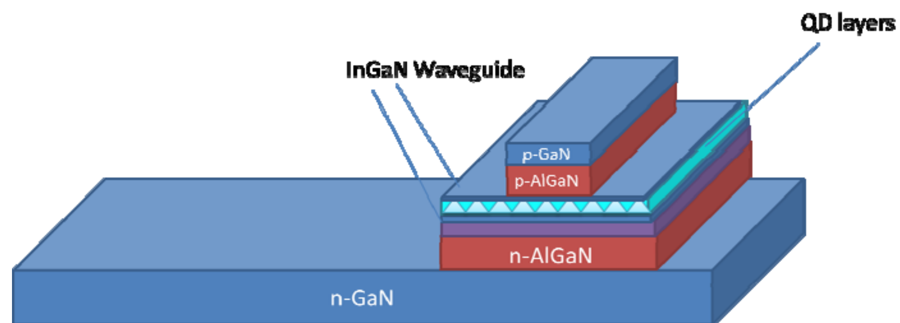

4. Deposition of n-contact

4.1 Lithography

Dehydrate bake: 2 min, 115 °C hotplate

Resist coating: HMDS, SPR 220-3.0 @ 4.0 krpm, 30 sec

Pre-bake: 90 sec @ 115 °C on hotplate

Exposure: 0.34 sec in projection stepper

Post-bake: 90 sec @ 115 °C

Resist development: AZ 300 MIF 55 sec;

DI water rinse 3 min

4.2 Descum:

30 sec, 80 W, 250mT, 17% O2

4.3 Oxide removal

HCl : DI water = 1:1, 1 min to remove native oxide

DI water rinse: 3 min

4.4 Metal deposition

Ti/Au = 25nm/300nm

4.5 Lift-off

Overnight in Acetone

IPA: 10 min

DI water: 2 min

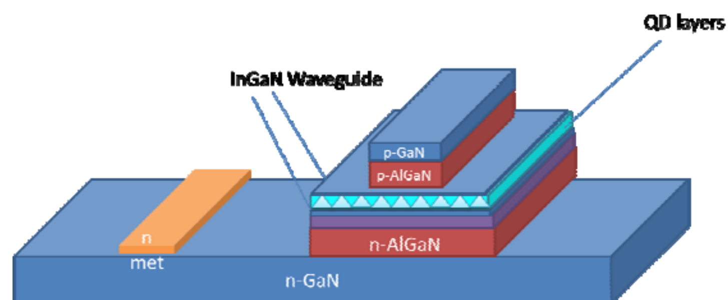

5. Passivation

SiO_x deposion: 1000 nm using GSI PECVD

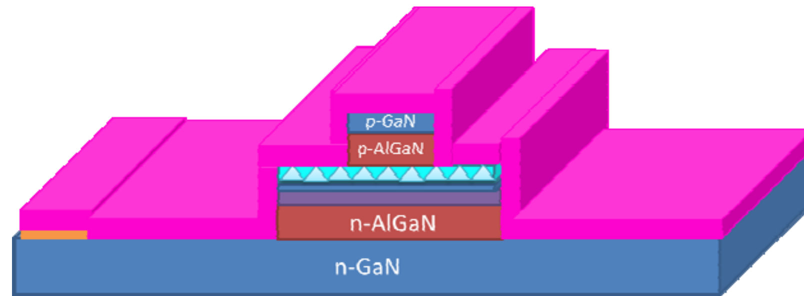

6. **Oxide Etch (Formation of Via holes)**

6.1 Lithography

Dehydrate bake: 2 min, 115 °C hotplate

Resist coating: HMDS, SPR 220-3.0 @ 4.0 krpm, 30 sec

Pre-bake: 90 sec @ 115 °C on hotplate

Exposure: 0.34 sec in projection stepper

Post-bake: 90 sec @ 115 °C

Resist development: AZ 300 MIF 55 sec;

DI water rinse 3 min

6.2 Plasma Etch

LAM:

SF_6 : C_4F_8 : Ar = 8 : 50 : 50 sccm, 10 mT, 300 W (rate ~ 175 nm/min)

6.3 Resist Removal

Plasma Asiher: 300 sec, 250 W, O_2 ~17%

Acetone: 10 min on hot plate

IPA: 5 min

DI water rinse: 2 min

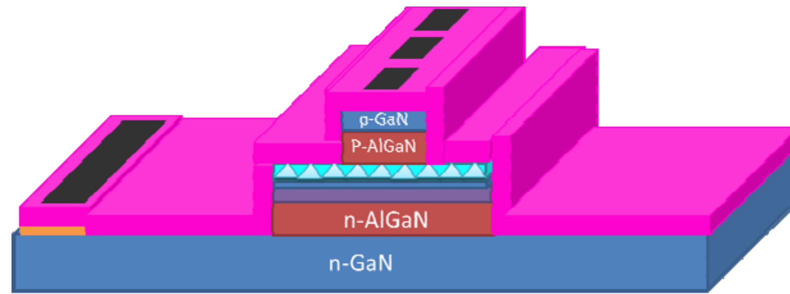

7. Deposition of p-contact and Interconnect

7.1 Lithography

Dehydrate bake: 2 min, 115 °C hotplate

Resist coating: HMDS, SPR 220-3.0 @ 4.0 krpm, 30 sec

Pre-bake: 90 sec @ 115 °C on hotplate

Exposure: 0.34 sec in projection stepper

Post-bake: 90 sec @ 115 °C

Resist development: AZ 300 MIF 55 sec;

DI water rinse 3 min

7.2 Descum:

30 sec, 80 W, 250mT, 17% O2

7.3 Oxide removal

HCl : DI water = 1:1, 1 min to remove native oxide

DI water rinse: 3 min

7.4 Metal deposition

Ti/Pt/Au = 200 Å/200 Å/3000 Å

7.5 Lift-off

Overnight in Acetone

IPA: 10 min

DI water: 2 min

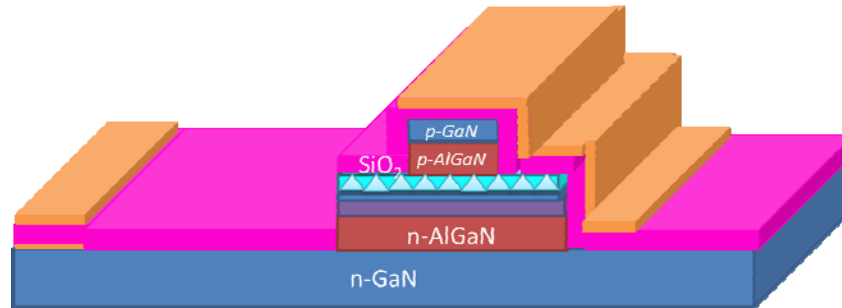

8. Annealing

8.1 Rapid thermal annealing: 550 °C, 5 min in N_2:O_2 (1:1) environment

9. Lapping

9.1 Mounting the sample on a glass plate with Paraffin wax (135 °C)

9.2 Lap down sample to ~ 100 μm

9.3 Solvent clean:

Xylenes > 30 min @ 105 °C hotplate

Acetone: 10 min

IPA : 10 min

DI water rinse: 2 min

10. Cleaving

10.1 Scribing: Make 2000 μm long, 400~1200 μm wide, 100 μm deep scribe

10.2 Press the sample gently with a small roller.

BIBLIOGRAPHY

BIBLIOGRAPHY

[1] J. M. Phillips, M. E. Coltrin, M. H. Crawford, A. J. Fischer, M. R. Krames, R. Mueller-Mach, G. O. Mueller, Y. Ohno, L. E. S. Rohwer, J. A. Simmons, and J. Y. Tsao, *Laser & Photon. Rev.* **1**, 307 (2007).

[2] US Department of Energy, “Life-Cycle Assessment of Energy and Environmental Impacts of LED Lighting Products," February (2012).

[3] N. Holonyak Jr. and S. F. Bevacqua, *Appl. Phys. Lett.* **1**(4), 82 (1962).

[4] S. Nakamura, M. Senoh, N. Iwasa, and S. Nagahama, *Jpn. J. Appl. Phys.* **34**, L797–L799 (1995).

[5] H. Amano, N. Sawaki, I. Akasaki, and Y. Toyoda, *Appl. Phys. Lett.* **48**, 353 (1986).

[6] S. Nakamura, *Jpn. J. Appl. Phys.* **30**, L1705 (1991).

[7] H. Amano, M. Kito, K. Hiramatsu, and I. Akasaki, *Jpn. J. Appl. Phys.* **28**, L2112 (1989).

[8] S. Nakamura, T. Mukai, M. Senoh, and N. Iwasa, *Jpn. J. Appl. Phys.* **31**, L139 (1992).

[9] A. A. Setlur, *Electrochem. Soc. Interface* **18**(4), 32 (2009).

[10] S. Nakamura , M. Senoh , S. Nagahama , N. Iwasa , T. Yamada , T. Matsushita , Y. Sugimoto and H. Kiyoku, *Appl. Phys. Lett.* **69**, 4056 (1996).

[11] Y. Enya, Y. Yoshizumi, T. Kyono, K. Akita, M. Ueno, M. Adachi, T. Sumitomo, S. Tokuyama, T. Ikegami, K. Katayama, and T. Nakamura, *Appl. Phys. Exp.*, **2**, 082101 (2009).

[12] S. Nakamura, M. Senoh, and T. Mukai, *Jpn. J. Appl. Phys.*, **32**, L8 (1993).

[13] S. Nakamura, T. Mukai, and M. Senoh, *Appl. Phys. Lett.*, **64**, 1687 (1994).

[14] M. R. Krames, O. B. Shchekin, R. Mueller-Mach, G. O. Mueller, L. Zhou, G. Harbers, and M. G. Craford, *IEEE J. Display Technol.*, **3**(2), 160 (2007).

[15] O. B. Shchekin,a J. E. Epler, T. A. Trottier, T. Margalith, D. A. Steigerwald, M. O. Holcomb, P. S. Martin, and M. R. Krames, *Appl. Phys. Lett.*, **89**, 071109 (2006).

[16] Y. C. Shen, G. O. Mueller, S. Watanabe, N. F. Gardner, A. Munkholm, and M. R. Krames, *Appl. Phys. Lett.*, **91**, 141101 (2007).

[17] M.-H. Kim, M. F. Schubert, Q. Dai, J. K. Kim, E. F. Schubert, J. Piprek, and Y. Park, *Appl. Phys. Lett.*, **91**, 183507 (2007).

[18] Y. Yang, X. A. Cao, and C. Yan, *IEEE Trans. on Elec. Dev.*, **55**, 1771 (2008).

[19] S. F. Chichibu, T. Sota, K. Wada, and S. Nakamura, *J. Vac. Sci. Technol. B* **16**, 2204 (1998).

[20] A. David, M. J. Grundmann, J. F. Kaeding, N. F. Gardner, T. G. Mihopoulos, and M. K. Krames, *Appl. Phys. Lett.,* **92***,* 053502 (2008).

[21] A. D. Dräger, H. Jőnen, C. Netzel, U. Rossow, and A. Hangleiter, *8th Intern. Conf. Nitride Semicon.,* Jeju (2009).

[22] M. Zhang, P. Bhattacharya, J. Singh, and J. Hinckley, *Appl. Phys. Lett.* **95**, 201108 (2009).

[23] A. E. Yunovich, V. E. Kudryashov, A. N. Turkin, A. Kovalev, and F. Manyakhin, *MRS Int. J. Nitride Semicond. Res.* **3**, 44 (1998).

[24] I. V. Rozhansky and D. A. Zakheim, *Phys. Status Solidi A* **204**, 227 (2007).

[25] A. Laubsch, M. Sabathil, W. Bergbauer, M. Strassburg, H. Lugauer, M. Peter, S. Lutgen, N. Linder, K. Streubel, J. Hader, J. V. Moloney, B. Pasenow, and S. W. Koch, *Phys. Status Solidi C* **6**, S913 (2009).

[26] A. Avramescu, T. Lermer, J. Müller, S. Tautz, D. Queren, S. Lutgen, and U. Strauß, *Appl. Phys. Lett.,* **95**, 071103 (2009).

[27] D. Sizov, R. Bhat, Fellow, and C.-E. Zah, *J. Llightwave Tech.*, **30**(5), 679 (2012).

[28] N. K. van der Laak, R. A. Oliver, M. J. Kappers, and C. J. Humphreys, *Appl. Phys. Lett.*, **90**, 121911 (2007).

[29] M. Rao, D. Kim, and S.Mahajan, *Appl. Phys. Lett.*, **85**, 1961 (2004).

[30] T. Takeuchi, S. Sota, M. Katsuragawa, M. Komori, H. Takeuchi, H.Amano, and I. Akasaki, *Jpn. J. Appl. Phys.*, **36**, L382 (1997).

[31] S. Nakamura, T. Mukai, M. Senoh, and N. Iwasa, *Jpn. J. Appl. Phys.*, **31**, L139 (1992).

[32] M. Zhang, P. Bhattacharya, W. Guo, and A. Banerjee, *Appl. Phys. Lett.* **96**, 132103 (2010).

[33] J. Piprek, *Phys. Status Solidi A,* 1–9 (2010).

[34] J. Piprek and S. Li, *Optical and Quantum Electronics* **42**(2), 89 (2010).

[35] N. F. Gardner, G. O. Muller, Y. C. Shen, G. Chen, S. Watanabe, W. Gotz, and M. R. Krames, *Appl. Phys. Lett.* **91**, 243506 (2007).

[36] J. H. Son and J.-L. Lee, *Opt. Express* **18**, 5466 (2010).

[37] S. Yamada, Y. Zhao, C. C. Pan, R. B. Chung, K. Fujito, J. Sonoda, S. P. DenBaars, and S. Nakamura, *Appl. Phys. Exp.*, **2**, 122102 (2010).

[38] Y. Enya, Y. Yoshizumi, K. Akita, M. Ueno, M. Adachi, T. Sumitomo, S. Tokuyama, T. Ikegami, K. Katayama, and T. Nakamura, *Appl. Phys. Exp.*, **2**, 082101 (2009).

[39] Y. Yoshizumi, M. Adachi, Y. Enya, T. Kyono, S. Tokuyama, T. Sumitomo, K. Akita, T. Ikegami, M. Ueno, K. Katayama, and T. Nakamura, *Appl. Phys. Exp.*, **2**, 092101 (2009).

[40] C. Adelmann, J. Simon, G. Feuillet, N. T. Pelekanos, B. Daudin, G. Fishman, *Appl. Phys. Lett.* **76**(12), 1570 (2000).

[41] R. A. Oliver, G. A. D. Briggs, M. J. Kappers, C. J. Humphreys, S. Yasin, J. H. Rice, J. D. Smith, R. A. Taylor, *Appl. Phys. Lett.* **83**(4), 755 (2003).

[42] K. S. Ramaiah, Y. K. Su, S. J. Chang, B. Kerr, H. P. Liu, I. G. Chen, *Appl. Phys. Lett.* **84**(17), 3307 (2004).

[43] S. Fathpour, Z. Mi, and P. Bhattacharya, *J. Phys. D Appl. Phys.* **38**, 2103 (2005).

[44] P. G. Eliseev, H. Li, T. Liu, T. C. Newell, L. F. Lester, and K. J. Malloy, *IEEE J.Selected Topics in Quantum Electron.* **7**, 135 (2001).

[45] J. Yang, P. Bhattacharya, and Z. Mi, *IEEE Transactions on Electron Devices* **54**(11), 2849 (2007).

[46] S. Nakamura, M. Senoh, N. Iwasa, and S. Nagahama, *Jpn. J. Appl. Phys.*, **34**, L797–L799 (1995).

[47] Y.-R. Wu, Y.-Y. Lin, H.-H. Huang, and J. Singh, *J. Appl. Phys.* **105**, 013117 (2009).

[48] S. Schulz and E. P. O' Reilly, *Phys. Rev. B* **82**, 033411 (2010).

[49] M. Zhang, P. Bhattacharya, and W. Guo, *Appl. Phys. Lett.* **97**, 011103 (2010).

[50] Z. Chen, D. Lu, H. Yuan, P. Han, X. Liu, Y. Li, X. Wang, Y. Lu, and Z. Wang, *J. Cryst. Growth* **235,** 188 (2002).

[51] H. Hirayama, S. Tanaka, and Y. Aoyagi *Microelectronic Engineering* **49**, 287 (1999).

[52] R. A. Oliver, G. A. D. Briggs, M. J. Kappers, C. J. Humphreys, S. Yasin, J. H. Rice, J. D. Smith, R. A. Taylor *Appl. Phys. Lett.* **83**,755 (2003).

[53] C. Adelmann, J. Simon, G. Feuillet, N. T. Pelekanos, B. Daudin, G. Fishman *Appl. Phys. Lett.* **76**, 1570 (2000).

[54] N. Grandjean and J. Massies, *Appl. Phys. Lett.* **72**, 1078 (1998).

[55] S. Dalmasso, B. Damilano, N. Grandjean, J. Massies, M. Leroux, J. L. Reverchon, J. Y. Duboz, *Thin Solid Films,* **380**, 195 (2000).

[56] K. Tachibana, T. Someya, Y. Arakawa, *Appl. Phys. Lett.* **74**, 383 (1999).

[57] F. C. Frank, and J. H. van der Merwe, *Proceedings of Royal Society of London A*, **198**, 205 (1949).

[58] M. Volmer, and A. Weber, *Z. Phys. Chem.*, **119**, 277 (1926).

[59] A. Pimpinelli, J. Villain *Physics of Crystal Growth. Cambridge*: Cambridge University Press (1998)..

[60] K. Oura, V. G. Lifshits, A. A. Saranin, A. V. Zotov, and M. Katayama *Surface Science*: *An Introduction*, Berlin: Springer (2003).

[61] I. N. Stranski, and L. Krastanow, *Abt. IIb.*, Band, **146**, 146 (1937).

[62] B. Damilano, N. Grandjean, S. Dalmasso, and J. Massies, *Appl. Phys. Lett.* **75**(24), 3751 (1999).

[63] B. Heying, R. Averbeck, L. F. Chen, E. Haus, H. Riechert, and J. S. Speck, *J. Appl. Phys*. **88**(4), 1855 (2000).

[64] W.-G, Jung, J.-M. Jang, and S.-K. Choi, and J.-Y. Kim, *Phys. Stat. Solidi C* **6**(4), 797 (2009).

[65] B. Damilano, N. Grandjean, S. Dalmasso, and J. Massies, *Appl. Phys. Lett.* **75**(24), 3751 (1999).

[66] T. Bartel, M. Dworzak, M. Strassburg, A. Hoffmann, A. Strittmatter, and D. Bimberg, *Appl. Phys. Lett.* **85**, 1946 (2004).

[67] M. Pophristic, F. H. Long, C. Tran, I. T. Ferguson, R. F. Carlicek Jr., *J. Appl. Phys.* **86**, 1114 (1999).

[68] S.-W. Feng, Y.-C. Cheng, Y.-Y. Chung, C. C. Yang, Y.-S. Lin, C. Hsu, K.-J. Ma, and J.-I. Chyi, *J. Appl. Phys.* **92**(8), 4441 (2002).

[69] K. Ramaiah, Y. K. Su, S. J. Chang, B. Kerr, H. P. Liu, and I. G. Chen, *Appl. Phys. Lett.* **87**(17), 3307 (2004).

[70] Y. Varshni, Physica 34(1), 149–154 (1967).

[71] J. Amar, and F. Family, *Phys. Rev. Lett.* **74**, 2066 (1995).

[72] T. Li, A. M. Fischer, Q. Y. Wei, F. A. Ponce, T. Detchprohm, and C. Wetzel, *Appl. Phys. Lett.* **96**, 031906 (2010).

[73] S.-H. Han, D.-Y. Lee, S.-J. Lee, C.-Y. Cho, M.-K. Kwon, S. P. Lee, D. Y. Noh, D.-J. Kim, Y. C. Kim and S.-J. Park, *Appl. Phys. Lett.* **94**, 231123 (2009).

[74] E. Iliopoulos and T. D. Moustakas, *Appl. Phys. Lett.* **81**(2), 295 (2002).

[75] J. Simon and D. Jena, *Phys. Stat. Sol. (a)* **205**(5), 1074–1077 (2008).

[76] J.-W. Shi, J.-K. Sheu, C.-H. Chen, G.-R. Lin, and W.-C. Lai, *IEEE Electron Device Letters* **29**, 158-160 (2008).

[77] D. Queren, A. Avramescu, G. Bruderl, A. Breidenassel, M. Schillgalies, S. Lutgen, and U. Strauß, *Appl. Phys. Lett.* **94**(8), 081119 (2009).

[78] J. Müller, G. Brüderl, M. Schillgalies, S. Tautz, D. Dini, A. Breidenassel, B. Galler, and S. Lutgen, *Appl. Phys. Lett.* **95**(5), 051104 (2009).

[79] T. Mukai, M. Yamada and S. Nakamura, *Jpn. J. Appl. Phys.* **38**, 3976-3981 (1999).

[80] A. David and M. J. Grundmann, *Appl. Phys. Lett.* **97**, 033501 (2010).

[81] Y. Yang, X. A. Cao and C. Yan, *IEEE Trans. Electron Devices* **55**, 1771 (2008).

[82] P. Bhattacharya, M. Zhang, and J. Hinckley, *Appl. Phys. Lett.* **97**, 251107 (2010).

[83] A. David and M. J. Grundmann, Appl. Phys. Lett. **96**, 103504 (2010).

[84] A.E. Chernyakov, M.M. Sobolev, V.V. Ratnikov, N.M. Shmidt, and E.B. Yakimov, *Superlattices and Microstructures* **45**, 301 (2009).

[85] W. Guo, M. Zhang, P. Bhattacharya, and J. Heo, *Nano Lett.* **11**, 1434 (2011).

[86] S. Hausser, G. Fuchs, A. Hangleiter, K. Streubel, and W. T. Tsang, *Appl. Phys. Lett.* **56**, 913 (1990).

[87] D. Klotzkin, K. Kamath, and P. Bhattacharya, *IEEE Photonics Tech. Lett.* **9**, 1301 (1997).

[88] T. B. Norris, K. Kim, J. Urayama, Z. K. Wu, J. Singh, and P. Bhattacharya, *J. Phy. D: Appl. Phys.* **38**, 2077 (2005).

[89] D. R. Matthews, H. D. Summers, P. M. Smowton, and M. Hopkinson, *Appl. Phys. Lett.* **81**, 4904 (2002).

[90] Y. S. Lin, K. J. Ma, C. Hsu, S. W. Feng, Y. C. Cheng, C. C. Liao, C. C. Yang, C. C. Chou, C. M. Lee, J. I. Chyi, *Appl. Phys. Lett.* **77**(19), 2988 (2000).

[91] J. Yang, P. Bhattacharya, and Z. Mi, IEEE Transactions on Electron Devices 54(11), 2849 (2007).

[92] D. Huang, M. A. Reshchikov, F. Yun, T. King, A. A. Baski, and H. Morkoç, *Appl. Phys. Lett.* **80**(2), 216 (2002).

[93] C. Adelmann, B. Daudin, R. A. Oliver, G. A. D. Briggs, and R. E. Rudd, *Phys. Rev. B* **70**, 125427 (2004).

[94] G. Kamler, J.L. Weyher, I. Grzegory, E. Jezierska, T. Wosiński, *J. Crys. Growth* **246**, 21-24 (2002).

[95] D. Zhuang, J.H. Edgar, *Materials Science and Engineering* **R48**, 1-46 (2005).

[96] J. L. Weyher, *Cryst. Res. Technol.* **47**(3), 333 – 340 (2012).

[97] G. Kamler, J. Smalc, M. Woźniak, J. L. Weyher, R. Czernecki, G. Targowski, M. Leszczyński, I. Grzegory, and S. Porowski, *J. Crys. Growth* **293**, 18-21 (2006).

[98] P. R. Berger, K. Chang, P. Bhattacharya, J. Singh, and K. K. Bajaj, *Appl. Phys. Lett.* **53**, 684 (1988).

[99] J. Yang, P. Bhattacharya, and Z. Mi, *IEEE Transactions on Electron Devices* **54**(11), 2849 (2007).

[100] J. Nie, S. A. Chevtchenko, J. Xie, X. Ni, and H. Morkoç, *Proc. of SPIE* **6894**, 689424 (2008).

[101] A. Banerjee, T. Frost, S. Jahangir, E. Stark, and P. Bhattacharya, *J. Crys. Growth* **378**, 566–570 (2013).

[102] T. Frost, A. Banerjee, K. Sun, S. L. Chuang, P. Bhattacharya, *IEEE J. Quantum Electron.* **49**(11), 923 (2013).

[103] K. Akita, T. Kyono, Y. Yoshizumi, H. Kitabayashi, and K. Katayama, *SEI Technical Review* **65**, 35 (2007).

[104] I.-L. Lu, Y.-R. Wu, and J. Singh, *J. Appl. Phy.* **108**, 124508 (2010).

[105] H. Ohta, S. P. DenBaars, and S. Nakamura, *J. Opt. Soc. Am. B* **27**, B45 (2010).

[106] O. H. Nam, K. H. Ha, J. S. Kwak, S. N. Lee, K. K. Choi, T. H. Chang, S. H. Chae, W. S. Lee, Y. J. Sung, H. S. Paek, J. H. Chae, T. Sakong, J. K. Son, H. Y. Ryu, Y. H. Kim, and Y. Park, *Phys. Stat. Sol. (a)* **201**(12), 2712-2720 (2004).

[107] K. Okamoto, J. Kashiwagi, T. Tanaka, and M. Kubota, *Appl. Phys. Lett.* **94**, 071105 (2009).

[108] R. M. Farrell, D. A. Haeger, P. S. Hsu, M. C. Schmidt, K. Fujito, D. F. Feezell, S. P. DenBaars, J. S. Speck, and S. Nakamura, *Appl. Phys. Lett.* **99**, 171113 (2011).

[109] U. Strauß, S. Brüninghoff, M. Schillgalies, C. Vierheilig, N. Gmeinwieser, V. Kümmler, G. Brüderl, S. Lutgen, A. Avramescu, D. Queren, D. Dini, C. Eichler, A. Lell, U. T. Schwarz, *Proc. of SPIE* **6894**, 689417 (2008).

[110] K. Okamoto, J. Kashiwagi, T. Tanaka, and M. Kubota, *Appl. Phys. Lett.* **94**, 071105 (2009).

[111] J. E. Northrup, *Appl. Phys. Lett.* **93**, 133107 (2009).

[112] F. Wu, Y. D. Lin, A. Chakraborty, H. Ohta, S. P. DenBaars, S. Nakamura, and J. S. Speck, *Appl.Phys. Lett.* **96**, 231912 (2010).

[113] A Banerjee, T Frost, E Stark, P Bhattacharya, *Appl.Phys. Lett.* **101**(4), 041108 (2012).

[114] M Zhang, A Banerjee, CS Lee, JM Hinckley, P Bhattacharya, *Appl. Phys. Lett.* **98**, 221104 (2011).

[115] A Banerjee, T Frost and P Bhattacharya, *J. Phys. D: Appl. Phys.*, **46**, 264004 (2013).

[116] A. Banerjee, T. Frost, S. Jahangir, E. Stark, and P. Bhattacharya, *Phy. Stat. Sol. (c)* **10**(5), 816 (2013).

[117] P. Bhattacharya, “Semiconductor Opotoelectronic Device”, Second Edition, Prentice Hall PTR (1997).

[118] M. T. Hardy, D. F. Feezell, S. P. DenBaars, and S. Nakamura, Materials Today **14**(9), 408 (2011).

[119] Y. D. Jho, J. S. Yahng, E. Oh, D. S. Kim, Phys. Rev. B, 66, 035334 (2002).

[120] C. Skierbiszewski, *Appl. Phys. Express* **5**, 022104 (2012).

[121] H. Zhao, R. A. Arif, Y. K. Ee, N. Tansu, *Opt. Quant. Electron.* **40**, 301 (2008).

[122] W. G. Scheibenzuber, U. T. Schwarz, L. Sulmoni, J. Dorsaz, J.-F. Carlin, and N. Grandjean, *J. Appl. Phys.* **109**, 093106 (2011).

[123] S. Fathpour, Z. Mi, and Pallab Bhattacharya, *IEEE Photonics Tech. Lett.* **17**(11), 2250 (2005).

[124] Z. Mi, P. Bhattacharya,and S. Fathpour, *Appl. Phys. Lett.* **86**, 153109 (2005).

[125] D.G. Deppe, K. Shavritranuruk, G. Ozgur, H. Chen, and S. Freisem, *Electronics Letters*, **45**(1) (2009).

Chapter 5

[126] W. Guo, A. Banerjee, M. Zhang, and P. Bhattacharya, *Appl. Phys. Lett.* **98**, 183116 (2011).

[127] W. Guo, A. Banerjee, P. Bhattacharya, and B. S. Ooi, *Appl. Phys. Lett.* **98**, 193102 (2011).

[128] W. Guo, M. Zhang, A. Banerjee, and P. Bhattacharya, *Nano Letters* **10**, 3355 (2010).

[129] R. Calarco, R. J. Meijers, R. K. Debnath, T. Stoica, E. Sutter, and H. Lüth, *Nano Lett.* **7**, 2248 (2007).

[130] L. Cerutti, J. Ristic, S. Fernandez-Garrido, E. Calleja, A. Trampert, K. H. Ploog, S. Lazic, J. M. Calleja, *Appl. Phys. Lett.* **88**, 213114 (2006).

[131] T. Kuykendall, P. Ulrich, S. Aloni, P. Yang, *Nat. Mater.* **6**, 951 (2007).

[132] X. Duan and C. M. Lieber, *J. Am. Chem. Soc.* **122**, 188 (2011).

[133] S. Fernandez-Garrido, J. Grandal, E. Calleja, M. A. Sanchez-Garcia and D. Lopez-Romero, *J. Appl. Phys.* **106**, 126102 (2009).

[134] A. Armstrong, Q. Li, K. H. A. Bogart, Y. Lin, G. T. Wang, and A. A. Talin, *J. Appl. Phys.* **106**, 053712 (2009).

[135] W. Guo, M. Zhang, P. Bhattacharya, and J. Heo, *Nano Lett.* **11**, 1434 (2011).

[136] R. Calarco, M. Marso, T. Richter, A. I. Aykanat, R. Meijers, A. D. Hart, T. Stoica, and H. Luth, *Nano Lett.* **5**, 981 (2005).

[137] N. A. Sanford, P. T. Blanchard, K. A. Bertness, L. Mansfield, J. B. Schlager, A. W. Sanders, A. Roshko, B. B. Burton, and S. M. George, *J. Appl. Phys.* **107**, 034318 (2010).

[138] Y. Kanemitsu, K. Tomita, D. Hirano, H. Inouye, *Appl. Phys. Lett.* **88**, 121113 (2006).

[139] *Spin Physics in Semiconductors*, edited by M. I. Dyakonov (Springer, Berlin, 2008).

[140] B. Beschoten, E. J. Halperin, D. K. Young, M. Poggio, J. E. Grimaldi, S. Keller, S. P. Denbaars, U. K. Mishra, E. L. Hu, and D. D. Awschalom, *Phys. Rev. B* **63**, 121202 (2001).

[141] A. Tackeuchi, T. Kuroda, A. Shikanai, T. Sota, A. Kuramata, K. Domen, *Physica E* 1011 – 1014 (2000).

[142] I. A. Buyanova, M. Izadifard, W. M. Chen, J. Kim, F. Ren, G, Thaler, C. R. Abernathy, S. J. Pearton, C. C. Pan, G. T. Chen, J. I. Chyi, and J. M. Zavada, *Appl. Phys. Lett.* **84**, 14 (2004).

[143] A. Banerjee, F. Doğan, J. Heo, A. Manchon, W. Guo, and P. Bhattacharya, *Nano Letters* **11**, 5396 (2011).

[144] J. H. Buβ, J. Rudolph, F. Natali, F. Semond, and D. Hagele, *Appl. Phys. Lett.* **95**, 192107 (2009).

[145] W. M. Chen, I. A. Buyanova, K. Nishibayashi, K. Kayanuma, K. Seo, A. Murayama, Y. Oka, G. Thaler, R. Frazier, C. R. Abernathy, F. Ren, S. J. Pearton, C. C. Pan, G. T. Chen, and J. Y. Chyi, *Appl. Phys. Lett.* **87**, 192107 (2005).

[146] S. L. Chuang and C. S. Chang, Semicond. Sci. Tech. 12, 252-263 (1997).

[147] A. V. Maslov and C. Z. Ning, *IEEE J. Quant. Electron.* **40**, 1389 (2004).

[148] S. Nagahara, M. Aritra, and Y. Arakawa, *Appl. Phys. Lett.* **86**, 242103 (2005).

[149] M. Oestreich, M. Bender, J. Hubner, D. Hagele, W. W. Ruhle, Th Hartmann, P. J. Klar, W. Heimbrodt, M. Lampalzer, K. Volz, and W. Stolz, *Semicond. Sci. Technol.* **17**, 285-297 (2002).

[150] A. Tackeuchi, O. Wada, Y. Nishikawa, Appl. Phys. Lett. 70, 1131 (1997).

[151] S. Nagahara, M. Aritra, and Y. Arakawa, *Appl. Phys. Lett.* **88**, 083101 (2006).

[152] O. Mayrock, H.-J. Wunsche, and F. Henneberger, Physical Review B, 62, 16870 (2000).

[153] M. W. Wu, J. H. Jiang, and M. Q. Weng, *Phys. Rep.* **61**, 493 (2010).

[154] N. J. Harmon, W. O. Putikka, and R. Joynt, *Phys. Rev. B* **81**, 085320 (2010).

[155] N. J. Harmon, W. O. Putikka and R. Joynt, *arXiv:1003.0494* (2010).

[156] W.-T. Wang, C. L. Wu, J. C. Chiang, Ikai Lo, H. F. Kao, Y. C. Hsu, W. Y. Pang, D. J. Jang, M. E Lee, Y.-C. Chang, and C.-N. Chen, *Journal of App. Phys.* **108**, 84718 (2010).

[157] C. Bo Shen Yun, Q. Zhang, F. Xu, N. Tang, L. Cen, X. Wang, Y. Chen, and J. Yu, *Appl. Phys. Lett.* **97**, 18194 (2010).

[158] J. Y. Fu and M. W. Wu, *Journal of Appl. Phys.* **104**, 93712 (2010).

[159] H. Chang, N. Biyikli, U. Ozgur, C. Kurdak, H. Markoc, V.I. Litvinov, *Physica E* **40**, 1586 (2008).

[160] H. Li , P. Li, J. Kang, Z. Li, Z. Li, J. Li, X. Yi, and G. Wang, *Appl. Phys. Exp.* **6**, 102103 (2013).

[161] Denso Global News Release: "http://www.globaldenso.com/en/newsreleases/121019-01.html"

[162] N. Michel, M. Krakowski, I. Hassiaoui, M.Calligaro, M. Lecomte, O. Parillaud,P. Weinmann, C. Zimmermann, W. Kaiser, M.Kamp, and A. Forchel, *Proc. of Spie*, **6909**, 690918 (2008).